

STRUCTURAL AND CHEMICAL PROPERTIES OF PURE AND DOPED GOLD NANO-CLUSTERS

By

KRISHNAKANTA MONDAL

PHYS03201004006

Raja Ramanna Centre for Advanced Technology, Indore

A thesis submitted to the

Board of Studies in Physical Sciences

In partial fulfillment of requirements

for the Degree of

DOCTOR OF PHILOSOPHY

of

HOMI BHABHA NATIONAL INSTITUTE

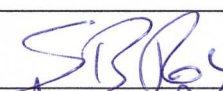
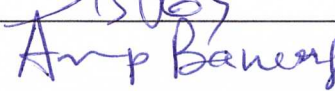
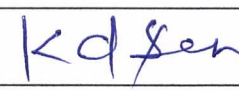
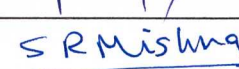
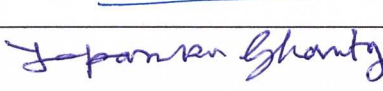

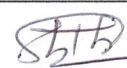
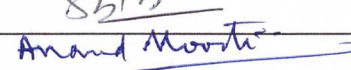


July, 2015

Homi Bhabha National Institute¹

Recommendations of the Viva Voce Committee

As members of the Viva Voce Committee, we certify that we have read the dissertation prepared by **Krishnakanta Mondal** entitled “**Structural and Chemical Properties of Pure and Doped Gold Nano-clusters**” and recommend that it may be accepted as fulfilling the thesis requirement for the award of Degree of Doctor of Philosophy.


Chairman- Prof. S. B. Roy		Date: 26.11.2015
Guide- Prof. Arup Banerjee		Date: 26/11/2015
External Examiner- Prof. K. D. Sen		Date: 26 Nov 2015
Member1- Prof. S. R. Mishra		Date: 26-11-2015
Member2- Prof. T. K. Ghanty		Date: 26/11/2015
Member3- Dr. Vinit Kumar		Date: 26/11/2015
Member4- Dr. Tarun K. Sharma		Date: 26/11/2015
Member5- Dr. Anand Moorti		Date: 26/11/2015

Final approval and acceptance of this thesis is contingent upon the candidate's submission of the final copies of the thesis to HBNI.

I/We hereby certify that I/we have read this thesis prepared under my/our direction and recommend that it may be accepted as fulfilling the thesis requirement.

Date: 26/11/2015

Place: INDORE


Guide: _____
Prof. Arup Banerjee

¹This page is to be included only for final submission after successful completion of viva voce.

STATEMENT BY AUTHOR

This dissertation has been submitted in partial fulfillment of requirements for an advanced degree at Homi Bhabha National Institute (HBNI) and is deposited in the Library to be made available to borrowers under rules of the HBNI.

Brief quotations from this dissertation are allowable without special permission, provided that accurate acknowledgement of source is made. Requests for permission for extended quotation from or reproduction of this manuscript in whole or in part may be granted by the Competent Authority of HBNI when in his or her judgment the proposed use of the material is in the interests of scholarship. In all other instances, however, permission must be obtained from the author.

Krishnakanta Mondal

DECLARATION

I, hereby declare that the investigation presented in the thesis has been carried out by me. The work is original and has not been submitted earlier as a whole or in part for a degree/diploma at this or any other Institution/University.

Krishnakanta Mondal

List of Publications Arising From the Thesis

Journals

1. "Density functional investigation on the structures and properties of Li atom doped Au₂₀ cluster" **K. Mondal**, T. K. Ghanty, A. Banerjee, A. Chakrabarti, C. Kamal, *Mol. Phys.*, **2013**, *111*, 725-734.
2. "Significant modulation of CO adsorption on bimetallic Au₁₉Li cluster" **K. Mondal**, D. Manna, T. K. Ghanty, A. Banerjee, *Chem. Phys.*, **2014**, *428*, 75-81.
3. "Structural and chemical properties of sub-nanometer sized bimetallic Au₁₉Pt cluster" **K. Mondal**, A. Banerjee, T. K. Ghanty, *J. Phys. Chem. C*, **2014**, *118*, 11935-11945.
4. "Silicene: A promising surface to achieve morphological transformation in gold clusters" **K. Mondal**, C. Kamal, A. Banerjee, A. Chakrabarti, T. K. Ghanty, *J. Phys. Chem. C*, **2015**, *119*, 3192-3198.
5. "Does enhanced oxygen activation always facilitate CO oxidation on gold clusters?" **K. Mondal**, A. Banerjee, A. Fortunelli, T. K. Ghanty. *J. Comput. Chem.*, **2015**, *36*, 2177-2187.

Conferences

1. "Tuning the properties of tetrahedral Au₂₀ cluster by Li doping" **K. Mondal**, C. Kamal, A. Chakrabarti, A. Banerjee, T. K. Ghanty, DAE-BRNS 4th Interdisciplinary Symposium on Materials Chemistry, December 11-15, **2012**, BARC, Mumbai, India.
2. "Effect of Li atom doping on the chemical reactivity of Au₂₀ cluster: A CO adsorption study" **K. Mondal**, D. Manna, A. Banerjee, T. K. Ghanty, Current Trend in Theoretical Chemistry, September 26-28, **2013**, BARC, Mumbai, India.

3. "Performance of Au_{19}X ($\text{X} = \text{Li}$ and Pt) cluster as a catalyst for CO oxidation" **K. Mondal**, A. Banerjee, T.K. Ghanty, ISCANM-III, March 11-14, **2014**, HRI, Allahabad, India.
4. "Catalytic Activity of Pt Doped Subnanometer Sized Gold Cluster" **K. Mondal**, A. Banerjee, A. Fortunelli and T. K. Ghanty, Theoretical Chemistry Symposium, December 18-21, **2014**, CSIR-NCL, Pune, India.
5. "Silicene supported gold cluster: A density functional study" **K. Mondal**, C. Kamal, A. Banerjee, A. Chakrabarti, T. K. Ghanty, Gordon Research Conferences on Clusters and Nanostructures, July 5-10, **2015**, Girona, Spain.

Krishnakanta Mondal

DEDICATION

This thesis is dedicated to my parents

ACKNOWLEDGEMENTS

The completion of the present thesis could not have been possible without the constant support and guidance of many people. First of all, I would like to thank my supervisor Prof. Arup Banerjee for his valuable guidance and encouragement throughout the tenure of my PhD. He gave me enough freedom in thinking, choosing my own research problems and collaborating with other groups which helped me to bring out my best. He never made me feel that he was my supervisor; rather he interacted with me like a friend. I discussed my professional as well as personal problems with him without any hesitation. I feel very lucky to have him as my PhD supervisor.

Next, I express my sincere gratitude to Prof. Tapan K. Ghanty for his guidance, support and encouragement. He was like my another supervisor and he guided to carry out the work in systematic manner which helped me to complete the thesis in time. He has also helped me to understand the nitty-gritty of quantum chemical calculations.

I extend my thanks to all the members of my doctoral committee for monitoring my progress during the last five years of my PhD. I am very thankful to Prof. L. M. Kukhreja, Prof. S. B. Roy and Prof. P. A. Naik for their criticism, comments and constructive suggestions which helped to improve the quality of the work presented in this thesis. I am also very thankful to Prof. S. R. Mishra, Prof. T. K. Sharma, Prof. Vinit Kumar and Prof. Anand Moorti for their support and encouragement.

I am very thankful to Prof. Aparna Chakrabarti for fruitful discussion, valuable suggestions and constant support. She also helped me in analysing the data of some of my calculations. I am also very thankful to Dr. C. Kamal with whom I started my journey in the field of computational science. I am also very thankful to Dr. Debashree Manna for her help and support. I am also highly indebted to my collaborator Prof. Alessandro Fortunelli for helpful discussions and valuable suggestions for the work on CO oxidation.

I would like to thank Prof. P. K. Gupta and Prof. H. S. Rawat for their support and encouragement. I thank to Mr. P.K. Thander for providing constant technical support in smooth running of the numerical code in the computing clusters. I also thank to RRCAT Computer Centre and BARC computer division for supplying the computing facilities.

I express my special gratitude to my teacher Prof. Somita Seal who suggested me to join PhD. I am also very thankful to my teacher Prof. Abhijit Sen and his father Prof. Prasanta Sen for their valuable suggestions to join RRCAT for pursuing PhD.

Life is incomplete without good friends. I would like to mention the names of my friends who have always provided help and support and stood behind me: Biswarup Pal, Guru Kalyan Hazra, Sasthi Pada Mondal, Gourav Chattarjee, Tanmoy Ghosh, Ranajit Mondal, Piyali Sarkar, Biplab Pal, Sandipan Dawn, Argha Chattaraj, Tanmoy Mukherjee, Subrata Mondal, Mahadev Mondal, Sushavon Lala, and Madhab Singha. During my journey in the last five years I was accompanied by Shyam, Ekta, Harish, Amol, Debu, CB (Bixmaiya Chalakani), Surya, Matin da, Saini Sir, Sanjit da, DJ (Dipankar Jana), Tufan, Ganga, Arijit, Vandana, Smritijit, Pares, Paromita, Debashis, Aditya, Gopal, Yashvir, Kintali, Sudheer, Dipanjna and Disha. Moreover, my special thank to Debashis da, Amit da, Suman da, Chiru da and Jana da who gave numerous parties which made my life joyful during my stay at RRCAT.

Finally, I express a deep sense of gratitude to my parents (Mr. Aditya Mondal and Mrs. Namita Mondal), maternal aunt (Mrs. Madhabi Mondal), aunt (Mrs. Janani Mondal), uncle (Mr. Senapati Mondal), maternal uncles and aunts, elder brother (Mr. Samar Mondal), elder sister (Mrs. Supriya Mondal) and brother-in-law (Mr. Rahul Deb Mondal) for their love, support and encouragement.

Contents

Synopsis	iii
List of Figures	xiii
List of Tables	xix
1 Introduction and Theoretical Methodology	1
1.1 Introduction	1
1.1.1 What are Clusters?	1
1.1.2 Gold	4
1.1.2.1 History of Gold	4
1.1.2.2 Properties of Gold	4
1.1.2.3 Relativistic Effect in Gold	5
1.1.2.4 Gold Clusters	6
1.1.2.5 Supported Gold Clusters	9
1.1.2.6 Heterogeneous Catalysis	11
1.2 Theoretical Methodology	13
1.2.1 Many-Body Problems	14
1.2.2 Born-Oppenhemier Approximation	15
1.2.3 Density Functional Theory	17
1.2.4 Nudged Elastic Band (NEB)	22
2 Structural and Electronic Properties of Li Doped Gold Nano-Clusters	25
2.1 Computational Details	26
2.2 Properties of $\text{Au}_{20-n}\text{Li}_n$, $n = 1$ Clusters	27
2.3 Properties of $\text{Au}_{20-n}\text{Li}_n$, $n = 2$ Clusters	29
2.3.1 Structural Properties of Tetrahedral Clusters	29
2.3.1.1 Analysis of Deformation	31
2.3.1.2 Analysis of Bond Length	32
2.3.2 Electronic Properties of Tetrahedral Clusters	32
2.3.2.1 Binding Energy	34
2.3.2.2 HOMO-LUMO gap, Ionization Potential and Electron Affinity	35
2.3.3 Properties of Cage-like $\text{Au}_{20-n}\text{Li}_n$, $n = 2$ Clusters	36
2.4 Effect of Doping of More Than Two Li Atoms	39
2.5 Density of Sates of $\text{Au}_{20-n}\text{Li}_n$, $n = 1 - 4$ Clusters	40

2.6	Vibrational Spectra of $\text{Au}_{20-n}\text{Li}_n$, $n = 1 - 4$ Clusters	41
2.7	Conclusions	43
3	Chemical Properties of Li Doped Gold Nano-Clusters	45
3.1	Computational Details	46
3.2	Structural Properties of Au_{19}Li -CO Complexes	47
3.3	Interaction of CO Molecule with Au_{19}Li Clusters	52
3.3.1	Adsorption of CO on Tetrahedral Au_{19}Li Clusters	53
3.3.2	Adsorption of CO on Cage-like Au_{19}Li Clusters	55
3.3.3	Electronic Structure of Cluster-CO Complexes	56
3.4	Conclusions	59
4	Structural and Chemical Properties of Pt Doped Gold Nano-Clusters	61
4.1	Structural and Electronic Properties of Bimetallic Au_{19}Pt Clusters	63
4.1.1	Properties of Tetrahedral Isomers of Au_{19}Pt Cluster	64
4.1.2	Properties of Cage-like Isomers of Au_{19}Pt Cluster	69
4.2	Chemical Properties of Bimetallic Au_{19}Pt Clusters	72
4.3	Conclusions	80
5	Catalytic Activity of Pt Doped Gold Nano-Clusters	83
5.1	Computational Details	84
5.2	Isomers of Au_{19}Pt Cluster	84
5.3	Adsorption of O_2 on Au_{19}Pt Clusters	84
5.4	Coadsorption of CO and O_2 on Td-E Isomer of Au_{19}Pt Cluster	89
5.5	Oxidation Reaction of CO on Td-E Isomer of Au_{19}Pt Cluster	91
5.6	Coadsorption of CO and O_2 on Td-S Isomer of Au_{19}Pt Cluster	95
5.7	Oxidation Reaction of CO on Td-S Isomer of Au_{19}Pt Cluster	97
5.8	Conclusions	99
6	Gold Clusters on Silicene: Morphology Transformation	101
6.1	Computational Details	103
6.2	Validation of Theoretical Methodology	104
6.3	Adsorption of Smaller Gold Clusters on Silicene	105
6.4	Adsorption of Larger Gold Clusters on Silicene	109
6.5	Conclusions	113
7	Summary	115
	Bibliography	119

Synopsis

The properties of the materials change drastically as we go from bulk to nano-dimension. It is due to the fact that the nano-materials like nano-particles and nano-clusters have large surface to volume ratio which strongly influences their physical and chemical properties. The pioneering work of Haruta *et al.* [1] on the catalytic activity of the tiny gold particles has motivated large number of theoretical and experimental works to understand the catalytic properties of these nano-particles and nano-clusters although passive nature of bulk gold is well known to us. The gold nano-clusters are also found to have potential applications in molecular electronics and optical devices as well as medical and biological diagnostics [2–12]. It is reported that the size of the gold clusters has major effect on their chemical activity as depending on the size, the geometric and electronic properties evolve significantly. The smaller gold clusters exhibit high reactivity towards CO and O₂ molecules, while the reactivity decreases as the size of the cluster increases. Lopez-Acevedo *et al.* [13] reported that the chemical reactivity of the gold clusters reaches the inert bulk value when the number (n) of atoms in the gold clusters reaches 144. However, it has been found that the catalytic activity of the larger sized gold clusters can be enhanced by incorporating some other atoms, thereby forming bimetallic clusters [14]. Moreover, the geometric and electronic properties of the bimetallic clusters can be modified by varying the particle size, composition and the support, thereby offering tunable catalytic property. To this end, it has been observed that the presence of Li and Pt atoms in gold clusters can enhance the catalytic activity of the gold clusters [7, 15–21]. Most of these earlier reports are restricted to the investigation on the smaller gold clusters having number of atoms less than

13. The detailed study to understand the effect of the doping of Li and Pt atoms on chemical property of the larger gold clusters is scanty in the literature.

In the family of gold clusters Au_{20} cluster with sub-nanometer size (size ~ 0.8 nm) possesses a unique characteristic due to its symmetric tetrahedral structure, which is both energetically and chemically stable in nature [22, 23]. Due to its remarkable properties a large number of theoretical and experimental investigations have been carried out to analyze the novel chemical [7, 24–29] and optical [30–35] properties of this magic cluster. It has been observed that the neutral Au_{20} cluster interacts very weakly with CO and O_2 molecules [7, 25]. However, Molina *et al.* found that presence of alkali atoms in Au_{20} cluster can enhance the affinity of this cluster towards CO and O_2 [7]. Moreover, these authors observed that the deposition of the Au_{20} cluster on defect rich MgO surface weakly enhances the chemical reactivity of this cluster. Here, we wish to point out that the incorporation of alkali atoms inside the cage of the tetrahedral Au_{20} may disturb the symmetry and the magic number configuration of this noble cluster. With an objective to retain the tetrahedral geometry and the magic nature of Au_{20} cluster, recently our group has carried out a detail investigation on the structural and electronic properties of M atom ($\text{M} = \text{Li}, \text{Na}, \text{K}, \text{Cs}, \text{Rb}, \text{Cu}$ and Ag) doped 20-atom gold cluster [36]. It has been observed that the Li doping leads to the most stable Au_{19}Li cluster which has binding energy larger than that of the pure Au_{20} cluster. Moreover, the energy gap between the highest occupied molecular orbital (HOMO) and lowest unoccupied molecular orbital (LUMO) is lower than that of the pure Au_{20} . These results indicate that the 20-atom gold clusters doped with Li atoms may have interesting structural and chemical properties. In order to explore this, in the present thesis we theoretically investigate the structural and chemical properties of the multiple Li atoms doped 20-atom gold cluster. Furthermore, to understand the effect of transition metal atom on the structural and chemical properties of the 20-atom gold cluster we choose Pt atom to dope in Au_{20} . To check the chemical reactivity of the doped clusters we use CO as a probe and investigate the CO adsorption behavior of the doped clusters. The comparison between the adsorption of CO molecule studies on Li and Pt atoms doped clusters indicates that the Pt atom doped gold cluster may exhibit efficient catalytic activity for the oxidation of CO. This aspect

of the Pt atom doped cluster has been systematically investigated by calculating the reaction paths for oxidation of CO and the corresponding barriers and thermodynamic properties which govern the reaction mechanism.

In order to understand the effect of supports on the structural and chemical properties of the gold clusters we study the adsorption of various gold clusters on silicene (silicon analogue of graphene). Note that silicene is a newly discovered graphene-like two-dimensional honeycomb structure made up of silicon and it has recently been experimentally grown successfully on Ag(111) surface [37]. We wish to mention that presently silicene has also been grown on various surfaces like ZrB₂(0001), Au(110) and Ir(111) etc [38–40]. In the present thesis we propose silicene as a suitable surface to stabilize the energetically less stable but catalytically more active gold clusters. The organization of the thesis is given below.

In **Chapter 1** of the thesis, we provide an overview of the noble properties of the pure and doped gold clusters. It is then followed by a brief introduction to the computational methods employed for the calculations of electronic structure based on density functional theory (DFT). Here, we also describe the nudged elastic band (NEB) method which is used to calculate the reaction paths and barriers for the oxidation reaction of the CO molecule.

Structural and electronic properties of 20-atom gold cluster (Au₂₀) doped with Li atoms (Au_{20-n}Li_n, n = 1 - 4) are described in **Chapter 2**. These calculations have been carried out using relativistic density functional theory within the framework of zeroth-order regular approximation (ZORA) [41, 42]. For this purpose various initial structures have been generated and employed for the geometry optimization followed by vibrational analysis to check the stability of the final optimized structures. We have calculated various properties like binding energy, ionization potential, electron affinity and HOMO-LUMO gap of these structures. It has been found that the dopant Li atoms always favor to occupy the surface positions of the pyramidal Au₂₀ cluster. The binding energies of the surface-doped Au_{20-n}Li_n clusters are always higher than that of the pure Au₂₀ cluster. However, the HOMO-LUMO gap, which is used to define the chemical stability

of the clusters, shows an interesting behavior. For $n = 1$ HOMO-LUMO gap (1.671 eV) decreases as compared to that of the pure Au_{20} cluster (1.786 eV). For $n = 2$, the HOMO-LUMO gap becomes comparable to that of pure Au_{20} and for $n > 2$ the HOMO-LUMO gap increases beyond its value for pure Au_{20} cluster. Interestingly, we find that the doped tetrahedral $\text{Au}_{16}\text{Li}_4$ cluster, where all the dopants are at the surface sites, possesses a very high HOMO-LUMO gap of 2.117 eV, which is 0.331 eV higher than that of pure Au_{20} cluster. It is important to note here that the geometric and energetic parameters indicate that $\text{Au}_{16}\text{Li}_4$ cluster may be considered as a possible ‘superatom’ in the design of novel cluster-assembled material. Moreover, as the lower value of HOMO-LUMO gap indicates the higher chemical reactivity of the clusters, it is then expected that the single Li doped Au_{19}Li cluster will be more reactive than pure Au_{20} cluster. Hence, in the next chapter the chemical reactivity of the Au_{19}Li cluster is investigated using the adsorption of CO molecule as a probe.

To check the chemical reactivity of the Au_{19}Li cluster the adsorption of a single CO molecule on various isomers of this cluster has been investigated in **Chapter 3** using the same level of theory as described in **Chapter 2**. For a particular isomer, initial geometries of CO adsorbed Au_{19}Li clusters are obtained by placing a CO molecule at each of the non-equivalent positions. It is observed that Li doping can enhance the adsorption energy of CO on Au_{19}Li cluster over that of pure Au_{20} cluster. Moreover, our study reveals that the endohedrally doped cage-like Au_{19}Li clusters show better propensity to adsorb CO than the corresponding exohedrally doped tetrahedral isomers. Furthermore, elongation of C-O bond length and the red-shift in C-O stretching frequency have been observed for some of the isomers with high value of adsorption energy. Our results indicate that the endohedrally doped cage-like Au_{19}Li clusters may be better catalytic agent than the pure Au_{20} cluster for CO oxidation.

In **Chapter 4** we carry out an investigation on the structural and chemical properties of the Pt atom doped subnanometer sized bimetallic Au_{19}Pt cluster within the framework of the relativistic density functional theory. It is observed that unlike Au_{19}Li clusters all isomers of the tetrahedral Au_{19}Pt cluster are energetically more stable as compared to the pure Au_{20} as well as cage-like isomers of Au_{19}Pt cluster. The high stability of the bimetallic Au_{19}Pt cluster can be

attributed to the strong interaction of the Au and Pt atoms, which is caused by the hybridization of s- and d-orbitals of guest Pt and the host Au atoms in the energy span of 5 eV below the HOMO level. To explore the chemical reactivity of the isomers of bimetallic Au₁₉Pt cluster, we investigate the adsorption behavior of a CO molecule on various non-equivalent sites of these isomers. We calculate CO adsorption energy, C-O bond length and bond stretching frequency for all the possible cluster-CO complexes. We find that a CO molecule is preferably adsorbed on Pt sites when both Au and Pt sites are exposed for the adsorption. Interestingly, we observe that the CO adsorption energy increases by more than 1.3 eV when a CO molecule gets adsorbed on Pt site in tetrahedral Au₁₉Pt cluster as compared to the adsorption on corresponding Au atoms in pure Au₂₀ cluster. Moreover, we have shown that due to the charge transfer from the cluster to CO molecule C-O bond length increases by around 0.02 Å, which causes a significant amount of red shift (104 - 121 cm⁻¹) in C-O stretching frequency. These results indicate that the electronic structure of CO molecule is highly disturbed when it is adsorbed on the bimetallic clusters, which in turn suggests that the oxidation of adsorbed CO molecule becomes easy.

To explore the oxidation of CO molecule on the subnanometer sized Au₁₉Pt cluster, in **Chapter 5** we calculate the reaction paths and the corresponding barriers and thermodynamic functions which govern the reaction mechanism in heterogeneous catalysis. For this purpose we consider two structurally similar isoenergetic isomers of Au₁₉Pt cluster and calculated the complete reaction paths corresponding to CO oxidation on these clusters. It is observed that the CO oxidation on one isomer occurs through a smaller reaction barrier (0.377 eV) as compared to that on the other isomer (0.702 eV), although the activation of O₂ on the latter is much higher than that on the former. Hence, it is very clear that the higher O₂ activation, which is generally believed to be the key factor for CO oxidation, solely cannot determine the efficiency of a catalyst. This is because of the fact that the adsorption of CO on the isomer which is capable of higher O₂ activation is stronger by around 0.4 eV as compared to that on the isomer capable of lower O₂ activation. Results presented in this work would be valuable in designing gold based novel nanocatalysts.

With an objective to stabilize the energetically less stable but catalytically more active planar form of finite sized gold clusters on some suitable solid support, in **Chapter 6** we have theoretically investigated the morphology transformation of gold dimer, trimer and Au_{20} cluster on pristine silicene/ $\text{Ag}(111)$ surface. In contrast to the previous schemes which have been suggested for the stabilization of planar structures by appropriate surfaces, the present proposal does not require any external influence such as doping or application of external electric field. In fact, we have exploited the special characteristics of the silicene surface, namely, buckled nature and weak Si-Si π bonding, which enable this surface to make strong Si-Au covalent bonds resulting into the two-dimensional planar Au_{20} isomer as more stable over its three-dimensional tetrahedral structure. In contrast to this, as already reported in the literature, the planar isomer of Au_{20} cluster is not energetically favored when it is adsorbed on a pure graphene surface. Moreover, Bader charge density analysis indicates that the amount of charge transfer from silicene surface to the planar Au_{20} cluster is considerably high, thereby increasing the possibility of enabling this composite system to act as a better catalyst. It would be interesting to investigate the adsorption of gold clusters on silicene surface experimentally for the verification of our theoretical prediction.

In **Chapter 7** we summarize the thesis followed by a brief discussion on the future work.

References for synopsis

- [1] Haruta, M.; Kobayashi, T.; Sano, H.; Yamada, N. *Chem. Lett.* **1987**, *16*, 405.
- [2] Heiz, U.; Landman, U. *Nanocatalysis*; Springer-Verlag, Berlin, 2007.
- [3] Sanchez, A.; Abbet, S.; Heiz, U.; Schneider, W. D.; Häkkinen, H.; Barnett, R. N.; Landman, U. *J. Phys. Chem. A* **1999**, *103*, 9573.
- [4] Yoon, B.; Häkkinen, H.; Landman, U.; Wörz, A. S.; Antonietti, J. M.; Abbet, S.; Judai, K.; Heiz, U. *Science* **2005**, *307*, 403.
- [5] Yoon, B.; Koskinen, P.; Huber, B.; Kostko, O.; van Issendorff, B.; Häkkinen, H.; Moseler, M.; Landman, U. *ChemPhysChem* **2007**, *8*, 157.
- [6] Heiz, U.; Schneider, W. D. *J. Phys. D* **2000**, *33*, R85.
- [7] Molina, L. M.; Hammer, B. *J. Catal.* **2005**, *233*, 399.
- [8] Haruta, M. *Catal. Today* **1997**, *36*, 153.
- [9] Pyykkö, P.; Runeberg, N. *Angew. Chem. Int. Ed.* **2002**, *41*, 2174.
- [10] Shaw, C. F. *Chem. Rev.* **1999**, *99*, 2589.
- [11] Wu, D.; Zhang, Z. D.; Liu, P. X.; Zhang, L. A.; Fan, F. Y. *Curr. Nanosci.* **2011**, *7*, 110.
- [12] Huang, X.; El-Sayed, H. I.; Quian, W.; Ei-Sayed, M. A. *J. Am. Chem. Soc.* **2005**, *128*, 2115.

-
- [13] Lopez-Acevedo, O.; Kacprzak, K. A.; Akola, J.; Häkkinen, H. *Nat. Chem.* **2010**, *2*, 329.
- [14] Liu, J. H.; Wang, A. Q.; Chi, Y. S.; Lin, H. P.; Mou, C. Y. *J. Phys. Chem. B* **2005**, *109*, 40.
- [15] Deka, A.; Deka, R. C. *Appl. Nanosci.* **2012**, *2*, 359.
- [16] Jena, N. K.; Chandrakumar, K. R. S.; Ghosh, S. K. *J. Phys. Chem. C* **2009**, *113*, 17885.
- [17] Song, C.; Ge, Q. *J. Phys. Chem. B* **2005**, *109*, 22341.
- [18] Sadek, M. M.; Wang, L. *J. Phys. Chem. A* **2006**, *110*, 14036.
- [19] Ge, Q.; Song, C.; Wang, L. *Comput. Mater. Sci.* **2006**, *35*, 247.
- [20] Morrow, B. H.; Resasco, D. E.; Striolo, A.; Nardelli, M. B. *J. Phys. Chem. C* **2011**, *115*, 5637.
- [21] Tian, W. Q.; Ge, M.; Gu, F.; Yamada, T.; Aoki, Y. *J. Phys. Chem. A* **2006**, *110*, 6285.
- [22] Wang, J.; Wang, G.; Zhao, J. *Chem. Phys. Lett.* **2003**, *380*, 716.
- [23] Gruene, P.; Rayner, D. M.; van der Meer, A. F. G.; Lyon, J. T.; Meijer, G.; Fielicke, A. *Science* **2008**, *321*, 674.
- [24] De Haeck, J.; Veldeman, N.; Claes, P.; Janssens, E.; Andersson, M.; Lievens, P. *J. Phys. Chem. A* **2011**, *115*, 2103.
- [25] Gao, Y.; Shao, N.; Pei, Y.; Chen, Z.; Zeng, X. C. *ACS Nano* **2011**, *5*, 7818.
- [26] Neumaier, M.; Weigend, F.; Hampe, O.; Kappes, M. M. *J. Chem. Phys.* **2005**, *122*.
- [27] Beletskaya, A. V.; Pichugina, D. A.; Shestakov, A. F.; Kuźmenko, N. E. *J. Phys. Chem. A* **2013**, *117*, 6817.
- [28] Nijamudheen, A.; Datta, A. *J. Phys. Chem. C* **2013**, *117*, 21433.
- [29] Li, Z.; Chen, Z. X.; He, X.; Kang, G. J. *J. Chem. Phys.* **2010**, *132*, 184702.
- [30] Wu, K.; Li, J.; Lin, C. *Chem. Phys. Lett.* **2004**, *388*, 353

-
- [31] Aikens, C. M.; Schartz, G. C. *J. Phys. Chem. A* **2006**, *110*, 13317.
- [32] Idrobo, J. C.; Walkosz, W.; Yip, S. F.; Ogut, S.; Wang, J.; Jellinek, J. *Phys. Rev. B* **2007**, *76*, 205422.
- [33] Tlahuice-Flores, A. *J. Mol. Model.* **2013**, *19*, 1937.
- [34] Koppen, J. V.; Hapka, M.; Szczniak, M. M.; Chaasiski, G. *J. Chem. Phys.* **2012**, *137*, 114302.
- [35] Kryachko, E. S.; Remacle, F. *Int. J. Quantum Chem.* **2007**, *107*, 2922.
- [36] Ghanty, T. K.; Banerjee, A.; Chakrabarti, A. *J. Phys. Chem. C* **2010**, *114*, 20.
- [37] Vogt, P.; Padova, P. D.; Quaresima, C.; Avila, J.; Frantzeskakis, E.; Asensio, M. C.; Resta, A.; Ealet, B.; Lay, G. L. *Phys. Rev. Lett.* **2012**, *108*, 155501.
- [38] Fleurence, A.; Friedlein, R.; Ozaki, T.; Kawai, H.; Y., W. *Phys. Rev. Lett.* **2012**, *108*, 245501.
- [39] Enriquez, H.; Mayne, A.; Kara, A.; Vizzini, S.; Roth, S.; Lalmi, B.; Seitsonen, A. P.; Aufray, B.; Greber, T.; Belkhou, R.; Dujardin, G.; Oughaddou, H. *Appl. Phys. Lett.* **2012**, *101*, 021605.
- [40] Meng, L.; Wang, Y.; Zhang, L.; Du, S.; Wu, R.; Li, L.; Zhang, Y.; Li, G.; Zhou, H.; Hofer, W. A.; Gao, H. *J. Nano Lett.* **2013**, *13*, 685.
- [41] van Lenthe, E.; Baerends, E. J.; Snijders, J. G. *J. Chem. Phys.* **1993**, *99*, 4597.
- [42] van Lenthe, E.; Baerends, E. J.; Snijders, J. G. *J. Chem. Phys.* **1994**, *101*, 9783.

List of Figures

1.1	Relativistic contraction of the 6s orbital of the elements Cs to Fm. This is calculated from $\langle r_{6s} \rangle_{\text{relativistic}} / \langle r_{6s} \rangle_{\text{non-relativistic}}$ and shows a maximum contraction at gold.	5
1.2	Gold clusters (Au_n) in the size range $n = 2 - 32$	7
1.3	Optimized geometry of pure Au_{20} cluster.	8
1.4	Single sheets of (a) silicene and (b) graphene.	10
1.5	Role of a catalyst.	11
1.6	Cartoon picture for (a) LH mechanism, and (b) ER mechanism for oxidation reaction of CO molecule.	13
2.1	Optimized geometries of tetrahedral and cage-like Au_{19}Li clusters.	28
2.2	Optimized geometries of pyramidal doped $\text{Au}_{18}\text{Li}_2$ clusters in decreasing order of BE. The values within the parenthesis indicate the relative BE (in eV) with respect to the most stable structure Td(S-S) which has been denoted in the figure as (S-S). The symbol $(\text{X-Y})_m$ indicates the cluster $\text{Td}(\text{X-Y})_m$, where X and Y represent the locations of the dopant atoms at S (surface), V (vertex), and E (edge) and m is an integer which indicates the serial number of different X-X, Y-Y and X-Y combinations.	30

2.3	Optimized geometries of cage-like doped $\text{Au}_{18}\text{Li}_2$ clusters ((C1)-(C15)) in decreasing order of BE. The values within the parentheses indicate the relative BE (in eV) with respect to the isomer $\text{Au}_{18}\text{Li}_2(\text{C1})$ which is represented in the figure as (C1).	37
2.4	Total DOS (blue) of the $\text{Au}_{20-n}\text{Li}_n$ ($n = 0 - 4$) clusters and partial DOS (green) of Li atom in the corresponding cluster: (a) Au_{20} , (b) Td-S, (c) Td(S-S), (d) Td(S-S-S), and (e) Td(S-S-S-S). The calculations of DOS have been carried out using a Lorentzian broadening of 0.1 eV. The dashed line indicates HOMO of the doped clusters. Note that to visualize the small value of the partial DOS of Li atom we use two separate y-axes for total DOS (left side) and partial DOS (right side) with different scaling.	40
2.5	IR-spectra of $\text{Au}_{20-n}\text{Li}_n$ ($n = 0 - 4$) clusters: (a) Au_{20} , (b) Td-S, (c) Td(S-S), (d) Td(S-S-S), and (e) Td(S-S-S-S). These spectra are broadened by a Gaussian having a width of 1 cm^{-1} . The vertical arrows in the panel (b) to (e) indicate the positions of the Au-derived peaks.	41
3.1	Optimized geometries of Au_{19}Li clusters. The arrows indicate the non-equivalent positions for CO molecule adsorption. The numbers within the parenthesis indicate the relative energies (eV) of the corresponding structure with respect to the most stable Td-S cluster. The relative binding energies presented here are calculated using PBE functional.	47
3.2	Energy level diagram of Au_{19}Li and Au_{20} clusters. The top most level below -4.75 eV is the HOMO and the bottom most level above -4.25 eV is the LUMO of the clusters.	49
3.3	Optimized geometries of the tetrahedral $\text{Au}_{19}\text{Li-CO}$ complexes.	50
3.4	Optimized geometries of the cage-like $\text{Au}_{19}\text{Li-CO}$ complexes.	52

3.5	Energy level diagram of Cg2 and Cg2_1 clusters.	58
4.1	Optimized geometries of pyramidal bimetallic Au ₁₉ Pt clusters in decreasing order of BE. The values within the parentheses indicate the relative energy (in eV) of the corresponding structures. Here, the relative energy (in eV) is calculated with respect to the most stable Td-S structure.	64
4.2	Representation of HOMO of spin down electrons corresponding to the tetrahedral Au ₁₉ Pt clusters.	67
4.3	Magnetization density (spin-up charge density - spin-down charge density) plot of Td-S, Td-E and Td-V clusters.	68
4.4	PDOS for s- and d-orbitals of Au (dashed lines) and Pt (solid lines) atoms in Td-S (a), Td-E (b) and Td-V (c) clusters.	69
4.5	Optimized geometries of cage and tube like Au ₁₉ Pt clusters in the decreasing order of BE. The values within the parentheses indicate the relative energy (in eV) of the corresponding structures. Here, the relative energy (in eV) is calculated with respect to the most stable Td-S structure.	70
4.6	Optimized geometries of pyramidal Au ₁₉ Pt-CO complex.	74
4.7	PDOS of s-and p-orbitals of CO (dashed line) and s- and d-orbitals of Pt atom (solid line) in (a) Td-S-S1, (b) Td-E-E1 and (c) Td-V-V1 complexes.	79
5.1	Optimized geometries of the Au ₁₉ Pt-O ₂ complexes	86
5.2	Adsorption energy vs d-band centre plot for some selected (a) cluster-O ₂ and (b) cluster-CO complexes. Here d-band centre is calculated with respect to the HOMO.	89

5.3	Partial reaction path for oxidation of CO on Td-E isomer of Au ₁₉ Pt cluster. ΔE and ΔG (in eV) indicate respectively, the reaction energy and Gibbs free energy calculated between the partial reactants and products.	92
5.4	Partial reaction path for oxidation of CO on pure Au ₂₀ cluster. ΔE (in eV) indicate the reaction energy calculated between the partial reactants and products.	93
5.5	Complete reaction path for oxidation of CO on Td-S isomer of Au ₁₉ Pt cluster. ΔE and ΔG (in eV) indicate respectively, the reaction energy and Gibbs free energy calculated between the partial reactants and products	96
5.6	Partial density of state (PDOS) corresponding to the p-orbital of the O ₂ molecule. Black and blue curves indicate the p-orbital of the adsorbed O ₂ for the CO+O ₂ coadsorption on Td-E and Td-S respectively. Red curve corresponds to the p-orbital of the free O ₂ molecule. The horizontal arrows indicate the shifting direction of the anti-bonding orbitals of the free O ₂ molecule. The vertical dotted line denotes the HOMO	97
6.1	(a) top view, (b) side view of the free-standing hexagonal buckled 4 × 4 unit cell of silicene surface.	102
6.2	Difference charge density (ρ_{diff}) with isosurface value of 0.003 e/Å ³ : (a) top view, (b) side view for Au/silicene/Ag(111) system. Red and green indicate respectively the accumulation and depletion of charge. Gray, blue and yellow balls represent Ag, Si and Au atoms, respectively.	106

- 6.3 (a) horizontal, (b) vertical configurations for Au₂ and (c) horizontal, (d) vertical configurations for Au₃, all are placed on silicene/Ag(111) surface. The values at the bottom indicate the relative energies of the respective configurations. The relative energy (E_r , in eV) values are calculated with respect to the horizontal configuration of the respective cluster. The values outside the square bracket are obtained with PBE XC-functional and the numbers within the square bracket are calculated using PBE + D2 method. Gray, blue and yellow balls represent Ag, Si and Au atoms, respectively. 107
- 6.4 Optimized geometries: (a) Au₂₀-P and (b) Au₂₀-T, both are placed on silicene/Ag(111) surface. The values at the bottom indicate the relative energies of the respective configurations. The relative energy (E_r , in eV) values are calculated with respect to Au₂₀-P. The values outside the square bracket are obtained with PBE XC-functional and the numbers within the square bracket are calculated using PBE + D2 method. Gray, blue and yellow balls represent Ag, Si and Au atoms, respectively. 110
- 6.5 Difference charge density (ρ_{diff}) with isosurface value of 0.002 e/Å³: (a) top view and (b) side view for Au₂₀-P, and (c) top view and (d) side view for Au₂₀-T, both adsorbed on silicene/Ag(111) surface. Red and green indicate, respectively, the accumulation and depletion of charges. Gray, blue and yellow balls represent Ag, Si and Au atoms, respectively. 112

List of Tables

2.1	Principle value for R_{ij} tensor of optimized pyramidal doped $\text{Au}_{18}\text{Li}_2$ clusters along with Au_{20} (T_d) cluster. All the values are given in \AA^2	31
2.2	Average nearest neighbor distance (in \AA) between Au atom and Li atom in the pyramidal doped $\text{Au}_{18}\text{Li}_2$ structures with the corresponding Au-Au distance in Au_{20} (T_d) cluster(first row). The values within the parenthesis indicate the range of the corresponding distances. In this table d_{X-Y} denotes distance between two atoms located at X and Y, where X, Y stand for S, V and E positions. Furthermore, in this table d_{E-E}^1 and d_{E-E}^2 denote distances between two atoms which lie on the different edges and on the same edge respectively.	33
2.3	Symmetry, binding energy (BE), energy gap between HOMO and LUMO (Δ_{HL}), vertical ionization potential (VIP) and vertical electron affinity (VEA) for exohedrally doped pyramidal $\text{Au}_{18}\text{Li}_2$ clusters along with Au_{20} (T_d) cluster. All the units are in eV.	34
2.4	Symmetry, binding energy (BE), energy gap between HOMO and LUMO (Δ_{HL}), vertical ionization potential (VIP) and vertical electron affinity (VEA) for doped cage-like $\text{Au}_{18}\text{Li}_2$ clusters along with Au_{20} (T_d) cluster. All the units are in eV.	37
2.5	Symmetry, binding energy (BE), energy gap between HOMO and LUMO (Δ_{HL}) and vertical ionization potential (VIP) for Au_{20} and $\text{Au}_{20-n}\text{Li}_n$ ($n = 1 - 4$) clusters. All the units are in eV.	39

3.1	Relative energies (in eV) of the five isomers of Au ₁₉ Li cluster.	48
3.2	Adsorption energy (E_{ad}), the distance between Au and C and C-O bond length (d_{Au-C} and d_{C-O} respectively) and Au-C and C-O bond stretching frequencies (ν_{Au-C} and ν_{C-O} respectively) for Au ₂₀ -CO complex.	53
3.3	Adsorption energy (E_{ad}) for the tetrahedral Au ₁₉ Li-CO complexes	54
3.4	Adsorption energy (E_{ad}) for the cage-like Au ₁₉ Li-CO complexes	55
3.5	Mulliken charges, the Au-C bond distance (d_{Au-C}) and C-O bond length (d_{C-O}), Au-C and C-O bond stretching frequencies (ν_{Au-C} and ν_{C-O} respectively) for the selected Au ₁₉ Li-CO complexes.	57
4.1	Calculated and experimental values of the binding energy, bond length and bond stretching frequency of Au ₂ , AuPt dimers and CO molecule.	63
4.2	Bond length between Pt atom and its nearest neighbor Au atom. ^a	65
4.3	Binding energy, HOMO-LUMO gap, and magnetic moment of the pure (Td-0) and bimetallic tetrahedral Au ₁₉ Pt cluster.	66
4.4	Binding energies of the bimetallic Au ₁₉ Pt clusters with different XC functionals and spin states.	71
4.5	Bond length and bond stretching frequency of the cluster-CO complexes.	75
4.6	Mulliken Charge on Pt Site and the Total Charge on the Adsorbed CO Molecule.	76
4.7	CO Adsorption energy (in eV) for the pure and the bimetallic Au ₁₉ Pt clusters.	77
5.1	O-O bond lengths (R_{O-O}), corresponding stretching frequencies (ν_{O-O}) and the atomic charges (Q_{O_2}) on the adsorbed O ₂ for the selected tetrahedral Au ₁₉ Pt-O ₂ complexes along with the corresponding values for a free O ₂ molecule	85

5.2	Adsorption energy (E_{ad}) of O_2 and CO on the various isomers of $Au_{19}Pt$ cluster	88
5.3	O-O bond length (R_{O-O}), its stretching frequency (ν_{O-O}) and atomic charge on O_2 (Q_{O_2}) in the CO+ O_2 coadsorbed and only O_2 adsorbed structures.	90
6.1	Calculated Results for the Adsorption of a Single Au Atom on the Free-standing Silicene along with the Corresponding Reported Values	105
6.2	Interaction energies with and without Grimme's dispersion correction, and average Au-Au and Au-Si bond distances (d_{Au-Au} and d_{Au-Si} , respectively) for the deposited Au_n ($n = 2, 3$) clusters for two different adsorption configurations (horizontal and vertical) along with the average Au-Au bond distances (d_{Au-Au}^g) and binding energies (E_b) of the gas phase Au_n ($n = 2, 3$) clusters	108

Chapter 1

Introduction and Theoretical Methodology

1.1 Introduction

1.1.1 What are Clusters?

According to the Oxford dictionary the term 'cluster' means "a group of things of the same type that grow or appear close together". To the scientific community cluster is an aggregate of a countable number ($2 - 10^n$, where n can be very high like 6 or 7) of identical or dissimilar particles (atoms or molecules). The aggregate generated from identical atoms (molecules) is known as a homo-atomic (homo-molecular) cluster, while the collection of dissimilar atoms (molecules) is called a hetero-atomic (hetero-molecule) cluster. The homo-atomic (homo-molecular) cluster is represented as A_n , where n indicates the number of A atoms (molecules) present in the cluster. In hetero-atomic (hetero-molecule) cluster two or more than two types of different atoms (molecules) are present and hence can be represented as A_nB_m , where n and m indicate the number of two different A and B atoms (molecules), respectively. The atoms and molecules as well as the bulk materials have been studied by physicist and the chemists and their basic properties are now fairly well understood. However, clusters, which lie in a domain between these two extremes show interesting properties which are distinctly different from their

bulk counterparts. This is due to the size of the cluster leading to electron confinement and high surface to volume ratio i.e, a large fraction of the constituent particles lie on the surface. With the advancement of sophisticated experimental methods and characterization techniques, clusters of different sizes have been synthesized and their properties have also been investigated. Along with these experimental techniques the progress in *ab-initio* density functional theory (DFT) based computational techniques have enriched the field of cluster science. Generally, clusters are classified broadly into four categories namely, van-der-Waals, covalent, ionic, and metallic clusters in accordance with the nature of bonding between the constituent particles. For details we refer to the books by Alonso [1] and Johnston [2].

In the van-der-Waals clusters the interactions between the constituent particles are weak and can be described accurately by a pair of forces. The strength of the binding energy for van der Waals cluster is about 0.3 eV per atom or less. Due to the simple central force the most stable clusters are those with high atomic density, that is, with a close-packing of atoms in icosahedral arrangements. On the other hand, covalent clusters are the aggregate of the covalently bonded atoms of the elements with strong binding energy, typically between 1.0 to 4.0 eV per atom or more. For example, the clusters formed by the members of group IV (C, Si, Ge) fall in this category. For ionic cluster the binding energy between the constituent particles is found to be 2.0 - 4.0 eV per atom. Here, the constituent units can be considered as the ionically bonded molecules. The cohesion among the constituent units can be described by potentials composed of an attractive part due to electrostatic monopole forces and a repulsive part from the quantum mechanical overlap of the electronic clouds of ions with filled electronic shells. Some of the well known clusters belonging to this category are $(\text{NaF})_n$, $(\text{NaCl})_n$, $(\text{CaF}_2)_n$ etc. In metal clusters the bonding arises due the overlap of the delocalized valance electrons of the constituent particles. The strength of the binding energy of the metal clusters ranges from a moderate value of around 0.5 eV per atom to a high value of 3.0 eV per atom. The clusters formed by alkali, alkaline earth and transition metal elements are typical members of this category.

Among all the clusters the metal clusters are widely investigated due to their interesting structural, chemical, optical and magnetic properties [1, 3]. Since the valance electrons of the *sp*

metal (alkali and alkaline earth) atoms are delocalized, the electronic density extends more or less smoothly over the whole cluster. As a result, the jellium model can be applied to these clusters to understand their electronic shell structures [4, 5]. However, the localized nature of *d* electrons present in the transition metal atoms make the corresponding clusters significantly more complex than the clusters of the *sp* elements. Part of the interest in transition metals clusters comes from their potential use in catalysis, and in fact, their reactivity with different molecular species has been studied. Another topic of great interest deals with the magnetic properties, especially the nature of the magnetic ordering and its evolution with the size of the clusters. From the catalysis point of view both the pure and doped gold nano-clusters have exhibited promising catalytic activity for several important reactions like CO combustion, propylene epoxidation, nitrogen oxide reduction, methanol synthesis, water–gas shift etc [6–9]. Besides, catalysis gold clusters have also been shown to possess potential application in molecular electronics and optical devices as well as medical and biological diagnostics [10–13]. Due to these interesting properties the gold nano-clusters have attracted considerable attention of both theoreticians and experimentalists. It is observed that the properties of the gold clusters strongly depend upon the shape and size of the clusters. Moreover, the properties of the gold clusters can be modified with the help of doping with various alkali, transition and coinage metal atoms. The presence of impurity atoms in doped gold clusters provides a knob to tune the geometric and electronic properties of these bimetallic clusters. Consequently, the various properties of these clusters can be altered in a desirable manner. In particular, the catalytic activity of the gold clusters gets enhanced when one or more suitable alkali and transition metal atoms are doped in the cluster [14–16]. Another possible scheme to modify the catalytic activity of gold clusters is to deposit these clusters on some suitable solid supports [17]. The change in the catalytic activity of the deposited cluster is attributed to the charge transfer from surface to the cluster or vice-versa. However, due to the computational complexity, the work on the larger doped gold clusters are limited in the literature, in particular, alkali (Li) and transition (Pt) metal atoms doped 20 atoms gold clusters are not explored much [18, 19]. In the present thesis we have focused our attention on this size range and systematically investigated the structural and chemical properties of the Li and Pt atoms doped 20-atom gold cluster [20–22]. Furthermore, we have also explored the

catalytic activity of the Pt atom doped 20-atom gold cluster by performing the oxidation reaction of CO molecule on it [23]. In addition, in the present thesis we have shown that silicene can be used as a support to stabilize the catalytically active but energetically less stable gold clusters [24]. In the following we give a brief description of various important properties of bulk gold and its nano-clusters.

1.1.2 Gold

1.1.2.1 History of Gold

The symbol used for gold is Au, which is derived from the Latin word aurum meaning shining dawn. Gold is considered to be very precious metal due to its shining color and this was the first metal used by man [25]. The early uses of gold were in coinage and jewellery. Lydian merchants (now west Turkey) were the first to use gold as a form of coins in around 700 B.C. These coins were prepared from the lumps of a mixture of gold and silver which is known as “electrum”. Later on the price of gold was too high for regular circulation and then cheaper metals such as copper replaced gold. Gold is highly coveted and priced due to its noble non-tarnishing property. Presently, gold is also used in electronic circuitry [26, 27] and in medicine [28]. Due to its precious nature earlier work on gold were mainly focused on metallic state of gold and its extraction from earth crust and further purification. However, since last 30 years the chemistry of gold has thoroughly been explored focusing on the use of gold in advanced materials and catalysis.

1.1.2.2 Properties of Gold

Gold has a shiny lustre and high electrical and thermal conductivities. It is also one of the most malleable and ductile metals with just 1 gm being enough to be hammered into 1 m². However, gold is not a very hard metal as it can easily be scratched with a knife. The atomic number of gold is 79 with electronic configuration as [Xe]4f¹⁴5d¹⁰6s¹. Like metallic copper

and silver, metallic gold has face centred cubic FCC structure. Due to stronger interatomic bonding metallic gold exhibits melting and boiling points higher than those of silver. This is due to the fact that the atomic radius of gold is smaller than that of silver. The smaller radius of gold may be attributed to the strong relativistic effect. In the following we discuss how relativistic effects lead to some of the interesting properties of gold.

1.1.2.3 Relativistic Effect in Gold

The relativistic effects play important role for elements with high value of Z (atomic number) as the electron moving near the nucleus acquire speed comparable to speed of light. Consequently, the mass of the electron increases which leads to the contraction of the sizes of the orbitals. This contraction is observed mainly for the s and p orbitals. The contraction of these orbitals leads to a stronger screening of the nuclear attraction, and hence to a destabilization and expansion on the d and f orbitals. As a result of this, $5d$ orbital undergoes an expansion whereas, contraction is observed for $6s$ orbital thereby decreasing the energy gap between these two orbitals. Consequently, $6s$ and $5d$ orbitals are strongly hybridized which distinguishes gold from other coinage elements like Cu and Ag . Figure 1.1 shows that among all the elements

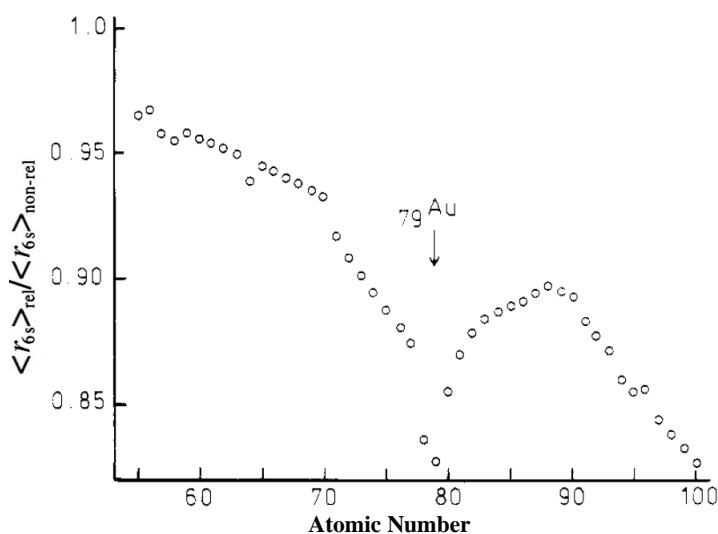
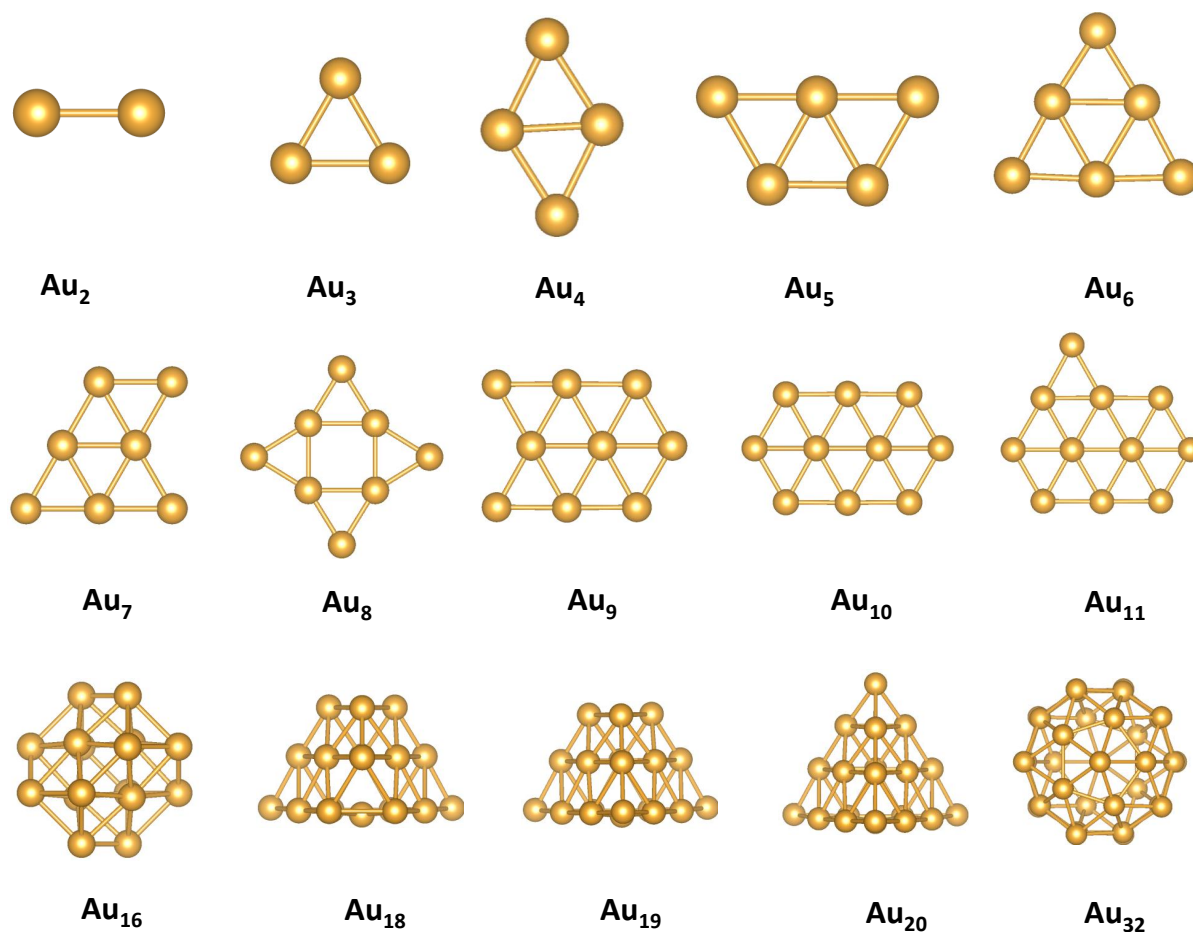


FIGURE 1.1: Relativistic contraction of the $6s$ orbital of the elements Cs to Fm . This is calculated from $\langle r_{6s} \rangle_{\text{relativistic}} / \langle r_{6s} \rangle_{\text{non-relativistic}}$ and shows a maximum contraction at gold (taken from Ref. [29]).

with $Z < 100$ the maximum relativistic effect is observed for gold [29, 30]. The yellow color of bulk gold is mainly due to the reduced gap (2.38 eV) between the 5d and 6s orbitals leading to the absorption of blue and violet light. On the other hand, for bulk silver corresponding transition does not occur until 3.70 eV. As a result of this it appears white in color. Therefore, the relativity driven hybridization of s and d orbitals leads to the stronger bonding between the gold atoms, which in turn significantly alters the structural and chemical properties of gold clusters and this is discussed in the next section.

1.1.2.4 Gold Clusters

Gold clusters can be produced by vaporizing the gold sheets/rods with the help of laser light [31, 32]. The generated clusters of various sizes are separated using mass spectrometer. These clusters are investigated either in the gas phase or by depositing them on some solid supports like MgO, Al₂O₃, TiO₂, CaO etc. [33–35]. Recently, gold clusters have also been chemically grown in suitable organic matrix [36–38]. Presently, the experimental techniques are capable of both producing and accurately characterising the gold clusters of various sizes ranging from very large number of atoms to the smallest two-atom dimer (Au₂). As discussed earlier, the effect of relativity renders a gold atom unique characteristics which make it a special element in the periodic table. The relativistic effect in conjunction with electron confinement endows gold clusters quite unique structural, chemical, optical and magnetic properties, which has attracted considerable attention of both theoreticians and experimentalists. For example, it is observed that in gold clusters (Au_n) 2-dimensional (2D) to 3-dimensional (3D) structural transition occurs for larger sizes ($n > 11$) as compared to the other two coinage metal (Ag and Cu) clusters because of relativistically enhanced strong sd hybridization and d-d interaction [39, 40]. This is elucidated in Figure 1.2 where we show optimized structures of gold clusters (Au_n) of various sizes. Note that the larger gold clusters like Au₂₀, Au₃₂ etc. possess highly symmetric tetrahedral or icosahedral structures. Like structural properties the relativistic effects also alter the chemical reactivity of gold clusters. In 1984 G. J. Hutchings [41] predicted the

FIGURE 1.2: Gold clusters (Au_n) in the size range $n = 2 - 32$.

catalytic activity of gold particles and concluded that it is the best one for acetylene hydrochlorination reaction on carbon support. Around the same time the catalytic activity of the tiny (2-4 nm) gold nano-particles supported on larger transition metal oxide (Fe_2O_3 , Co_3O_4 and NiO) particles was demonstrated by Harura *et. al*, [42]. After this pioneering work, a large number of theoretical and experimental studies have been carried out to understand the catalytic properties of these nanoparticles and nanoclusters in view of contrasting character of bulk gold [10, 43–47]. Recently, in an article published in Nature [48] it has been reported that the gold nano-particles can be used in the cars for air purification. It is observed that smaller gold clusters like Au_6 [32] are found to be very reactive, while the reactivity reaches the inert bulk limit for larger clusters like Au_{144} [49]. However, the catalytic activity of the larger gold clusters can be enhanced with help of doping using the alkali or transition metals atoms [15, 16, 50–53]. This has motivated us to investigate further the role of doping in the

performance of nano-sized gold cluster (Au_{20}) as an catalytic agent for CO oxidation reaction. In the present thesis we aim to address some of the issues related to the catalytic activity of 20-atom gold cluster.

In the family of gold clusters Au_{20} occupies a special position due to its symmetric tetrahedral structure, which is both energetically and chemically highly stable in nature. The Au_{20} cluster is a magic number cluster with a size of about a Fermi wavelength of an electron in bulk gold (0.7 nm). Both the neutral and ionic form of Au_{20} have been produced experimentally [46, 47] and found to be possessing tetrahedral geometry. Subsequently, a large number of theoretical and experimental studies have been carried out focusing attention on various aspects like geometric structure, catalytic activity, nonlinear optical property, and surface enhanced Raman scattering property of Au_{20} cluster [14, 44, 46, 54–56]. The tetrahedral geometry (as shown in Figure 1.3)

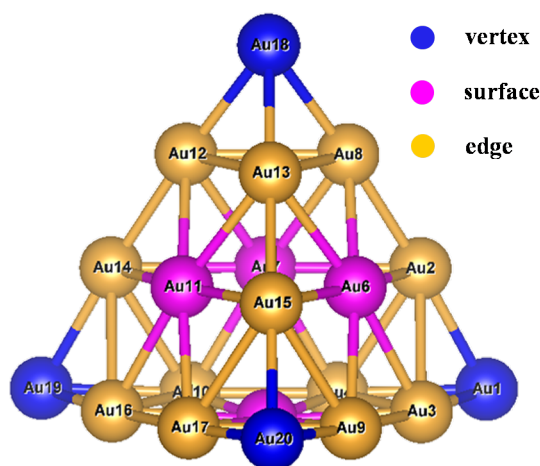


FIGURE 1.3: Optimized geometry of pure Au_{20} cluster.

of the Au_{20} cluster has three unique sets of atoms, namely surface (S) (4 Au atoms), edge (E) (12 Au atoms) and vertex (V) (4 Au atoms). The vertex Au atoms are the lowest coordinated sites with coordination number of 3, while the surface and edge Au atoms are having coordination number of 6. Due to different local environment, the electronic structure of the vertex, surface and edge Au atoms are also very different. The vertex Au atoms are found to be negatively charged whereas surface atoms are positively charged. This polarized charge distribution leads to large (1646 a.u.) first order hyperpolarizability (β) of Au_{20} cluster, which is four times higher than that of π -delocalized phenyliminomethyl ferrocene complex and about 150 times higher

than the average hyperpolarizability of urea [56]. Moreover, it is reported that the Raman or infra red signal of the organic molecules like pyridine gets enhanced when it is adsorbed on Au₂₀ cluster [44, 57]. However, it has been observed that the Au₂₀ cluster shows very weak chemical reactivity [58]. The chemical inertness of Au₂₀ cluster is characterized by a very large energy gap (1.777 eV) [47] between highest occupied molecular orbital (HOMO) and lowest unoccupied molecular orbital (LUMO), which is even greater than that of C₆₀ (1.57 eV) [59]. However, the negative ion of Au₂₀ shows higher reactivity towards the adsorption of CO and O₂ molecules [14]. It is also observed that the reactivity of the Au₂₀ cluster can be enhanced either by incorporating alkali metal atoms or by depositing it (Au₂₀) on some suitable supports [14, 60, 61]. Motivated by these results in the present thesis we propose to study the effect of different kind of metallic dopant atoms and support on the structural and electronic properties of gold clusters with the primary aim to explore the possibility of enhancement of its chemical reactivity. In the following we discuss the effect of support on the properties of gold clusters.

1.1.2.5 Supported Gold Clusters

For practical reason sometimes the clusters are deposited on suitable supports. It has already been reported that the structural and chemical properties of the gold cluster get modified when they are deposited on solid surfaces. The modification of these properties strongly depends upon the nature of the surface. Mostly oxide surfaces are used to support the gold clusters. In particular, MgO surface has been extensively explored for the deposition of gold clusters [60–66]. It is found that the pristine MgO surface does not affect the geometry and electronic structure of gold clusters, while the defect rich or doped MgO surface can change the geometry as well as the electronic structure of the gold clusters [17, 61, 65]. This change in geometry is attributed to charge transfer from the surface to the adsorbed clusters. Due to such charge transfer a dimensionality cross over of gold clusters can occur along with enhanced catalytic activity [61, 62, 65]. Other well studied oxide supports for gold clusters are Al₂O₃, TiO₂, CaO etc. [33–35]. Recently, non oxide two dimensional surfaces are also predicted to be promising as a support for the gold clusters. To this end gold clusters on pure and doped graphene surfaces

has been investigated by various groups [67, 68]. In the last two-three years graphene like two dimensional materials grown from other group IV elements have attracted the attention of the researchers [69, 70]. Very recently, silicene which is a single layer of Si atoms has been grown successfully by various groups [71–74]. However, the theoretical prediction of silicene was reported a decade ago [75]. Silicene shows similar properties like graphene as both have linear dispersion around the Dirac point. Due to this semi metallic band structure silicene has attracted considerable attention of the researchers. Recently, Akinwande and co-workers have demonstrated the use of silicene as field-effect transistor [76]. Note that the geometries of graphene and silicene are not exactly same [70]. In graphene all the C atoms lie on a same plane whereas, for silicene there are two type of Si atoms which lie on two different planes. For this reason silicene is known to have buckled structure in contrast to the planar structure of graphene. In Figure 1.4 we display the single sheets of graphene and silicene. The buckling of

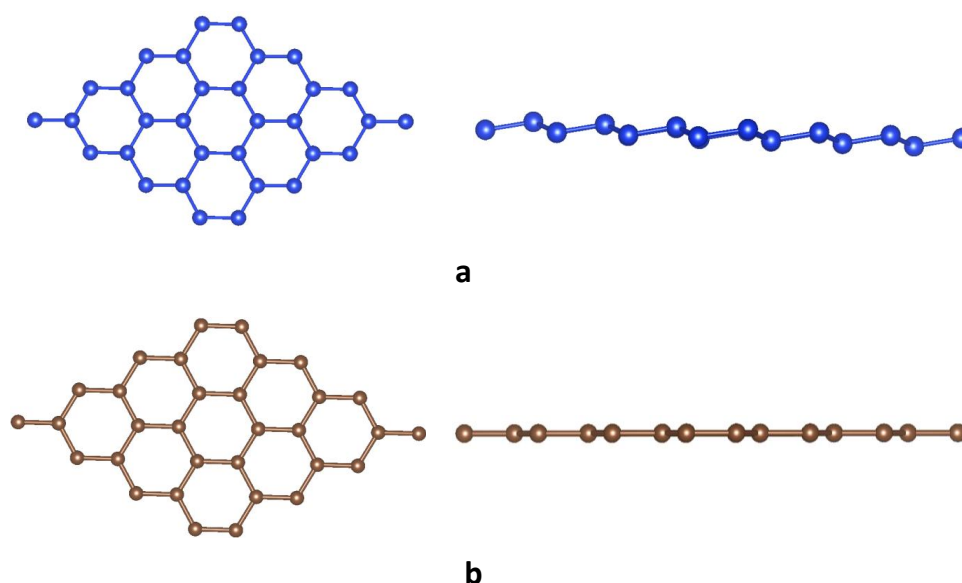


FIGURE 1.4: Single sheets of (a) silicene and (b) graphene.

silicene occurs due to the presence of sp^2 and sp^3 mixed hybridization in Si-Si bonds along the plane of the silicene. Moreover, the buckling leads to the strong σ and weak π bonds between the Si atoms. These weak π bonds can be broken easily to adsorb guest atoms or molecules on the silicene. Recently, it has been reported that a single atom of alkali, transition and coinage metals can be strongly adsorbed on silicene [77]. Furthermore, it is observed that the single gold

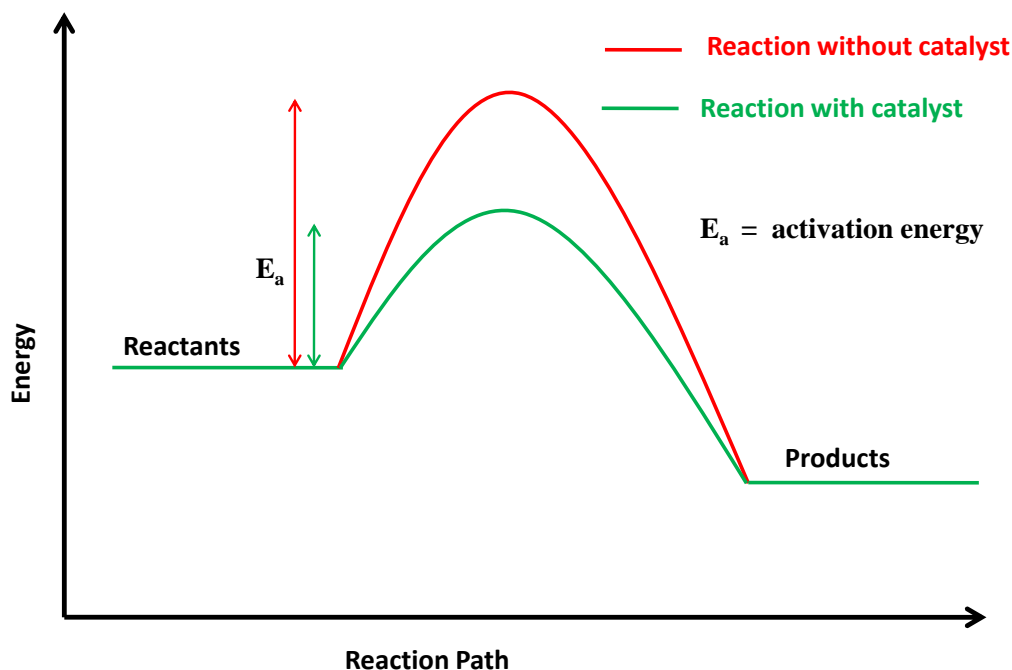


FIGURE 1.5: Role of a catalyst.

atom on silicene exhibits efficient catalytic activity for the oxidation reaction of CO molecule [78]. This has motivated us to study the adsorption of gold clusters on silicene. In the present thesis we have discussed the effect of silicene on the structural and electronic properties of the gold clusters.

1.1.2.6 Heterogeneous Catalysis

In view of our aim to investigate the catalytic activity of Pt doped gold clusters towards oxidation reaction of CO, we now briefly describe basic mechanisms of catalysis relevant for our purpose. *Catalysis* is defined as a process in which the rate of a reaction is enhanced by a relatively small amount of a different substance (known as catalyst) that does not undergo any permanent change itself. The catalyst helps to reduce the activation barrier of the chemical reaction and thereby increasing the reaction rate. Note that catalyst cannot facilitate the thermodynamically forbidden reactions. The cartoon picture in Figure 1.5 depicts the role of a catalyst as an agent which reduces the reaction barrier. Such catalytic activity of acid (catalyst)

in the conversion of starch to glucose in presence of water was first reported by the Russian scientist Gottlieb Kirchhof in 1812 [79]. Around the same time English chemist Sir Humphry Davy found that platinum can be used to accelerate certain organic reactions. Later, his student Michael Faraday demonstrated the ability of platinum to recombine hydrogen and oxygen to form water [79]. In 1834, Swedish chemist John Berzelius demonstrated that the sulphuric acid can accelerate the conversion of alcohol to ether and he named this decomposition process as 'catalysis'. Presently, catalysts are used in countless applications in our daily lives such as catalytic converters in motor vehicles and large scale applications in industries etc. Due to the high importance of catalytic materials, a large number of researchers from both academia and industries are actively working in this field.

Broadly the catalysis is categorized into two types namely, homogeneous catalysis and heterogeneous catalysis. For homogeneous catalysis the reactants and the catalyst are in the same phase while they are in different phases for heterogeneous catalysis. The catalysts in heterogeneous catalysis are, in general, solid materials and the reactants are either liquid or gas or both. In this type of catalytic process the surface area of the catalyst plays a very important role as the reaction takes place only on the surface of the solid material. The reaction rate is proportional to the surface area of the catalyst. In heterogeneous catalysis the important factors are the reactivity of the catalyst, the diffusion of the reactants and products on the surface and most importantly the desorption of the products. The stability of the heterogeneous catalyst is also very crucial. Since in heterogeneous catalysis the reactants and catalyst are in different phases, the catalyst can be easily separated from the products and reactants. As a result, constant flow of reactants can be maintained in heterogeneous catalysis.

The heterogeneous catalysis can be described by two basic mechanisms namely, Langmuir-Hinshelwood (LH) and Eley-Rideal (ER) [54]. In LH mechanism the reaction occurs between the species which are adsorbed on the surface of the catalyst (see Figure 1.6a). Whereas, for ER type reaction the molecule in the gas phase reacts with another molecule adsorbed on the surface of the catalyst (see Figure 1.6b). For this reason the knowledge of the adsorption behavior of the reactants on the catalyst surface is very crucial. Note that for the maximum reaction rate there

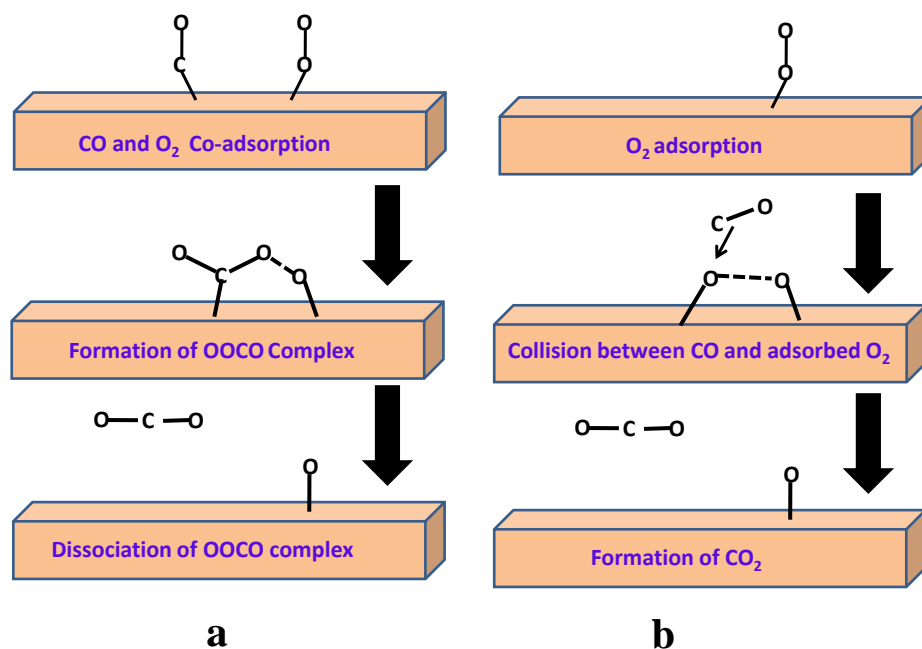


FIGURE 1.6: Cartoon picture for (a) LH mechanism, and (b) ER mechanism for oxidation reaction of CO molecule.

exists an optimum value of the adsorption energy of the reactants which is known as Sabatier principle [80]. According to this principle the plot between the reaction rate and adsorption energy of the reactants follows a *volcano* like shape. The peak of this volcano indicates the optimum value of the adsorption energy of the reactants.

1.2 Theoretical Methodology

In this section we give a brief description of the theoretical methodology employed for carrying out the calculations of the structural and chemical properties of the gold nano-clusters which is the main topic of this thesis. To this end we employ *ab-initio* methods within the formalism of DFT which is briefly described below.

1.2.1 Many-Body Problems

It is well known that the physical and chemical properties of materials are determined by the behavior of electrons which glue the atoms together to form a variety of molecules and solids. To understand the behavior of these electrons which are quantum particles in nature one has to solve the central equation of quantum mechanics, the time-independent Schrödinger equation

$$\hat{H}|\Psi\rangle = E|\Psi\rangle \quad (1.1)$$

where $|\Psi\rangle$ is the energy eigenfunction of the system, E indicates the energy eigenvalue and \hat{H} represents the Hamiltonian of the system, which is given by,

$$\begin{aligned} \hat{H} = & -\frac{\hbar^2}{2m_e} \sum_{i=1}^N \nabla_i^2 - \frac{\hbar^2}{2} \sum_{I=1}^{N_I} \frac{\nabla_I^2}{M_I} + \frac{1}{4\pi\epsilon_0} \sum_{i<j}^N \frac{e^2}{|\mathbf{r}_i - \mathbf{r}_j|} + \frac{1}{4\pi\epsilon_0} \sum_{I<J}^{N_I} \frac{Z_I Z_J e^2}{|\mathbf{R}_I - \mathbf{R}_J|} \\ & - \frac{1}{4\pi\epsilon_0} \sum_{i,I}^{N,N_I} \frac{Z_I e^2}{|\mathbf{r}_i - \mathbf{R}_I|} \end{aligned} \quad (1.2)$$

where,

lower and upper cases are used to represent the electrons and nuclei, respectively.

\hbar and ϵ_0 : Planck's constant and permittivity of vacuum.

\mathbf{r}_i and \mathbf{R}_I : positions of electrons and nuclei.

m_e and M_I : masses of electrons and nuclei.

e and $Z_I e$: charges of electrons and nuclei.

N and N_I : numbers of electrons and nuclei in the system.

In this thesis, we use atomic units (a.u.) in which \hbar , e , m_e , and $\frac{1}{4\pi\epsilon_0}$ are taken as unity. In Eq. 1.2, the first and second terms represent the kinetic energy operators respectively for electrons and nuclei. The third and fourth terms correspond to the repulsive potentials due to electron-electron and nucleus-nucleus interactions, respectively. The attractive interaction between the electrons and nuclei is described by the last term. It is very clear that the complexity of the eigen value

equation (Eq. 1.1) increases with the increasing number of electrons (N) and nuclei (N_I). This is because the Hamiltonian and the corresponding many wave function Ψ depend on $3(N + N_I)$ coupled degrees of freedom. Hence, to solve the Eq. 1.1 for any realistic system (where both N and N_I are large) one has to look for reasonable approximation to simplify this complex Hamiltonian. Fortunately, in many physical problems, the kinetics of the nuclei is not important and thereby they can be neglected. This is the basic essence of the *Born-Oppenhemier* approximation [81]. Under this approximation we can decouple the nuclear and electronic degrees of freedom and focus attention on the time-independent Schrödinger equation for the electrons only.

1.2.2 Born-Oppenhemier Approximation

In a system the electrons move much faster than the nuclei since the mass of an electron is much smaller than that of a nucleus. Thus to a good approximation relative to the electrons, nuclei can be considered as stationary while electrons carry out their motions. This fact allows one to assume that the nuclei remain always in the same adiabatic state during the motion of electrons thereby decoupling the electronic and nuclei degrees of freedom. By using this approximation, one can neglect the kinetic energy of nuclei from the Hamiltonian. Furthermore, the positions (R_I) of the nuclei can be treated as parameters and thus the nucleus-nucleus interaction term becomes constant for a fixed set of nuclei. Thus, applying the *Born-Oppenhemier* approximation we can rewrite the Hamiltonian only for electrons as,

$$\hat{H} = -\frac{1}{2} \sum_{i=1}^N \nabla_i^2 + \sum_{i<j}^N \frac{1}{|\mathbf{r}_i - \mathbf{r}_j|} - \sum_{i,I}^{N,N_I} \frac{Z_I}{|\mathbf{r}_i - \mathbf{R}_I|} \quad (1.3)$$

In the above Hamiltonian still the electronic degrees of freedom are coupled by the second electron-electron interaction term. For this reason even sloving the eigenvale equation given by (Eq. 1.1) with the above hamiltonian is still a very difficult task. However, there are various approximate methods, which take into account the effect of electron-electron interaction with different degree of accuracy, have been developed to solve the complicated many-body

Schrödinger equation (Eq. 1.1). The Hamiltonian in Eq. 1.3 may be written more compactly as,

$$\hat{H} = \hat{T} + \hat{V}_{ne} + \hat{W} \quad (1.4)$$

where

$$\hat{T} = -\frac{1}{2} \sum_{i=1}^N \nabla_i^2 \quad (1.5)$$

is the kinetic energy operator, and

$$\hat{V}_{ne} = - \sum_{i,I}^{N,N_I} \frac{Z_I}{|\mathbf{r}_i - \mathbf{R}_I|} \quad (1.6)$$

represents the electron-nucleus interaction term and

$$\hat{W} = \sum_{i < j}^N \frac{1}{|\mathbf{r}_i - \mathbf{r}_j|} \quad (1.7)$$

is the electron-electron interaction operator. As noted above for many-electron system it is not possible to obtain exact solution for time-independent Schrödinger equation as electron-electron interaction makes the many-body wavefunction very cumbersome. To circumvent this difficulty various approximate methods like Hartree-Fock [82] and post-Hartree-Fock methods have been developed to solve the time-independent Schrödinger equation. The post-Hartree-Fock methods like (i) Configuration interaction (CI), (ii) Coupled cluster (CC) and (iii) Møller-Plesset perturbation theory (MP2, MP3, MP4, etc.) are able to produce quite accurate results which match well with the experimental data. However, these methods are computationally very expensive due to an unfavorable scaling with the size of the systems [83] and hence their applicability are restricted to the smaller systems of few atoms or molecules. For example, in CI method the computation time scales as M^6 for single and double excitations and as M^8 and M^{10} for triply and quadruple excitations, respectively, where M is the size of the basis set used in the calculations. Similarly, the computational time in n^{th} order Møller-Plesset perturbation

theory scales as M^{n+3} . It is then natural to look for an alternative method which can be used to calculate the electronic properties of a wider range of systems having large number of atoms or molecules and yet takes into account of the effect of electron-electron interaction namely, exchange and correlation quite accurately. An alternative to the wavefunctional approach to the many-electron problems is DFT in which ground state electron density is the basic variable which is a function of just three spatial variables. The theory is in principle exact and allows one to write any physical observable of a many-electron system in terms of its ground state density. This theory has been extensively used for calculations of electronic structure of many-electron systems. In the following we give a brief description of Kohn-Sham formalism (KS) [84] of DFT which is generally employed to carry out *ab-initio* electronic structure calculations of many-electron systems .

1.2.3 Density Functional Theory

The foundation of DFT was laid by Hohenberg and Kohn (HK) [85] in terms of two fundamental theorems which endow the ground state density $n(\mathbf{r})$ (a function of three spatial variables) a status of basic variable like the wavefunction $\Psi(\mathbf{r}_1, \mathbf{r}_2, \dots, \mathbf{r}_N)$ (a function of $3N$ spatial variables) in Schrödinger theory.

The first HK theorem states that the ground state electronic density ($n(\mathbf{r})$) of a system of an arbitrary collection of fixed number of electrons moving under the influence of local external one-body potential $V_{ext}(\mathbf{r})$ is uniquely determined by $V_{ext}(\mathbf{r})$. This implies that the Hamiltonian is a unique functional of the density, $n(\mathbf{r})$ and hence by solving the time-independent Schrödinger equation the wavefunction can be determined uniquely by the density, $n(\mathbf{r})$, so that

$$n(\mathbf{r}) \longleftrightarrow \Psi[n(\mathbf{r})] \quad (1.8)$$

This further implies that the ground state-expectation value of any observable \hat{O} is also a functional of the density, $n(\mathbf{r})$, i.e.

$$\langle \Psi[n] | \hat{O} | \Psi[n] \rangle = O[n] \quad (1.9)$$

In particular the ground state energy E_{gs} of the many-electron system can be written as

$$E_{gs} = T[n] + W[n] + V_{ne}[n] \quad (1.10)$$

$$= \int n(\mathbf{r}) V_{ext}(\mathbf{r}) d(\mathbf{r}) + F_{HK}[n] \quad (1.11)$$

with

$$T[n] = \langle \Psi[n] | \hat{T} | \Psi[n] \rangle \quad (1.12)$$

$$W[n] = \langle \Psi[n] | \hat{W} | \Psi[n] \rangle \quad (1.13)$$

$$V_{ne}[n] = \langle \Psi[n] | \hat{V}_{ne} | \Psi[n] \rangle \quad (1.14)$$

The functional $F_{HK}[n] = T[n] + W[n]$ is called Hohenberg–Kohn energy functional which is a universal functional of the ground state density in the sense that it does not depend on the external potential $V_{ext}(\mathbf{r})$. The second HK theorem allows one to determine ground state density via energy variational principle and it states that for any trial density $n'(\mathbf{r})$, such that $n'(\mathbf{r}) > 0$ and $\int n'(\mathbf{r}) d\mathbf{r} = N$ the exact ground state energy obeys the following relation

$$E_0 \leq E_{gs}[n'] \quad (1.15)$$

where $E_{gs}[n']$ is the energy functional which can be calculated from Eq. 1.11 for density $n'(\mathbf{r})$. This is analogous to the variational principle for the ground state wavefunction. Note that in deriving this variational principle, the external potential is not considered to be a functional of density but rather a parameter. The ground state density is the one which makes the energy functional $E_{gs}[n]$ stationary under the constraint $\int n(\mathbf{r}) d\mathbf{r} = N$ and satisfy the following

relation,

$$\delta E_{gs}[n] - \mu \left(\int n(\mathbf{r}) d\mathbf{r} - N \right) = 0 \quad (1.16)$$

where μ is the Lagrange multiplier. This in turn gives the Euler-Lagrange equation

$$\mu = \frac{\delta E_{gs}[n]}{\delta n} \quad (1.17)$$

$$= V_{ext}(\mathbf{r}) + \frac{\delta F_{HK}}{\delta n} \quad (1.18)$$

Although the variational equation is easy from the computational point of view, however, it can be solved only approximately as the exact form of $F_{HK}[n]$ as a functional of ground state density is not known. Moreover, the approximate results are not accurate enough mainly due to the highly approximate treatment of the kinetic energy which constitutes a substantial part of the total energy. To circumvent this problem Kohn and Sham (KS) proposed a formalism [84] in which a major portion of the kinetic energy is taken into account exactly. In this formalism, the problem of a complicated interacting system is ingeniously mapped onto a problem of much easier-to-solve non-interacting system. The external potential of the interacting system is replaced by a suitable effective external potential V_{ks} of a non-interacting system having the same density as that of the actual interacting system. This effective external potential V_{ks} takes care of the interactions present in the system. The universal functional F_{HK} can be written in terms of the kinetic energy $T_s[n]$ of the fictitious auxiliary non-interacting system as,

$$\begin{aligned} F_{HK}[n] &= T[n] + W[n] \\ &= T_s[n] + (T[n] - T_s[n]) + E_H[n] + (W[n] - E_H[n]) \\ &= T_s[n] + E_H[n] + E_{xc}[n] \end{aligned} \quad (1.19)$$

where E_{xc} is the so-called exchange-correlation (XC) functional given by

$$E_{xc}[n(\mathbf{r})] = (W[n] - E_H[n]) + (T[n] - T_s[n]) \quad (1.20)$$

and $E_H[n]$ represents the Hartree energy due to the classical Coulomb interaction between the electrons.

It can be observed from the above equation that the XC functional E_{xc} consists of two terms, first one coming from the difference between the total electron-electron interaction and the classical Hartree term and second one is the difference between the kinetic energies of the interacting and non-interacting systems. Therefore, it is very clear that the origin of the quantity $E_{xc}[n]$ is purely quantum mechanical and the exact form of this functional is not known. The non-interacting kinetic energy $T_s[n]$ is given in terms of the single-particle orbitals, $\phi_i(\mathbf{r})$ as,

$$T_s[n] = - \sum_i^N \int \phi_i(\mathbf{r})^* \left[\frac{\nabla^2}{2} \right] \phi_i(\mathbf{r}) d\mathbf{r} \quad (1.21)$$

By using the variational nature of the ground state energy and Eqs. (1.19) - (1.21) one obtains Hartree-like equation satisfied by the single-particle orbitals $\phi_i(\mathbf{r})$ as

$$\left(-\frac{\nabla^2}{2} + V_{ks}[n(\mathbf{r})] \right) \phi_i(\mathbf{r}) = \epsilon_i \phi_i(\mathbf{r}) \quad (1.22)$$

where the effective potential V_{ks} is defined by,

$$V_{ks}[n(\mathbf{r})] = V_{ext}[n(\mathbf{r})] + V_H[n(\mathbf{r})] + V_{xc}[n(\mathbf{r})] \quad (1.23)$$

$$\text{with} \quad V_H[n(\mathbf{r})] = \frac{1}{2} \int \frac{n(\mathbf{r}')}{|\mathbf{r} - \mathbf{r}'|} d\mathbf{r}' \quad \text{and} \quad V_{xc}[n(\mathbf{r})] = \frac{\delta E_{xc}[n(\mathbf{r})]}{\delta n(\mathbf{r})} \quad (1.24)$$

are the Hartree and the XC potentials respectively. The density of the interacting system can be obtained from the single-particle orbitals via,

$$n(\mathbf{r}) = \sum_i^N |\phi_i(\mathbf{r})|^2 \quad (1.25)$$

The Hartree-like single-particle equation (Eq. 1.22) is the so-called Kohn-Sham equation of

DFT. In Kohn-Sham approach the kinetic energy for non interacting electrons is exactly incorporated while the exact form of the XC ($E_{xc}[n(\mathbf{r})]$) is still not known. Therefore, to solve the Kohn-Sham equation it become necessary to choose an approximate form for $E_{xc}[n(\mathbf{r})]$ ($V_{xc}[n(\mathbf{r})]$) in terms of the ground state density. During the last fifty years several research group have devoted considerable effort to develop the approximate forms for the exchange and energy functional with higher and higher degree of accuracy [84, 86–93].

The simplest form of $E_{xc}[n(\mathbf{r})]$ was proposed by Kohn and Sham within the so called Local Density Approximation (LDA). The main assumption of LDA is that $E_{xc}[n(\mathbf{r})]$ for a non-uniform electronic system can be obtained by applying the results of uniform electron gas to infinitesimal portions of non-uniform electron distribution, each having $n(\mathbf{r})d(\mathbf{r})$ number of electrons, and then summing over the contributions of XC energy $\epsilon_{xc}[n(\mathbf{r})] d\mathbf{r}$ of each element over all space. This then leads to

$$E_{xc}^{LDA}[n(\mathbf{r})] = \int n(\mathbf{r}) \epsilon_{xc}(n) d\mathbf{r} \quad (1.26)$$

where $\epsilon_{xc}(n)$ indicates the XC energy per particle of a uniform electron gas of density $n(\mathbf{r})$. With this the XC potential becomes,

$$V_{xc}^{LDA}[n(\mathbf{r})] = \frac{\delta E_{xc}[n(\mathbf{r})]}{\delta n(\mathbf{r})} = \epsilon_{xc}(n(\mathbf{r})) + n(\mathbf{r}) \frac{\delta \epsilon_{xc}[n(\mathbf{r})]}{\delta n(\mathbf{r})} \quad (1.27)$$

The XC density $\epsilon_{xc}(n)$ can be further decomposed into exchange and correlation parts as

$$\epsilon_{xc}(n) = \epsilon_x(n) + \epsilon_c(n) \quad (1.28)$$

For uniform electron gas the exact form of the exchange part, ϵ_x was derived by Dirac [94]. Whereas, exact form of the correlation term, $\epsilon_c(n)$ is not known as the determination of the correlation energy of uniform electron gas is a difficult many-body problem on its own. However, for finite number of electrons Ceperley and Alder calculated the ground state energy of

a uniform electron gas accurately by employing quantum Monte Carlo simulation. The extracted correlation energies from this result are then interpolated using sophisticated interpolation schemes to provide various analytical forms of correlation density. The most widely used forms are VWN, developed by Vosko, Wilk and Nusair [86] and PW92 which is developed by Perdew and Wang [87].

For many years LDA has been applied to calculate band structures and total energies quite accurately in solid state physics. However, it is not that popular among the quantum chemists as it fails to provide a quantitative description of chemical bond in molecules which requires calculations with an error not more than 1 kcal/mol (0.04 eV per particle). To achieve this accuracy and at the same time keeping in mind the inhomogeneity in density of real many-electron system, improved expressions of XC functional have been proposed within Generalized Gradient Approximation (GGA). The general form for the XC functional within GGA is given by

$$E_{xc}^{GGA}[n(\mathbf{r})] = \int \epsilon_{xc}^{GGA}(n(\mathbf{r}), \nabla n(\mathbf{r})) d\mathbf{r} \quad (1.29)$$

where ϵ_{xc}^{GGA} is the XC energy density which is determined by imposing as many of the known exact properties of $\epsilon_{xc}[n]$. By following this scheme several XC functional within GGA have been developed and presently there exists a whole zoo of GGA functional. The details on GGA can be found in several reviews [95–97]. The most popular functional within GGA which are being extensively employed to carry out calculations of molecules and solids were proposed by Perdew and co-workers, such as PW91 (Perdew-Wang 1991) [98] and PBE (Perdew-Burke-Ernzerhof) [92]. In this thesis, for most of our calculations we use these two GGA functionals.

1.2.4 Nudged Elastic Band (NEB)

As mentioned before one of the main focus of this thesis is on the catalytic activity of doped gold clusters towards oxidation reaction of CO molecule. For this purpose it is necessary to determine the minimum energy path (MEP) along which the oxidation reaction will proceed

and the corresponding transition state. Using the transition state energy we estimate the reaction barriers which provides quantitative information regarding the feasibility of the reaction. To determine the MEP we use nudged elastic band method (NEB) [99]. This method can be applied to reactions for which both initial and final states are known. To determine MEP first several images (typically 4-20) of the systems between the initial and final states are constructed. A spring type interaction between the images is considered to maintain the continuity of the path which mimics an elastic band. To bring the band close to MEP an optimization of the elastic band involving the minimization of the force acting on the images is carried out. The NEB method gives a discrete representation of the MEP where the energy of the saddle point which is known to be the transition state is obtained by interpolation. If the barrier is narrower compared to the length of the MEP then few images are found around the saddle point which may lead to the inaccurate interpolation to get the energy of the saddle point. This is circumvented by arranging the images with the help of a climbing image method and the resulting elastic band method is termed as Climbing Images NEB (CI-NEB) [100]. Unlike NEB method, in CI-NEB method the images are not dispersed uniformly rather, images are arranged in such a way so that the density of the image is more around the saddle point. This method provides more accurate energy of the transition state. In this thesis we use CI-NEB method to find the transition states and the reaction barriers to study the catalytic activity of the doped gold clusters in the oxidation reaction of CO molecule.

Chapter 2

Structural and Electronic Properties of Li Doped Gold Nano-Clusters

The doping of gold clusters with suitable metallic impurity allows one to tune the geometric, electronic, and chemical properties of these clusters in desirable fashion [101–104]. For example, gold-alkali bimetallic clusters show extra stability as compared to the pure gold clusters due to the charge transfer from the dopant alkali atom to the gold atoms [50, 105]. The charge transfer from alkali-metal atom to the gold atoms can be exploited to get very large first-order nonlinear optical coefficient by placing the dopant atom at appropriate locations in the cluster [106]. It has also been shown that doping can enhance the HOMO-LUMO energy gap thereby increasing the chemical stability of the cluster. For example, Gao et al. predicted that the HOMO-LUMO gap of a transition metal doped gold cluster (Zr@Au_{14}) may be enhanced significantly (2.23 eV) over that of Au_{20} cluster [107]. Recently, our group has carried out a detailed investigation of the various properties of doped neutral Au_{19}M ($\text{M} = \text{Li, Na, K, Rb, Cs, Cu, and Ag}$) clusters [19]. Our study reveals that the tetrahedral structure of Au_{20} is quite stable and it does not get much distorted when an Au atom is replaced by a Li or a Cu atom. It is interesting to note here that Au_{19}M clusters with dopant atom (Li or Cu) located at the center of one of the surfaces of tetrahedral structure are found to be energetically more stable than the pure Au_{20} cluster. However, the HOMO-LUMO gap and ionization potential (IP) of Au_{19}Li and

Au_{19}Cu are still lower than the corresponding values of pure Au_{20} cluster. A very recent study by Zhang and Fa [108] devoted to the anions of double doped bimetallic clusters $\text{Au}_{18}\text{M}_2^-$ ($\text{M} = \text{Cu}$ and Na) shows that even for double doped $\text{Au}_{18}\text{Cu}_2^-$ cluster tetrahedral structure of Au_{20} with two Cu atoms located at center of the surfaces remains the most stable structure. However, HOMO-LUMO gap of the double doped $\text{Au}_{18}\text{Cu}_2^-$ cluster is found to be smaller than that of single Cu atom doped cluster. Unlike Cu the double Na doped $\text{Au}_{18}\text{Na}_2^-$ cluster cannot retain the tetrahedral geometry of the pure Au_{20} , instead $\text{Au}_{18}\text{Na}_2^-$ possesses flat cage-like geometry which is because of the larger size of the dopant Na atom. In our earlier investigation we found that the binding energy of Au_{19}Li cluster is higher than the binding energy of other alkali atom ($\text{M} = \text{Na}, \text{K}, \text{Rb}$ and Cs) and coinage metal atom ($\text{M} = \text{Cu}$ and Ag) doped Au_{19}M clusters as well as that of pure Au_{20} cluster. These results then naturally motivated us to ask the question how the structure and stability of the doped bimetallic clusters are modified when two or more atoms with less electronegativity than Au atom are doped in Au_{20} cluster. The difference in the electronegativity between Li and Au is more than that of between Cu and Au, hence it is expected that charge transfer in Li doped cluster will be more as compared to the Cu doped one. Therefore, it would be interesting to investigate whether charge transfer can significantly alter the electronic properties of the doped Au_{20} cluster. The present chapter is devoted to a systematic investigation of the structure and various electronic properties of doped $\text{Au}_{20-n}\text{Li}_n$ ($n = 1 - 4$) clusters.

2.1 Computational Details

Our theoretical calculations are based on density functional theory as implemented in Amsterdam Density Functional (ADF2008) program package [109]. The relativistic effect due to Au atom is included in our calculations through zero-order regular approximation (ZORA) [110, 111]. All the doped structures are optimized using Perdew - Wang 1991 (PW91) XC functional [98] within GGA. For Au atom, we use the triple- ζ Slater type orbital (STO) basis

set added with two polarization functions (TZ2P in ADF basis library) at the frozen core approximation level. In particular, we consider electrons in the levels up to 4f as core. On the other hand, for Li atom all electrons are taken into consideration using TZ2P basis set. The geometries are optimized using quasi-Newton method and the Hessian is updated in the optimization process by employing Broyden-Fletcher-Goldfarb-Shanno (BFGS) [112–115] method until the convergence criteria of 10^{-4} a.u. for Cartesian gradient and 10^{-6} a.u. for energy are met. The stability of the clusters are checked with the vibrational frequency data. Absence of imaginary value of vibrational frequency indicates a stable structure. All the figures presented in this chapter are generated using the software XCrySDen [116].

The infrared (IR) absorption intensity A_i for the i^{th} vibrational mode can be calculated taking the derivatives of the electric dipole moment μ_{el} with respect to the normal coordinates Q_i as [117–120]

$$A_i = 947.86g_i \left| \frac{\partial \mu_{el}}{\partial Q_i} \right|^2 \quad (2.1)$$

where A_i is given in unit of km/mol and g_i is the degeneracy of the i^{th} mode of vibration. We analyze the vibrational spectra, identify the peaks and correlate them with the important vibrational modes of the clusters.

2.2 Properties of $\text{Au}_{20-n}\text{Li}_n$, $n = 1$ Clusters

In this section we discuss the geometric and electronic properties of the $\text{Au}_{20-n}\text{Li}_n$, $n = 1$ clusters (i.e., Au_{19}Li clusters). Note that the details of the geometric and electronic properties of the Au_{19}Li clusters are given in Ref. [19]. However, for the sake of completeness of the present thesis we briefly describe the properties of the Au_{19}Li clusters. To generate the initial geometries of Au_{19}Li clusters we consider several structures of pure Au_{20} and Au_{19} clusters (tetrahedral, tube- and cage-like), and create from them starting geometries of Au_{19}Li clusters either by replacing an Au atom with a Li atom in Au_{20} cluster or by adding a Li atom in Au_{19} cluster. As mentioned earlier (Figure 1.3), the tetrahedral Au_{20} cluster has three unique sets of

atoms, namely surface (S) (4 Au atoms), edge (E) (12 Au atoms) and vertex (V) (4 Au atoms). To generate exohedrally doped tetrahedral structure we replace one of the gold atom from these three sets by a Li atom. We denote these exohedrally doped tetrahedral Au_{19}Li clusters by Td-X, where Td stands for tetrahedral geometry and X (X = S, E, and V) refers to the location of the dopant atom Li and X = 0 represents a pure Au_{20} cluster. All these structures of Au_{19}Li cluster are then optimized at GGA level (PW91 XC functional). After geometry optimization we also calculate the vibrational frequencies to check the stability of these structures. The absence of

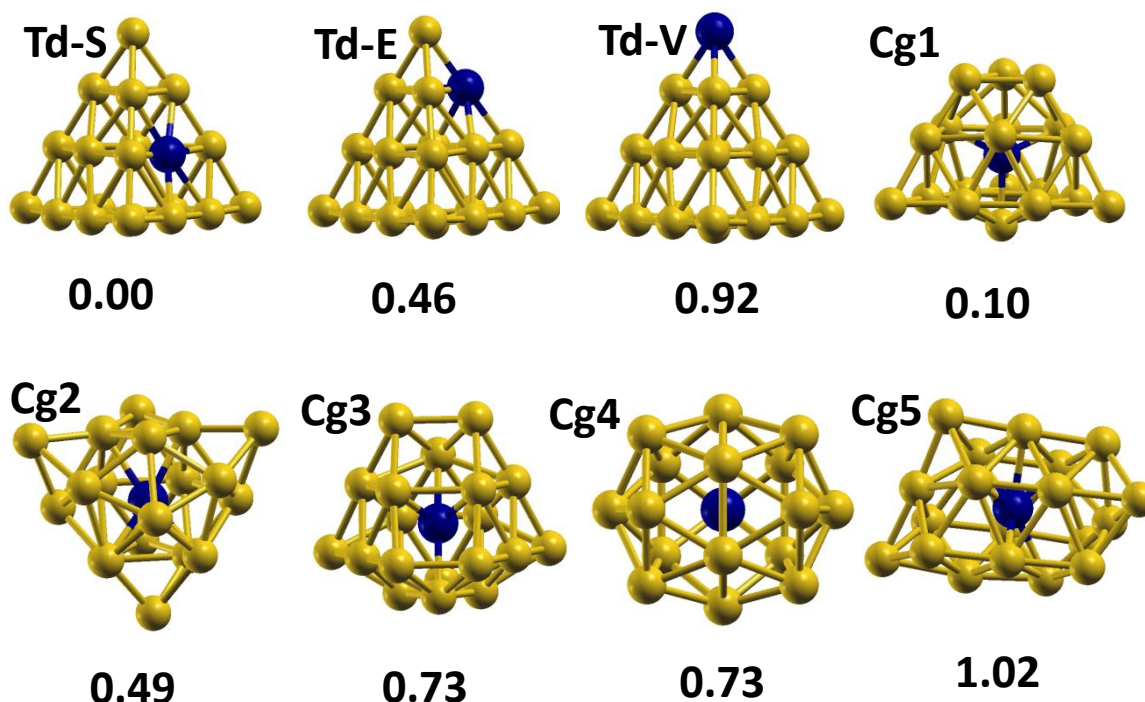


FIGURE 2.1: Optimized geometries of tetrahedral and cage-like Au_{19}Li clusters.

negative frequency component confirms the stability of the clusters. The optimized geometries of the three tetrahedral geometries (Td-S, Td-E and Td-V) of the Au_{19}Li clusters are displayed in Figure 2.1. To make our search for the minimum energy structure of the Au_{19}Li cluster more extensive we also consider more than ten cage-like isomers of Au_{19}Li cluster where the dopant Li atom is placed at the endohedral positions of the cage. The cage-like isomers are denoted by Cgi, where $i = 1 - 10$. All these cage-like isomers of Au_{19}Pt cluster are optimized at the similar level of theory as employed for obtaining optimized tetrahedral isomers. Selected optimized geometries of the cage-like isomers of Au_{19}Li cluster are shown in Figure 2.1.

It is observed that among all the isomers of Au_{19}Li cluster Td-S, where Li atom sits on the surface position of the tetrahedron of Au_{20} cluster is the most stable one while, Td-V where Li atom sits on the vertex site is the least stable configuration as compared to the other tetrahedral isomers of Au_{19}Li cluster. The binding energy of Td-S cluster is around 0.6 eV higher than that of the pure Au_{20} cluster. It is also reported that the doping of Li-atom insignificantly disturb the tetrahedral geometry of the pure Au_{20} cluster. This is due to the fact that the size of Li atom (1.52 Å) is comparable to that of Au atom (1.44 Å) [19, 50]. Moreover, it is found that the HOMO-LUMO gap of the Td-S cluster is around 0.1 eV lower than that of the pure Au_{20} cluster. The higher stability and lower HOMO-LUMO gap are the signatures of the efficient catalyst. Hence, it is natural to ask the question whether the doping of more than one Li atom can further enhance the stability of the 20-atom gold cluster with a lower HOMO-LUMO gap. To answer this question, we have carried a systematic investigation on the structural and electronic properties of the $\text{Au}_{20-n}\text{Li}_n$, $n = 2 - 4$ clusters and in the following we discuss the results.

2.3 Properties of $\text{Au}_{20-n}\text{Li}_n$, $n = 2$ Clusters

2.3.1 Structural Properties of Tetrahedral Clusters

Having discussed the geometries of Au_{19}Li clusters we now investigate the geometries of the $\text{Au}_{18}\text{Li}_2$ clusters. For this purpose we consider several structures of Au_{20} cluster (both tetrahedral and cage-like structures), and generate from them starting geometries of $\text{Au}_{18}\text{Li}_2$ clusters by replacing two Au atoms with Li atoms. We also consider initial structures of $\text{Au}_{18}\text{Li}_2$ clusters which are generated from the truncated structures of Au_{19} cluster by adding one Li atom in it and by replacing one Au atom with one Li atom. We explore more than 40 different $\text{Au}_{18}\text{Li}_2$ structures to carry out our investigations. All these structures of doped clusters are then optimized. Note that for the doped clusters considered here we find that spin singlet corresponds to the minimum energy configuration. Consequently, we consider only spin singlet as the ground state for all the doped clusters. After geometry optimization we also calculate the vibrational

frequencies to check the stability of these structures. Using these stable geometries we calculate the binding energy (BE), HOMO-LUMO gap (Δ_{HL}), ionization potential (IP) and electron affinity (EA) to characterize the stability and chemical inertness of the $\text{Au}_{18}\text{Li}_2$ clusters.

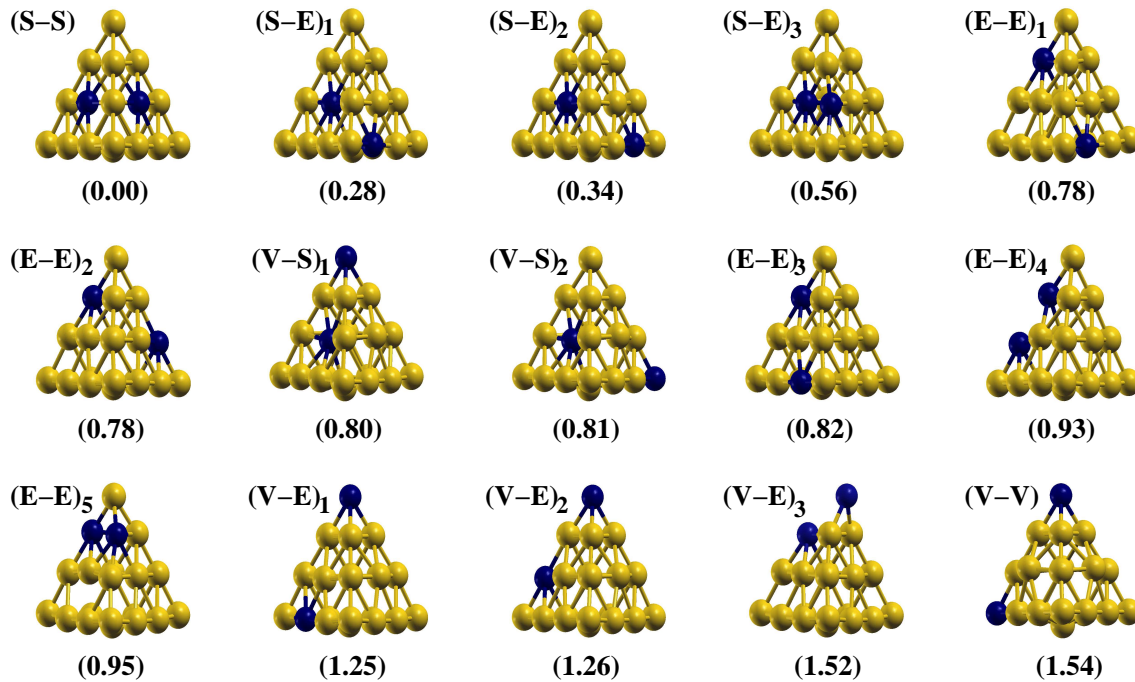


FIGURE 2.2: Optimized geometries of pyramidal doped $\text{Au}_{18}\text{Li}_2$ clusters in decreasing order of BE. The values within the parenthesis indicate the relative BE (in eV) with respect to the most stable structure Td(S-S) which has been denoted in the figure as (S-S). The symbol (X-Y) $_m$ indicates the cluster Td(X-Y) $_m$, where X and Y represent the locations of the dopant atoms at S (surface), V (vertex), and E (edge) and m is an integer which indicates the serial number of different X-X, Y-Y and X-Y combinations.

The optimized structures of $\text{Au}_{18}\text{Li}_2$ clusters based on the tetrahedral structure of Au_{20} are shown in Figure 2.2. We denote these doped clusters by Td(X-Y) $_m$, where X and Y represent the locations of the dopant atoms at S (surface), V (vertex), and E (edge) and m is an integer which indicates the serial number of different X-X, Y-Y and X-Y combinations. The structures in Figure 2.2 are arranged in the descending order of their stability. We note here that for geometry optimization 15 pyramidal $\text{Au}_{18}\text{Li}_2$ structures are chosen. It has been observed that the parent structure of Au_{20} does not undergo any significant distortion when two Au atoms are replaced by two Li atoms, as the atomic radius of Li (1.52 Å) is comparable to that of Au (1.44 Å) atom [19, 50].

2.3.1.1 Analysis of Deformation

In conformity with the above observation Figure 2.2 clearly demonstrates that most of the structures are not distorted much except for the structures in which one Li atom is located in close proximity of another Li atom. For such clusters the distance between the two neighboring Li atoms is in the range of 3.11 - 3.51 Å which is higher than the average Au-Au and Au-Li bond lengths in the Au₁₈Li₂ clusters as well as Li-Li bond length in Li₂ dimer (2.71 Å). To quantify the degree of deformation of the clusters we calculate the principle values of the tensor $R_{ij} = \sum_I x_i x_j$, where $x_i = \{x, y, z\}$ represents the three dimensional coordinates of the i^{th} atom in the cluster [121]. The summation is performed over all the atoms in the cluster. The principle values R_{xx} , R_{yy} and R_{zz} of this tensor define the dimensions (R_x , R_y , R_z) of the cluster through the relation $R_x = \sqrt{R_{xx}/N}$, $R_y = \sqrt{R_{yy}/N}$ and $R_z = \sqrt{R_{zz}/N}$, where N is the total number of atoms in the cluster. The calculated values for R_{xx} , R_{yy} and R_{zz} are listed in the Table 2.1.

TABLE 2.1: Principle value for R_{ij} tensor of optimized pyramidal doped Au₁₈Li₂ clusters along with Au₂₀ (T_d) cluster. All the values are given in Å².

System	R_{xx}	R_{yy}	R_{zz}
Au ₂₀	81.44	81.44	81.44
Td(S-S)	79.05	81.17	79.68
Td(S-E) ₁	80.38	80.43	79.65
Td(S-E) ₂	78.43	82.07	79.98
Td(S-E) ₃	78.41	79.52	83.19
Td(E-E) ₁	81.31	78.09	83.21
Td(E-E) ₂	79.65	80.68	82.64
Td(V-S) ₁	81.00	77.83	81.71
Td(V-S) ₂	80.52	80.52	79.68
Td(E-E) ₃	81.04	79.64	81.39
Td(E-E) ₄	79.46	89.94	75.39
Td(E-E) ₅	81.18	81.40	79.91
Td(V-E) ₁	80.87	79.25	83.78
Td(V-E) ₂	78.54	86.05	79.46
Td(V-E) ₃	79.03	86.75	79.55
Td(V-V)	80.64	81.93	82.08

These results show that all the doped structures except Td(V-E)₂ (Figure 2.2) are triaxially (i.e., principle values of the tensor R_{ij} are unequal) deformed. The structure Td(E-E)₄ where two Li atoms are the nearest neighbour along the edge, has highest degree of triaxial deformation. The

doped cluster with two Li atoms located at any two surfaces (Td(S-S)) undergoes small triaxial deformation. However, the structures Td(V-S)₂, Td(E-E)₃ and Td(E-E)₅ show triaxial oblate type of deformation because two of the three principle values of the tensor R_{ij} are almost same but less than the third one. On the other hand, Td(V-E)₂ and Td(V-V) has triaxial prolate kind of deformation. For the structure Td(S-E)₁ all the three principle values are very close to each other ($R_{xx} \approx R_{yy} \approx R_{zz}$), showing symmetric structure.

2.3.1.2 Analysis of Bond Length

To further study the structures of double-doped gold clusters we examine the bond lengths between two Li atoms and their nearest neighbors (Au atoms). In Table 2.2 different Au-Li bond lengths in the doped pyramidal Au₁₈Li₂ clusters are listed along with the corresponding Au-Au bond lengths in the pure Au₂₀ tetrahedral cluster. In this table d_{X-Y} denotes distance between two atoms located at X and Y positions, where X, Y stand for S, V and E positions. Furthermore, in this table d_{E-E}^1 and d_{E-E}^2 denote distances between two atoms which lie on the different edges and on the same edge respectively. It can be seen from the Table 2.2 that almost all the bond lengths, except d_{E-E}^2 , undergo reduction in comparison to those of the pure gold cluster. We note here that for Td(S-S) cluster maximum number (sixteen) of Au-Li bond lengths undergo reduction of average 0.06 Å. We wish to mention here that in the following we will see that this result is consistent with the results for the BE and HOMO-LUMO gap characterizing the stability of the clusters.

2.3.2 Electronic Properties of Tetrahedral Clusters

Having discussed the structures of possible isomers of double doped Au₁₈Li₂ clusters we now discuss the results for various electronic properties of these clusters.

TABLE 2.2: Average nearest neighbor distance (in Å) between Au atom and Li atom in the pyramidal doped $\text{Au}_{18}\text{Li}_2$ structures with the corresponding Au-Au distance in Au_{20} (T_d) cluster (first row). The values within the parenthesis indicate the range of the corresponding distances. In this table d_{X-Y} denotes distance between two atoms located at X and Y, where X, Y stand for S, V and E positions. Furthermore, in this table d_{E-E}^1 and d_{E-E}^2 denote distances between two atoms which lie on the different edges and on the same edge respectively.

System	d_{S-E}	d_{S-S}	d_{V-E}	d_{E-E}^1	d_{E-E}^2
Au_{20}	2.81	3.16	2.71	2.94	2.68
Td(S-S)	2.76 (2.75-2.77)	3.07	—	—	—
Td(S-E) ₁	2.76 (2.70-2.83)	2.83 (2.81-2.87)	2.69	2.74	2.82
Td(S-E) ₂	2.76 (2.72-2.79)	2.94	2.67	2.76	2.79
Td(S-E) ₃	2.72 (2.65-2.87)	2.83 (2.82-2.84)	2.63	2.83 (2.77-2.88)	2.66
Td(E-E) ₁	2.70 (2.69-2.71)	—	2.68	2.76 (2.74-2.78)	2.81
Td(E-E) ₂	2.72 (2.70-2.79)	—	2.67	2.74 (2.70-2.76)	2.80 (2.76-2.83)
Td(V-S) ₁	2.80 (2.75-2.86)	2.82 (2.79-2.85)	2.67 (2.66-2.68)	—	—
Td(V-S) ₂	2.78	2.87	2.68	—	—
Td(E-E) ₃	2.75 (2.70-2.80)	—	2.68	2.77 (2.75-2.78)	2.73
Td(E-E) ₄	2.66	—	2.61	2.66	—
Td(E-E) ₅	2.75	—	2.61	2.76	2.72
Td(V-E) ₁	2.69	—	2.67 (2.66-2.68)	2.78 (2.74-2.81)	2.80
Td(V-E) ₂	2.68	—	2.67 (2.64-2.73)	2.74	2.92
Td(V-E) ₃	2.67	—	2.58	2.66	2.75
Td(V-V)	—	—	2.66 (2.65-2.67)	—	—

2.3.2.1 Binding Energy

In order to characterize the stability of the $\text{Au}_{18}\text{Li}_2$ clusters we calculate BE of these doped clusters. The BE of these clusters are calculated using the formula given by

$$\text{BE} = -\{E(\text{Au}_{18}\text{Li}_2) - 18E(\text{Au}) - 2E(\text{Li})\} \quad (2.2)$$

where $E(\text{Au}_{18}\text{Li}_2)$, $E(\text{Au})$ and, $E(\text{Li})$ are the energies of $\text{Au}_{18}\text{Li}_2$ cluster, Au and, Li atoms respectively. The binding energies of the pyramidal $\text{Au}_{18}\text{Li}_2$ clusters are listed in the third

TABLE 2.3: Symmetry, binding energy (BE), energy gap between HOMO and LUMO (Δ_{HL}), vertical ionization potential (VIP) and vertical electron affinity (VEA) for exohedrally doped pyramidal $\text{Au}_{18}\text{Li}_2$ clusters along with Au_{20} (T_d) cluster. All the units are in eV.

System	Symmetry	BE	Δ_{HL}	VIP	VEA
Au_{20}	T_d	47.38	1.786	7.19	2.59
Td(S-S)	C_{2v}	48.40	1.742	7.09	2.53
Td(S-E) ₁	C_s	48.12	1.513	6.86	2.52
Td(S-E) ₂	C_s	48.06	1.533	6.91	2.52
Td(S-E) ₃	C_1	47.84	1.433	6.83	2.54
Td(E-E) ₁	C_2	47.62	1.412	6.74	2.50
Td(E-E) ₂	C_s	47.62	1.399	6.73	2.49
Td(V-S) ₁	C_s	47.60	1.329	6.59	2.44
Td(V-S) ₂	C_{3v}	47.59	1.272	6.55	2.47
Td(E-E) ₃	C_s	47.58	1.370	6.77	2.52
Td(E-E) ₄	C_{2v}	47.48	1.249	6.54	2.48
Td(E-E) ₅	C_s	47.46	1.507	6.85	2.42
Td(V-E) ₁	C_1	47.18	1.321	6.57	2.41
Td(V-E) ₂	C_s	47.15	1.215	6.42	2.38
Td(V-E) ₃	C_s	47.14	1.336	6.41	2.28
Td(V-V)	C_{2v}	46.86	1.324	6.51	2.35

column of Table 2.3. From this table it can be seen that $\text{Au}_{18}\text{Li}_2$ cluster with two Li atoms located at the surfaces of tetrahedral structure (Td(S-S)) possesses the highest BE (48.40 eV). The BE of this cluster is 1.02 eV higher than that of Au_{20} pyramidal structure and 0.44 eV more than that of the most stable isomer Td-S of singly doped Au_{19}Li cluster [19]. We also observe that for $\text{Au}_{18}\text{Li}_2$ cluster with both the dopant atoms situated at the vertex positions of the pyramidal structure is the configuration with lowest BE (46.86 eV). All other doped clusters with two Li atoms situated at different locations in the pyramid possess binding energies lying

between these two extreme values. Following trend is observed for the BE of all the doped pyramidal clusters: $BE(Td(S-S)) > BE(Td(S-E)) > BE(Td(E-E))$ and $BE(Td(V-S)) > BE(Td(V-E)) > BE(Td(V-V))$. The reason for the increase in BE can be attributed to the larger bond energy of Au-Li bond (3.05 eV) as compared to the Au-Au bond (2.32 eV) in their respective dimer configurations.

2.3.2.2 HOMO-LUMO gap, Ionization Potential and Electron Affinity

We now discuss the results for HOMO-LUMO gap, IP and EA, which characterize chemical stability of a cluster. The results for HOMO-LUMO gap of all the pyramidal $Au_{18}Li_2$ structures are listed in the fourth column of Table 2.3. Similar to the results for BE, Td(S-S) cluster also possesses the largest HOMO-LUMO energy gap of magnitude 1.742 eV, which is very close to that of the Au_{20} pyramidal cluster (1.786 eV). Due to this large energy gap the Td(S-S) cluster should be associated with high chemical stability. We wish to point out here that the HOMO-LUMO gap of a singly doped Td-S cluster is 1.671 eV [19]. The corresponding result for $Au_{18}Li_2$ indicates that the HOMO-LUMO gap may be enhanced by doping more than one Li atom at other surfaces of the pyramidal structure. This opens up a possibility that the HOMO-LUMO gap can be tuned in desired fashion by multiple Li doping and this possibility will be explored further in more detail later. We would like to mention that unlike Td(S-S) cluster, no enhancement in HOMO-LUMO gap is observed for either Td(E-E) or Td(V-V) clusters.

Next, we focus our attention on IP and EA of the exohedrally doped clusters. Note that the calculations of IP and EA are carried out with the assumption that the lowest-energy geometry of a charged cluster is same as that of the neutral ones, and the quantities so calculated are called as vertical IP (VIP) and vertical EA (VEA). The values of VIP and VEA are calculated using the following two equations,

$$VIP = -\{E(Au_{18}Li_2) - E(Au_{18}Li_2^+)\} \quad (2.3)$$

$$VEA = -\{E(Au_{18}Li_2^-) - E(Au_{18}Li_2)\} \quad (2.4)$$

where, $E(\text{Au}_{18}\text{Li}_2)$, $E(\text{Au}_{18}\text{Li}_2^+)$ and $E(\text{Au}_{18}\text{Li}_2^-)$ are the energies of the neutral, cationic and anionic $\text{Au}_{18}\text{Li}_2$ clusters, respectively. The calculated values of VIP and VEA of the pyramidal clusters are tabulated in the fifth and sixth columns of Table 2.3 respectively. The most stable (both energetically and chemically) isomer Td(S-S) also has the highest VIP among all the $\text{Au}_{18}\text{Li}_2$ isomers. We compare VIP and VEA values obtained in the present study with the values reported for Td-S in Ref. [19] and find that with the second doping of Li atom at any of the remaining three surface locations results in an increase in the VIP by 0.06 eV and a decrease in the VEA value by 0.04 eV. This small increase in the value of VIP is due to the lowering of the HOMO of the doped Td(S-S) cluster. However, it is observed that no enhancement in VIP is observed for the clusters with Li atoms located at the two vertices or two edges, which are found to be less stable. It is interesting to note that although VIP of Li atom is lower than that of an Au atom, VIP of Td(S-S) cluster is higher than that of Td-S cluster. Clearly, it is due to a stronger interaction of a Li atom located on the surface with the neighboring Au atoms resulting in transfer of electronic charge from the Li atom to the Au atoms.

2.3.3 Properties of Cage-like $\text{Au}_{20-n}\text{Li}_n$, $n = 2$ Clusters

Having discussed the results for various properties of tetrahedral $\text{Au}_{18}\text{Li}_2$ clusters we now focus our attention on the results for some of the highly stable cage-like structures of $\text{Au}_{18}\text{Li}_2$ cluster with one doping at the endohedral location and the other one at one of the exohedral positions. In Figure 2.3 we display the optimized structures of 15 of these stable cage-like isomers ($\text{Au}_{18}\text{Li}_2(\text{Cj})$, where $j = 1 - 15$) in the decreasing order of BE. We observe that the cage-like structures with flat surfaces ($\text{Au}_{18}\text{Li}_2(\text{C1})$ to $\text{Au}_{18}\text{Li}_2(\text{C6})$, termed as *flat cage-like* structures), which are constructed from the truncated tetrahedron, are energetically more stable than the other cage-like isomers ($\text{Au}_{18}\text{Li}_2(\text{C7})$ to $\text{Au}_{18}\text{Li}_2(\text{C15})$) with curved surfaces (termed as *other cage-like* structures). The various properties of the cage-like structures are listed in Table 2.4. The BE of these clusters are given in the third column of Table 2.4. The BE of the *flat cage-like* structures dominates over the *other cage-like* structures. This is reflected in the lowering of the average Au-Li bond length of the *flat cage-like* structures as compared to the *other cage-like*

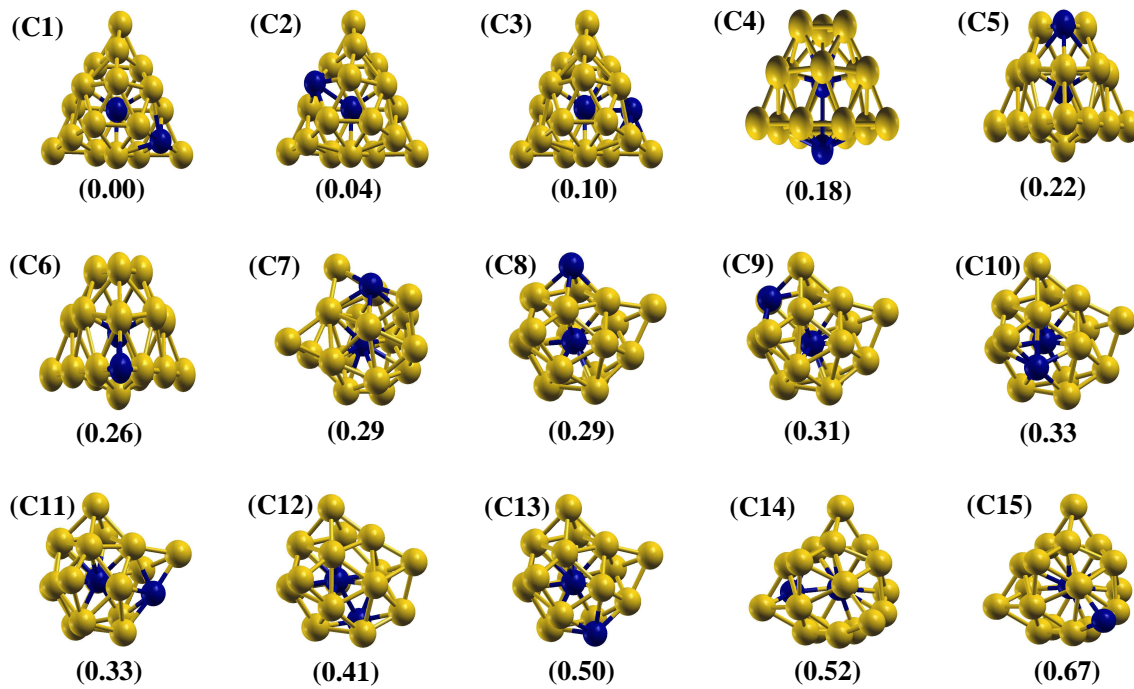


FIGURE 2.3: Optimized geometries of cage-like doped $\text{Au}_{18}\text{Li}_2$ clusters ((C1)-(C15)) in decreasing order of BE. The values within the parentheses indicate the relative BE (in eV) with respect to the isomer $\text{Au}_{18}\text{Li}_2(\text{C1})$ which is represented in the figure as (C1).

TABLE 2.4: Symmetry, binding energy (BE), energy gap between HOMO and LUMO (Δ_{HL}), vertical ionization potential (VIP) and vertical electron affinity (VEA) for doped cage-like $\text{Au}_{18}\text{Li}_2$ clusters along with Au_{20} (T_d) cluster. All the units are in eV.

System	Symmetry	BE	Δ_{HL}	VIP	VEA
Au_{20}	T_d	47.38	1.786	7.19	2.59
$\text{Au}_{18}\text{Li}_2(\text{C1})$	C_s	48.05	0.984	6.66	2.79
$\text{Au}_{18}\text{Li}_2(\text{C2})$	C_s	48.00	1.081	6.69	2.65
$\text{Au}_{18}\text{Li}_2(\text{C3})$	C_1	47.95	1.070	6.80	2.85
$\text{Au}_{18}\text{Li}_2(\text{C4})$	C_{3v}	47.87	0.968	6.64	2.81
$\text{Au}_{18}\text{Li}_2(\text{C5})$	C_s	47.82	0.920	6.60	2.79
$\text{Au}_{18}\text{Li}_2(\text{C6})$	C_s	47.78	1.052	6.54	2.61
$\text{Au}_{18}\text{Li}_2(\text{C7})$	C_1	47.76	0.896	6.57	2.78
$\text{Au}_{18}\text{Li}_2(\text{C8})$	C_s	47.75	0.838	6.42	2.69
$\text{Au}_{18}\text{Li}_2(\text{C9})$	C_1	47.73	0.962	6.59	2.74
$\text{Au}_{18}\text{Li}_2(\text{C10})$	C_1	47.71	0.928	6.61	2.78
$\text{Au}_{18}\text{Li}_2(\text{C11})$	C_1	47.71	0.928	6.61	2.47
$\text{Au}_{18}\text{Li}_2(\text{C12})$	C_1	47.64	0.866	6.51	2.75
$\text{Au}_{18}\text{Li}_2(\text{C13})$	C_s	47.55	0.914	6.17	2.74
$\text{Au}_{18}\text{Li}_2(\text{C14})$	C_1	47.52	0.895	6.55	2.77
$\text{Au}_{18}\text{Li}_2(\text{C15})$	C_1	47.38	0.764	6.17	2.52

clusters. We note that the BE of the *flat cage-like* clusters are comparable with the BE of the exohedrally doped tetrahedral $\text{Au}_{18}\text{Li}_2$ clusters.

Next, we discuss the HOMO-LUMO gaps of all the cage-like structures and find that these are very small as compared to those of the exohedrally doped tetrahedral $\text{Au}_{18}\text{Li}_2$ clusters (see Table 2.3 and Table 2.4). Comparison of the HOMO-LUMO gaps of the different cage-like structures shows that except for $\text{Au}_{18}\text{Li}_2(\text{C5})$ cluster, the HOMO-LUMO gaps of the *flat cage-like* structures are in general higher than those of the *other cage-like* structures indicating a larger chemical stability for the former. We find that there is no increase in the HOMO-LUMO gap of the singly doped (at the endohedral site) cage-like structures after the doping of another Li atom in any of the exohedral sites.

Having discussed the results for both tetrahedral and cage-like structures we wish to make few remarks regarding the stability of the doped clusters with tetrahedral geometry. We reiterate here that, in case of singly surface doped tetrahedral Td-S structures, a definite increase in the HOMO-LUMO gap is observed as the number of Li doping at the surface sites is increased from one to two, leading to the Td(S-S) cluster. We note that this cluster has the highest HOMO-LUMO gap as well as the highest BE among all the isomers of $\text{Au}_{18}\text{Li}_2$ cluster. The stability of Td(S-S) cluster can be understood by considering the nature of chemical bonding between Li and Au atoms in the cluster. When a Li atom is doped in the clusters, at the dopant site a positive charge centre is created due to the partial donation of the 2s-electron by Li. As a result of this, the surrounding Au atoms become slightly negative in nature. This leads to strong attraction between the Li atom and surrounding Au atoms. When we dope two Li atoms in the system, it creates two positive charge centres surrounded by more negatively charged Au atoms. If these two positive charge centres are not closely spaced and surrounded by more number of Au atoms, then we get the more stable structures. On the other hand, when two positive centres are not well separated then the stability is reduced due the repulsion between these two centres. Hence, we find that the bi-doped cluster with Li atoms at any of the two surface sites of the pyramidal Au_{20} cluster is the most stable one due to reduced Au-Li and Au-Au bond lengths.

The average Au-Li bond length reduces by 0.06 Å as compared to the corresponding Au-Au bond length in Au₂₀ cluster due to doping by two Li atoms at the two surface positions.

2.4 Effect of Doping of More Than Two Li Atoms

The increase in the HOMO-LUMO gap in the Td(S-S) cluster as compared to that of Td-S system indicates that the gap may be enhanced by doping with more than two Li atoms at the other surface sites. Moreover, from the calculated values of BE, VIP and HOMO-LUMO gap of Au₁₈Li₂ isomers as discussed above, it is clear that the Li atoms favor to occupy the surface sites in the pyramidal Au₂₀ cluster. This motivates us to probe the Li-doping in the pyramidal Au₂₀ cluster beyond double doping. In Table 2.5 we present the result for symmetry, BE, HOMO-

TABLE 2.5: Symmetry, binding energy (BE), energy gap between HOMO and LUMO (Δ_{HL}) and vertical ionization potential (VIP) for Au₂₀ and Au_{20-n}Li_n ($n = 1 - 4$) clusters. All the units are in eV.

System	Symmetry	BE	Δ_{HL}	VIP
Au ₂₀	T _d	47.38	1.786	7.19
Td-S	C _{3v}	47.96	1.671	7.03
Td(S-S)	C _{2v}	48.40	1.742	7.09
Td(S-S-S)	C _{3v}	48.78	1.819	7.18
Td(S-S-S-S)	T _d	49.14	2.117	7.34

LUMO gap (Δ_{HL}), and VIP of different surface doped Au_{20-n}Li_n, $n = 1 - 4$) clusters along with pure Au₂₀ cluster to show the effect of higher Li doping. Interestingly, we find that Li doping at three surface sites results in an energy gap of 1.819 eV which is greater than that of Au₂₀ tetrahedral structure. We can see that the increase in BE and HOMO-LUMO gap continues up to four Li doping and we achieve a highly symmetric (T_d) Td(S-S-S-S) cluster (all the four Li atoms are located at the four surfaces of Au₂₀) with a very high HOMO-LUMO gap of 2.117 eV and BE of 49.14 eV. This shows that the Td(S-S-S-S) cluster has 0.331 and 1.76 eV higher energy gap and BE, respectively, than those of Au₂₀ pyramidal structure. This high stability of the Td(S-S-S-S) cluster may be due to the highly symmetric charge distribution around each

Li and Au atoms. This phenomenon of highly symmetric charge distribution leading to a high stability is also observed in case of pyramidal Au_{20} cluster.

2.5 Density of States of $\text{Au}_{20-n}\text{Li}_n$, $n = 1 - 4$ Clusters

To gain more insight into the enhancement of stability of the doped clusters we study the density of states (DOS) and its evolution with number of Li atom doping. In Figure 2.4 we plot DOS

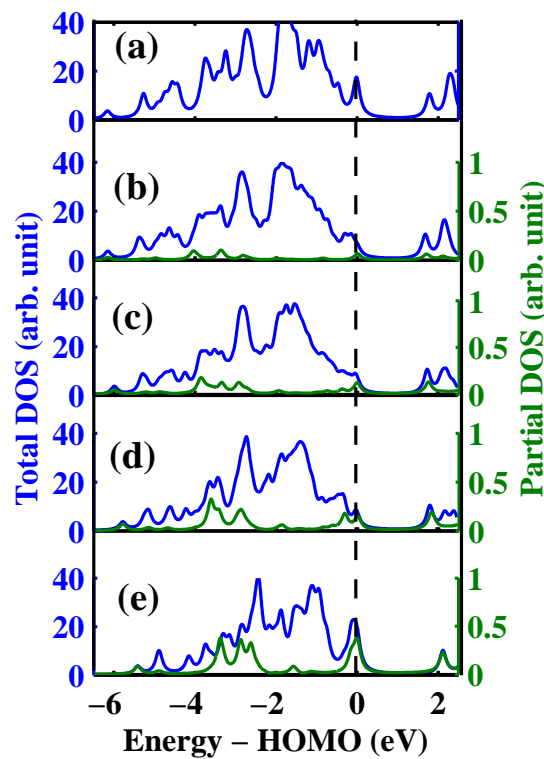


FIGURE 2.4: Total DOS (blue) of the $\text{Au}_{20-n}\text{Li}_n$ ($n = 0 - 4$) clusters and partial DOS (green) of Li atom in the corresponding cluster: (a) Au_{20} , (b) Td-S, (c) Td(S-S), (d) Td(S-S-S), and (e) Td(S-S-S-S). The calculations of DOS have been carried out using a Lorentzian broadening of 0.1 eV. The dashed line indicates HOMO of the doped clusters. Note that to visualize the small value of the partial DOS of Li atom we use two separate y-axes for total DOS (left side) and partial DOS (right side) with different scaling.

for all the four surface doped clusters along with the DOS of the pure Au_{20} cluster. In this figure the total DOS of the clusters and partial DOS corresponding to the contribution of Li atom are shown by blue and green curves respectively. Note that the calculations of the total

DOS (TDOS) and partial DOS (PDOS) are based on Mulliken population analysis. The PDOS indicates the weight factor of a basis function in the molecular orbitals determined by means of the Mulliken population analysis. It is very clear from this figure that the 2s electron of Li atom is hybridized with the 5d and 6s electrons of Au atoms. This hybridization is the signature of the interaction between Au and Li atoms. The amount of Li atom contribution to the total DOS increases with the increase in the number of doped Li atoms. This increasing trend is in conformity with the BE and HOMO-LUMO data presented in Table 2.5.

2.6 Vibrational Spectra of $\text{Au}_{20-n}\text{Li}_n$, $n = 1 - 4$ Clusters

The IR-spectroscopy is widely used to determine the geometrical structure of the neutral clusters [46]. Hence, we present an analysis [122] of the IR-spectra of some of the most stable

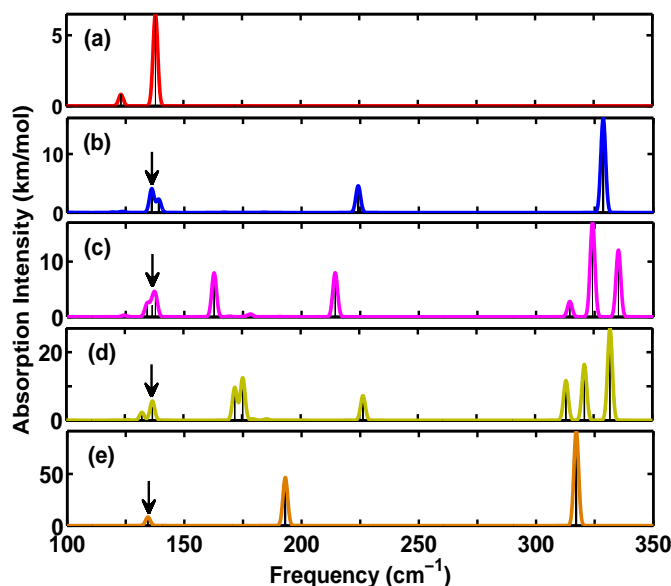


FIGURE 2.5: IR-spectra of $\text{Au}_{20-n}\text{Li}_n$ ($n = 0 - 4$) clusters: (a) Au_{20} , (b) Td-S, (c) Td(S-S), (d) Td(S-S-S), and (e) Td(S-S-S-S). These spectra are broadened by a Gaussian having a width of 1 cm^{-1} . The vertical arrows in the panel (b) to (e) indicate the positions of the Au-derived peaks.

doped clusters along with the pure Au_{20} cluster and results are displayed in Figure 2.5. From the absorption intensity plotted as a function of the vibrational frequency, we find distinct characteristic features in the IR-spectra of the clusters in the series $\text{Au}_{20-n}\text{Li}_n$ ($n = 0 - 4$). It is

observed that the pure Au_{20} cluster has a strong peak at around 138 cm^{-1} . This peak results from a triply degenerate vibrational mode of the Au atoms. All the doped structures have additionally a few strong peaks beyond 138 cm^{-1} . The analysis of the vibrational modes shows that these peaks arise mainly because of the presence of the guest Li atom which has a much smaller mass compared to the Au atom and due to the strong bonding between the Au and Li atoms. The Li atom at the surface can vibrate in different ways giving rise to different vibrational modes which we proceed to discuss below. In the single Li atom doped Td-S cluster, which has a lower symmetry (C_{3v}) than T_d symmetry of Au_{20} cluster, the triply degenerate vibrational mode of pure Au_{20} is split into two degenerate (136 cm^{-1}) and one non-degenerate (139 cm^{-1}) mode. Another peak at around 224 cm^{-1} arises due to the vibration of Li atom perpendicular to the plane of the surface of the cluster. Furthermore, a doubly degenerate peak at around 328 cm^{-1} is found, which is due to the vibration of the Li atom parallel to the surface of the cluster. For the double Li atom doped Td(S-S) cluster, the symmetry of the cluster is reduced further (C_{2v}) which leads to splitting of the Au-related peak at around 138 cm^{-1} into three non-degenerate peaks ($134, 136, 138\text{ cm}^{-1}$). A motion corresponding to a simultaneous vibration of the two Li atoms perpendicular to the plane but in opposite direction yields a peak at around 162 cm^{-1} . On the other hand, a simultaneous vibration of the two atoms which is perpendicular to the plane and in same direction (both Li atoms being in- or out-bound) gives rise to a peak at around 214 cm^{-1} . Two major peaks at around 324 cm^{-1} and 336 cm^{-1} are due to the symmetric vibration of the Li atoms parallel to the surface while an asymmetric vibration of the Li atoms gives rise to a small peak at around 315 cm^{-1} . In Td(S-S-S) cluster the asynchronous vibrations of the Li atoms perpendicular to the plane result in two peaks: a doubly degenerate peak at 171 cm^{-1} and another one at 175 cm^{-1} . On the other hand, a concurrent motion of the three Li atoms perpendicular to the surface yields a peak at 226 cm^{-1} . The vibrations of the Li atoms parallel to the surface give rise to three peaks, which consist of two degenerate modes each at around 313 cm^{-1} and 321 cm^{-1} and a non-degenerate mode at around 332 cm^{-1} . The most stable and tetrahedrally symmetric structure Td(S-S-S-S) shows three triply-degenerate peaks at around $134, 193$ and 317 cm^{-1} . The first one corresponds to Au atoms, the second and the third ones, which are very strong, arise due to the vibration of the Li atoms perpendicular and parallel to

the plane of the surface of the cluster, respectively. This IR-spectrum analysis shows that Li-doped $\text{Au}_{20-n}\text{Li}_n$ ($n = 1 - 4$) clusters exhibit strong absorption in the frequency range 300-350 cm^{-1} which is absent in the case of the pure Au_{20} cluster. This difference in the infrared spectra may be exploited in the structure determination of the doped clusters.

2.7 Conclusions

In summary, we have investigated the structural and electronic properties of the Li doped gold nano-clusters. In addition, we have discussed the IR-spectrum of the stable structures to provide a spectroscopic signature characterizing these structures. We have found that the dopant Li atoms prefer the surface positions of the pyramidal structure of Au_{20} cluster. The thermodynamic stabilities of these structures are found to be very high as compared to the pyramidal Au_{20} cluster. On the other hand, the chemical stability follows an interesting trend. It is observed that the HOMO-LUMO gap of the single Li atom doped Td-S cluster is less by around 0.1 eV as compared to that of the pure Au_{20} cluster. Whereas, the chemical stability (HOMO-LUMO gap) of two Li atoms doped Td(S-S) cluster is almost similar to that of the pyramidal Au_{20} cluster. This indicates that the chemical stability of the Li doped clusters increases as we increase the number of dopant Li atoms. We have observed that the enhancement in thermodynamic stability of doped cluster with increasing number of dopant Li atom can be attributed to the increase in the ionic nature of the Au-Li bonds. We have found that the doped Td(S-S-S-S) cluster with highly symmetric (T_d) structure possesses significantly higher BE (49.14 eV) and HOMO-LUMO gap (2.12 eV), as compared to those of pure Au_{20} cluster. These results show that Li doped gold clusters $\text{Au}_{20-n}\text{Li}_n$ ($n = 1 - 4$) offer a possibility of tuning the HOMO-LUMO gap by placing the Li atoms at appropriate positions in the tetrahedral Au_{20} cluster. Overall, it is observed that the single Li doped Td-S cluster possesses the lowest HOMO-LUMO gap among all the most stable Li doped 20-atom gold clusters. It is then expected that a single Li atom doped Au_{19}Li cluster will exhibit higher chemical reactivity. In the next chapter we present the results for the detailed study on the chemical reactivity of Li doped Au_{19}Li cluster.

Chapter 3

Chemical Properties of Li Doped Gold Nano-Clusters

In the previous chapter we predicted that the chemical reactivity of the single Li doped Au_{19}Li cluster will be higher due to its lower HOMO-LUMO gap. In order to check our prediction, in the present chapter we discuss the chemical properties of the Au_{19}Li cluster. We check the chemical reactivity of the Au_{19}Li cluster using CO molecule as a probe. We wish to mention here that the catalytic activity of the pure Au_{20} cluster towards CO and O_2 absorption has been studied both experimentally and theoretically by various research groups [14, 58, 123] and it has been found that these molecules interact weakly with the free Au_{20} cluster [14, 58]. The effect of support on the structure of Au_{20} cluster and its reactivity towards CO and O_2 molecules have also been reported in the literature [14, 60, 61, 65]. It has been demonstrated that with appropriately chosen support, charge transfer from support to Au_{20} cluster can be enhanced, which in turn leads to its structural change as well as an increase in its reactivity towards CO and O_2 . On the other hand, in another recent experimental report, Haeck et al. found that the doping of Ag in the Au_{20} cluster (Au_{19}Ag) leads to decrease in the reactivity towards CO oxidation as compared to that of pure Au_{20} cluster [124]. It is well known that the chemical activity of gold clusters can be modified by doping another atom in the cluster [20, 53, 125]. For Example, in a study, Jena et al. found that the interaction of CO with small gold clusters

(2-8 atoms) may be enhanced by doping gold clusters with H and Li atoms [126]. In the present chapter we investigate the effect of doping of Li atom on chemical reactivity of the larger gold cluster by studying the CO adsorption behavior of the Au₁₉Li clusters.

3.1 Computational Details

All calculations presented in this chapter have been carried out by employing the theory as described in Chapter 2 except the XC-functional. In this chapter all the structures are optimized within GGA level with Perdew-Burke-Ernzerhof (PBE) XC (XC) functional [92]. Note that this functional gives quite accurate results for structural and electronic properties of gold clusters and hence widely used to investigate pure as well as doped gold clusters [15, 103, 127, 128]. In order to check the suitability of the PBE XC-functional for the Au₁₉Li systems we also employ other GGA XC-functionals like PW91, BP86 and Meta-GGA type TPSS XC-functional to calculate the binding energies of the bimetallic clusters [98, 129–131].

In order to characterize the strength of interaction between CO molecule and pure or bimetallic gold clusters we calculate the adsorption energy, E_{ad} using the equation,

$$E_{ad} = -[E(cluster - CO) - E(cluster) - E(CO)] \quad (3.1)$$

where $E(cluster - CO)$, $E(cluster)$, and $E(CO)$ are the energies of the cluster-CO complex, most stable tetrahedral parent Au₂₀ or bimetallic Au₁₉Li cluster on which CO molecule has been adsorbed, and a bare CO molecule, respectively. The higher values of E_{ad} indicate stronger interaction between CO and the cluster. In the following we present the results of our calculations and discuss various electronic properties to comprehend these results.

3.2 Structural Properties of Au_{19}Li -CO Complexes

To study the adsorption of CO molecule on the bimetallic Au_{19}Li clusters first we need to know correct geometric structures of these systems. To obtain optimized geometries of Au_{19}Li -CO

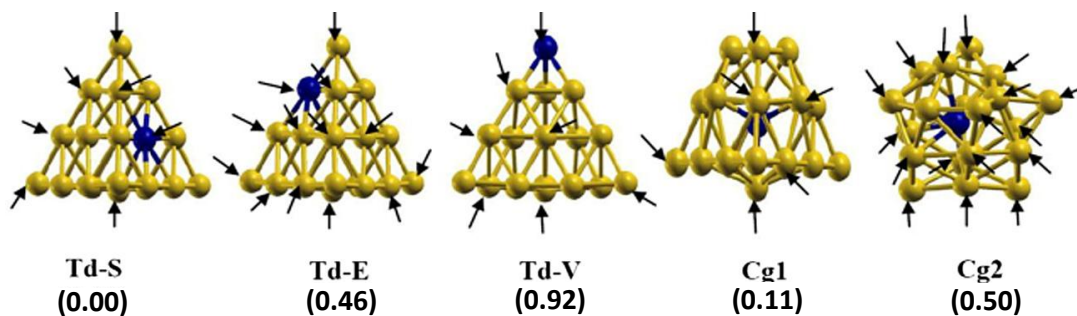


FIGURE 3.1: Optimized geometries of Au_{19}Li clusters. The arrows indicate the non-equivalent positions for CO molecule adsorption. The numbers within the parenthesis indicate the relative energies (eV) of the corresponding structure with respect to the most stable Td-S cluster. The relative binding energies presented here are calculated using PBE functional.

complexes we consider three distinct possible exohedrally doped tetrahedral and two of the most stable endohedrally doped cage-like Au_{19}Li structures, which are displayed in Figure 3.1. These geometries have been taken from our previous studies on the structures and electronic properties of gold-alkali and gold-coinage bimetallic Au_{19}M (where $\text{M} = \text{Li}, \text{Na}, \text{K}, \text{Rb}, \text{Cs}, \text{Ag}, \text{Cu}$) clusters [19, 20]. As discussed in the previous chapter that we denote the exohedrally doped tetrahedral Au_{19}Li clusters by Td-X, where Td stands for tetrahedral geometry and X refers to the location of the dopant atom (Li), where $\text{X} = \text{E}, \text{S}$, and V stand for doping at an edge site, a surface site, and a vertex site respectively, and $\text{X}=0$ represents a pure Au_{20} cluster. The two cage-like Au_{19}Li clusters where the dopant Li atom is placed at the endohedral positions are named as Cg1 and Cg2 respectively (see Figure 3.1). In the previous chapter we observed that the cluster Td-S is the most stable one among all Au_{19}Li structures [19, 20]. To make our search more exhaustive for the most stable Au_{19}Li cluster we calculate the relative binding energies of all the five isomers of Au_{19}Li cluster with respect to the most stable Td-S structure with four different XC-functionals and the corresponding results are listed in Table 3.1. From these results we can see that the energy ordering of the bimetallic Au_{19}Li clusters does not change due to the use of different XC-functionals. The relative stabilities of Au_{19}Li clusters are almost the

TABLE 3.1: Relative energies (in eV) of the five isomers of Au_{19}Li cluster.

system	Relative energy (in eV) with different XC-functionals			
	PBE	PW91	BP86	TPSS
Td-S	0.00	0.00	0.00	0.00
Td-E	0.46	0.45	0.47	0.34
Td-V	0.92	0.93	0.95	0.71
Cg1	0.11	0.12	0.17	0.09
Cg2	0.50	0.52	0.58	0.47

same for all the XC-functionals used in our calculations. However, the values of binding energy for each isomer obtained by using TPSS are consistently lower than the corresponding values calculated using the other three XC-functionals. As the binding energies for PBE functional is quite consistence with the energies calculated with other functionals like PW91, BP86 and TPSS, we discuss our main results obtained with PBE functional only. In the following we analyze the relative binding energy data further at PBE level. At this level we find that the energies of the structures Td-E and Td-V are less by around 0.46 and 0.92 eV respectively, as compared to that of Td-S structure. However, the cage-like structure Cg1 is found to be energetically very close to Td-S (difference of just around 0.11 eV), whereas, Cg2 is found to be 0.50 eV less stable as compared to that of Td-S. These results indicate that the structures Td-S and Cg1 are most likely to exist with equal probability in the experimental generation of Au_{19}Li cluster and the structures Td-E and Cg2, which are slightly less favorable, are also equally probable to be observed in the experiments. In order to understand the electronic structures of the selected five isomers of Au_{19}Li clusters we plot the energy levels corresponding to the frontier molecular orbitals of the five isomers of Au_{19}Li cluster and pure Au_{20} cluster in Figure 3.2. From this figure we can see that the pure Au_{20} cluster possesses the highest HOMO-LUMO gap, whereas, the bimetallic Cg2 cluster has the lowest value of HOMO-LUMO gap and the HOMO-LUMO gaps of the other isomers of the bimetallic Au_{19}Li clusters lie in between these two extreme values. It is also very clear from the Figure 3.2 that the presence of a Li atom shifts the HOMO of the bimetallic Au_{19}Li clusters towards the higher energy. Thus the lower value of HOMO-LUMO gap and the higher energy state of HOMO of the bimetallic clusters can increase the

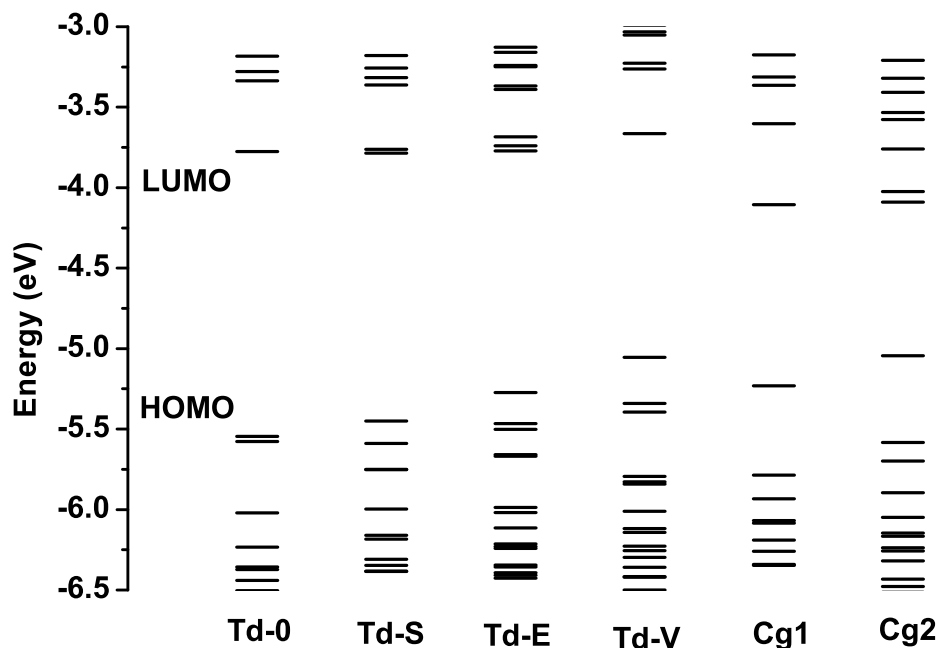
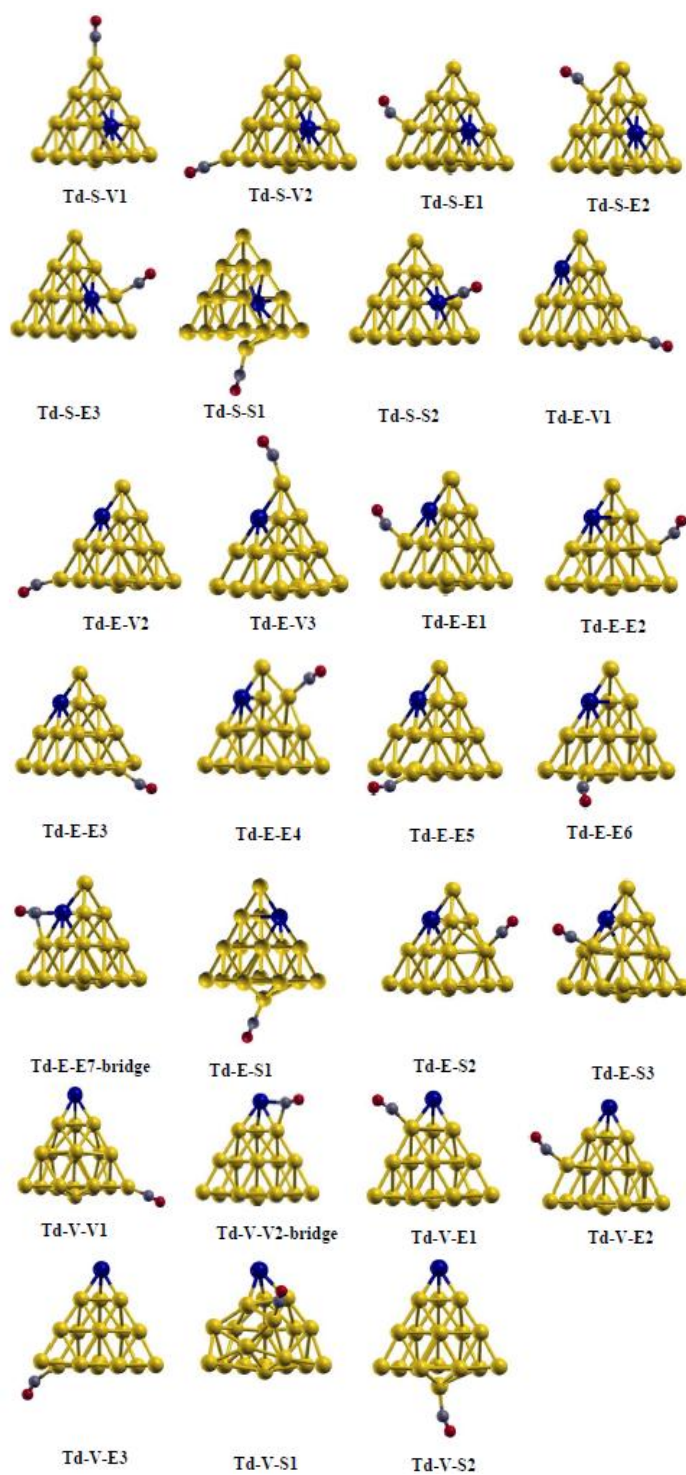


FIGURE 3.2: Energy level diagram of Au_{19}Li and Au_{20} clusters. The top most level below -4.75 eV is the HOMO and the bottom most level above -4.25 eV is the LUMO of the clusters.

chemical reactivity of these bimetallic clusters, which is the main focus of the study of the present chapter. Now, to study the adsorption of CO molecule on the five (three tetrahedral and two cage-like) isomers of Au_{19}Li cluster various possible structures of cluster-CO complex have been generated by placing the CO molecule at different non-equivalent positions of these isomers. The non-equivalent adsorption sites for CO molecule are indicated by the arrows in Figure 3.1. A CO molecule can interact with the Au atom in the cluster either via C atom (CO mode) or via O atom (OC mode). We find that the CO molecule prefers to interact with Au clusters through CO mode. So all the calculations in the present study have been carried out considering cluster-CO type of configurations only. This consideration leads to more than 50 possible geometries of Au_{19}Li -CO complex, which are taken as initial geometries for the determination of the correct structures. All these structures are then optimized at GGA level using PBE XC functional in the framework of DFT. The geometries of all the structures of tetrahedral Au_{19}Li -CO complex are shown in Figure 3.3. Following the notations for parent structures, we denote the various tetrahedral isomers of cluster-CO complex by Td-X-Yj, where Y refers to

FIGURE 3.3: Optimized geometries of the tetrahedral $\text{Au}_{19}\text{Li-CO}$ complexes.

the site of CO adsorption like E, S and V and the index j , which takes integral values indicates different Y sites in the tetrahedral geometry. From Figure 3.3 we observe that the tetrahedral structures of all the Au_{19}Li isomers (except for Td-V-S1) undergo a very small change when a CO molecule is adsorbed on these clusters. However, we note here that for CO adsorbed at the surface sites, the gold atoms lying on this surface are pulled out leading to distortion of the pyramidal structure. As a result of this, maximum distortion is observed for Td-V-S1 structure. Moreover, we note here that the adsorption of CO on the surface of Au_{19}Li clusters occurs at an angle with respect to the normal to the surface. In contrast to this for the pure Au_{20} cluster the adsorbed CO molecule points in the vertically outward direction. We also observe that for a Li atom located at one of the edge or vertex sites, CO molecule prefers to occupy a position in between the nearest Li-Au bond. This configuration is found for two structures, which we designate as Td-E-E7-bridge and Td-V-V2-bridge (see Figure 3.3).

Having discussed the optimized tetrahedral structures of cluster-CO complex we next focus our attention on the cage-like structures. As mentioned before we consider two most stable cage-like geometries of Au_{19}Li cluster from our earlier study [19]. In fact these two endohedrally doped cage-like structures (Cg1 and Cg2) possess slightly higher binding energy than a pure Au_{20} cluster. To study CO adsorption on these cage-like structures a CO molecule is placed at different sites of these two cage-like cluster. For Cg1 structure CO molecule is placed at six unique positions (shown by arrows in Figure 3.1) to generate six possible structures of cluster-CO complex, which are denoted by Cg1_i ($i = 1 - 6$). On the other hand, for Cg2 structure there are seventeen non-equivalent Au positions, which are considered for CO absorption. These seventeen structures are denoted by Cg2_i ($i = 1 - 17$). All the optimized geometries of the cluster-CO complexes for the cage-like structures are shown in the Figure 3.4. Note that we do not get converged results for Cg2_17 complex and hence the geometry corresponding to this complex is not listed in this figure. From Figure 3.4 it can be again seen that a CO molecule favors the low coordinated sites of the bimetallic cluster for adsorption on it. As a result of this less symmetric Cg2_i cage-like structures undergo significant distortion in their shapes as compared to more symmetric Cg1_i structures.

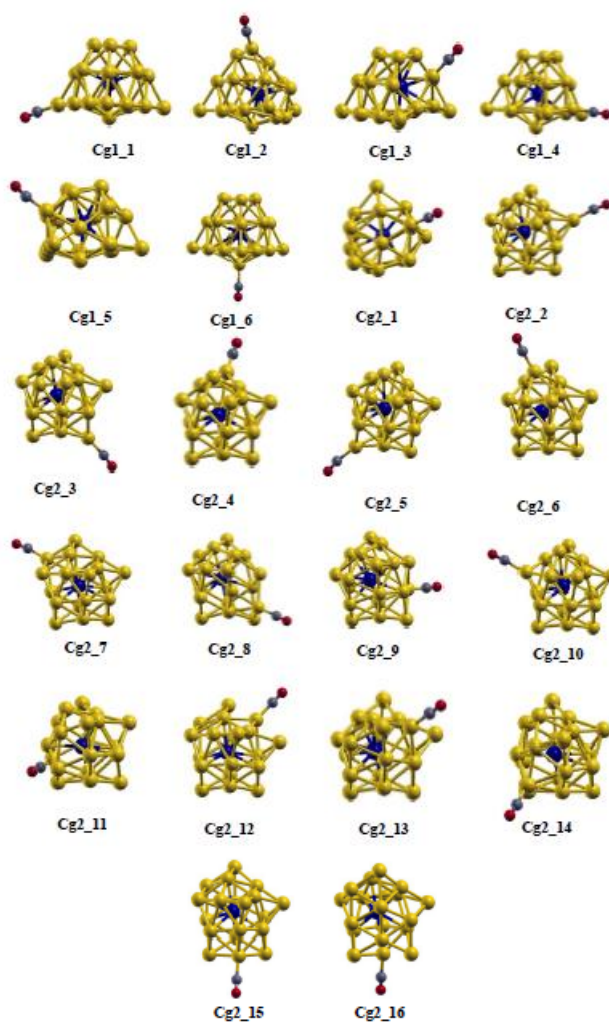


FIGURE 3.4: Optimized geometries of the cage-like $\text{Au}_{19}\text{Li-CO}$ complexes.

In the next section we next present the results for the interaction energy and the other electronic properties of above mentioned isomers of the cluster-CO complex.

3.3 Interaction of CO Molecule with Au_{19}Li Clusters

Before we discuss the results for the interaction of CO molecule with Au_{19}Li cluster we first present the results for the interaction of CO molecule with Au_{20} cluster to establish the accuracy of our calculation as well as for completeness. The results for the adsorption energy of CO on pure Au_{20} clusters are compiled in Table 3.2 along with the corresponding data from the

TABLE 3.2: Adsorption energy (E_{ad}), the distance between Au and C and C-O bond length (d_{Au-C} and d_{C-O} respectively) and Au-C and C-O bond stretching frequencies (ν_{Au-C} and ν_{C-O} respectively) for Au_{20} -CO complex.

system	adsorption energy, E_{ad} (eV)	bond length analysis (Å)		frequency analysis (cm^{-1})	
		d_{Au-C}	d_{C-O}	ν_{Au-C}	ν_{C-O}
Td-0-E	0.45 (0.54) ^b	2.021	1.147	319	2027
Td-0-S	0.37 (0.38) ^b	1.986	1.144	335	2056
Td-0-V	0.82 (0.84) ^b	1.977	1.144	354	2063

^aTd-0-E, Td-0-S and Td-0-V are the Au_{20} -CO complexes where the CO is adsorbed at edge (E), surface (S) and vertex (V) respectively.

^bThe values within the parenthesis are taken from Ref. [14].

already published work [14]. It can be seen from this table that our results for E_{ad} match quite well with those of Ref. [14] except for the case of CO molecule adsorbed at the edge site. This discrepancy in the results may be due to the use of different methods employed and different choice of XC functionals in the two calculations. Now, we discuss the results for the adsorption energy of CO molecule on various isomers of $Au_{19}Li$ clusters.

3.3.1 Adsorption of CO on Tetrahedral $Au_{19}Li$ Clusters

The energy corresponding to the adsorption of a CO molecule on exohedrally doped tetrahedral isomers of $Au_{19}Li$ cluster are listed in Table 3.3. These results clearly indicate that a CO molecule always favours to get adsorbed at a vertex site (only Au occupied) of the pyramidal structure, which has the lowest number of nearest neighbours (minimum co-ordination), irrespective of the location of the dopant Li atom in the cluster. Among all possible exohedrally doped tetrahedral isomers we find that a configuration with Li atom at the vertex site and a CO molecule adsorbed at another vertex location (Td-V-V1), yields highest value of $E_{ad} = 0.91$ eV, which is around 0.1 eV higher than the adsorption energy of CO molecule on Au_{20} vertex. On the other hand, we observe no adsorption of CO molecule at the vertex site if it is already occupied by a Li atom, rather, in this case the CO molecule prefers to reside at the middle of Au-Li bond which leads to appearance of bridge-like structures (Td-V-V2-bridge) with $E_{ad} = 0.61$ eV.

TABLE 3.3: Adsorption energy (E_{ad}) for the tetrahedral $Au_{19}Li$ -CO complexes

System	Adsorption energy (eV)
Td-S-V1	0.82
Td-S-V2	0.80
Td-S-E1	0.46
Td-S-E2	0.45
Td-S-E3	0.39
Td-S-S1	0.37
Td-S-S2	0.22
Td-E-V1	0.82
Td-E-V2	0.81
Td-E-V3	0.74
Td-E-E1	0.66
Td-E-E2	0.46
Td-E-E3	0.45
Td-E-E4	0.45
Td-E-E5	0.44
Td-E-E6	0.42
Td-E-E7-bridge	0.40
Td-E-S1	0.43
Td-E-S2	0.37
Td-E-S3	0.33
Td-V-V1	0.91
Td-V-V2-bridge	0.61
Td-V-E1	0.58
Td-V-E2	0.47
Td-V-E3	0.46
Td-V-S1	0.43
Td-V-S2	0.29

Unlike a vertex site, a surface site which has six nearest neighbours is generally found to be less favourable site for CO adsorption with adsorption energy varying from 0.2 - 0.4 eV. We note that adsorption of a CO molecule on the top of Li atom occurs when it is located at one of the surface site of tetrahedral with a very low value of adsorption energy ($E_{ad} = 0.22$ eV). From the results presented in Table 3.3 we conclude that CO molecule prefers a lowest-coordinated site for adsorption on the exohedrally doped tetrahedral $Au_{19}Li$ cluster. Note that the preference of the low-coordinated site for adsorption of CO molecule in various pure and doped gold clusters has already been emphasized in the previous works [132–134]. In this context we wish to mention that it has already been shown that Na atom doped at the endohedral location in the tetrahedral structure of Au_{20} cluster exhibits a strong tendency to adsorb CO molecule at the

vertex site [14].

3.3.2 Adsorption of CO on Cage-like Au₁₉Li Clusters

Having discussed the adsorption energies of tetrahedral isomers of Au₁₉Li-CO complex we now present the results for cage-like isomers of the same complex. The results for the adsorption

TABLE 3.4: Adsorption energy (E_{ad}) for the cage-like Au₁₉Li-CO complexes

System	Adsorption energy (eV)
Cg1_1	1.01
Cg1_2	0.74
Cg1_3	0.61
Cg1_4	0.57
Cg1_5	0.51
Cg1_6	0.39
Cg2_1	1.15
Cg2_2	1.04
Cg2_3	0.90
Cg2_4	0.88
Cg2_5	0.82
Cg2_6	0.79
Cg2_7	0.72
Cg2_8	0.70
Cg2_9	0.70
Cg2_10	0.70
Cg2_11	0.67
Cg2_12	0.67
Cg2_13	0.63
Cg2_14	0.62
Cg2_15	0.58
Cg2_16	0.58

energy of CO molecule on cage-like isomers of Au₁₉Li cluster are compiled in Table 3.4. We observe from this table that seven cage-like isomers, namely, Cg1_1, Cg2_1, Cg2_2, Cg2_3, Cg2_4, Cg2_5, and Cg2_6 show very strong affinity towards adsorption of CO molecule which are comparable or higher than that observed for CO adsorption on pure Au₂₀ cluster. The highest value of $E_{ad} = 1.15$ V is found for the case of Cg2_1 isomer of Au₁₉Li cluster. Note that this value of adsorption energy is significantly higher (around 40 percent) than the corresponding value for pure Au₂₀ cluster. Similarly Cg1_1 isomer also interacts quite strongly ($E_{ad} = 1.01$

eV) with the CO molecule. Like tetrahedral isomers, for cage-like isomers also we observe that the CO molecule prefers to interact with the Au atoms at the low-coordinated cluster sites. From the results of Table 3.3 and 3.4 we conclude that doping of gold cluster with Li atom results in enhancement of CO adsorption energy. Moreover, we also observe that the endohedrally doped Au_{19}Li clusters exhibit significantly better adsorption of CO molecule than its exohedrally doped tetrahedral counterpart. The higher value of CO adsorption energy for the endohedrally doped Cg2_1 cluster may be attributed to the lower value of HOMO-LUMO gap (0.957 eV, also see Figure 3.2) of this cluster as compared to the corresponding exohedrally doped isomers (1.671 - 1.402 eV) [19]. We note here that the bimetallic cluster Cg2 which shows the highest propensity towards CO adsorption is slightly less stable as compared to the most stable Td-S structure but it is more stable than pure Au_{20} cluster. Thus it is possible that Cg2 will be produced in the gas phase along with the other isomers of Au_{19}Li cluster. Alternatively, it is established that by choosing a suitable solid surface as a support even energetically less favourable isomers can be stabilized [17]. It is then quite clear that the energy ordering of the adsorbed clusters will be different as compared to that of the free clusters, and it might be possible to observe Cg2 experimentally.

3.3.3 Electronic Structure of Cluster-CO Complexes

In order to get better insight into the mechanism of CO adsorption on Au_{19}Li cluster we now carry out analysis of charge distribution, relevant bond lengths, and vibrational frequencies of cluster-CO complexes. The results for the charge distribution at the adsorption site, Au-C ($d_{\text{Au-C}}$) and C-O ($d_{\text{C-O}}$) bond lengths after adsorption, and their stretching frequencies ($\nu_{\text{Au-C}}$ and $\nu_{\text{C-O}}$) are listed in Table 3.5. Note that we present the results for only those structures, which possess CO adsorption energy comparable or higher with respect to that of $\text{Au}_{20}\text{-CO}$ complex (0.82 eV). The charge distributions are obtained by employing Mulliken population analysis. It can be clearly seen that for all the isomers (both exohedrally doped tetrahedral and endohedrally doped cage-like) with large value of adsorption energy, the adsorption sites are associated with anionic character. After adsorption of CO molecule, the Au atom at the

TABLE 3.5: Mulliken charges, the Au-C bond distance (d_{Au-C}) and C-O bond length (d_{C-O}), Au-C and C-O bond stretching frequencies (ν_{Au-C} and ν_{C-O} respectively) for the selected $Au_{19}Li$ -CO complexes.

System	Mulliken charge analysis			Bond length analysis (Å)		Frequency analysis (cm^{-1})	
	Charge on Adsorption site		Charge on CO after adsorption	d_{Au-C}	d_{C-O}	ν_{Au-C}	ν_{C-O}
	Before CO adsorption	After CO adsorption					
Td-S-V1	-0.0718	0.0889	0.0109	1.977	1.143	355	2066
Td-S-V2	-0.0682	0.1006	0.0086	1.977	1.144	355	2062
Td-E-V1	-0.0694	0.0941	0.0057	1.978	1.144	355	2062
Td-E-V2	-0.0833	0.0946	-0.0158	1.982	1.146	359	2043
Td-V-V1	-0.0773	0.1148	-0.0047	1.963	1.145	372	2057
Cg1_1	-0.0307	0.1142	0.0003	1.963	1.145	374	2070
Cg2_1	-0.0019	0.1184	-0.0234	1.962	1.146	374	2047
Cg2_2	-0.0327	0.0999	-0.0305	1.953	1.147	386	2042
Cg2_3	-0.0421	0.1100	-0.0128	1.96	1.146	373	2053
Cg2_4	-0.0737	0.1120	0.0009	1.962	1.145	372	2061
Cg2_5	-0.0415	0.0983	-0.0186	1.972	1.146	363	2045
Cg2_6	-0.0302	0.1468	-0.0080	1.971	1.145	363	2056

adsorption site transfers a fraction of its charge to the neighbouring atoms in the cluster and also to the CO molecule. However, we do not observe any correlation between the charge transfer from cluster to CO molecule and the adsorption energy. For example, we find that for the case of isomer Cg2_1 with the highest value of adsorption energy, charge transfer has taken place from cluster to CO, whereas for Cg1_1 with the third highest adsorption energy, a charge transfer in the reverse direction is observed. Similarly, no definite trend is observed for other isomers. Furthermore, we observe that the isomers for which CO molecule acts as electron acceptor (Td-E-V2, Td-V-V1, Cg2_1, Cg2_2, Cg2_3, Cg2_5, Cg2_6) the C-O bond length undergoes elongation by 0.01 Å or more (except for Td-V-V1 and Cg2_6, where the charge transfers to CO is very small) in comparison to the free CO molecule bond length ($d_{C-O} = 1.136$ Å). This increase in C-O bond length may be attributed to the back donation from the cluster to the $2\pi^*$ anti-bonding orbital of CO molecule [17, 133, 134]. On the other hand, for

CO molecule acting as electron donor, the increase in C-O bond length is less ($< 0.01 \text{ \AA}$) as compared to that observed in the case where CO acts as electron acceptor. Moreover, a higher red-shift in the CO stretching frequency with respect to free CO frequency ($\nu_{C-O} = 2122 \text{ cm}^{-1}$) is observed for the case when CO molecule act as an electron acceptor than the case when it acts as an electron donor.

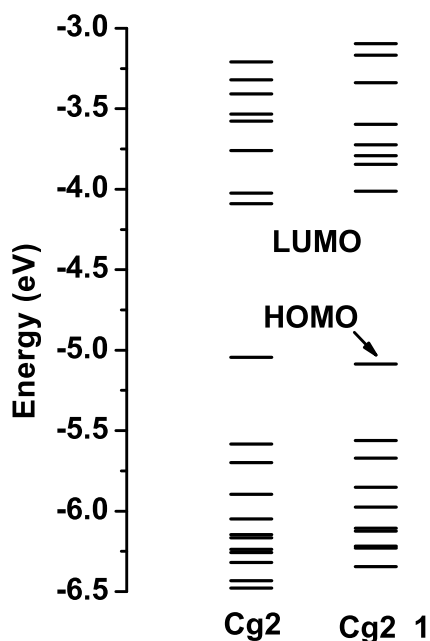


FIGURE 3.5: Energy level diagram of Cg2 and Cg2_1 clusters.

In order to understand the electronic structures of Cg2_1 complex we plot the energy levels of the frontier molecular orbitals of this complex and its parent structure Cg2 in Figure 3.5. From this figure it is very clear that when a CO molecule is adsorbed on Cg2 cluster results in larger HOMO-LUMO gap as the HOMO shifts towards the lower value, whereas, LUMO shifts towards the higher energy. This indicates that the chemical stability of Cg2 cluster increases as a CO molecule is adsorbed on it. This in turn also suggests that the isomer Cg2 of Au_{19}Li cluster may act as good catalytic agent for CO oxidation reaction.

3.4 Conclusions

In summary, we investigate the CO adsorption on bimetallic Au_{19}Li cluster by employing *ab-initio* density functional theory based method. We observe that the CO adsorption on Au_{19}Li cluster is highly dependent on the site of the adsorption. The Li sites are least favorable, whereas, the Au occupied low coordinated and anionic sites are the most favorable for CO adsorption among all the bimetallic cluster-CO configurations. In accordance with our prediction in the previous chapter, here we observe that Li doping can enhance the adsorption energy of CO molecule with Au_{19}Li cluster over that of pure Au_{20} cluster. In particular, we find that Cg2_1 complex possesses very high adsorption energy of 1.15 eV, which is 40 percent higher than that of pure Au_{20} -CO complex. The back donation, which is one of the most important factors for CO oxidation is also found to be occurring for Cg2_1 complex. We observe that for some of the exohedrally and endohedrally doped Au_{19}Li isomers, C-O bond length undergoes elongation leading to red shift in C-O stretching frequency. This elongation in C-O bond length is attributed to the back donation from the cluster to the anti-bonding $2\pi^*$ level of CO, which leads to the weakening of C-O bond. Specifically, we find that for endohedrally doped cage-like Cg2_1 isomer of Au_{19}Li cluster, CO adsorption results in a back donation of charges from the cluster to CO molecule, which results in an elongation of the C-O bond length by 0.01 \AA and a red-shift of 75 cm^{-1} in the C-O stretching frequency. These results indicate that by doping Li atom at endohedral location in cage-like structure of Au_{20} cluster, it is possible to enhance the adsorption energy of CO molecule on this cluster and also to increase the C-O bond length. Consequently, it may be expected that such bimetallic cluster may be a suitable catalytic agent for carrying out CO oxidation reaction. Here, we wish to point out that our present study indicates that the tetrahedral structure of Au_{19}Li cluster may be lost when a CO molecule is adsorbed on it. Therefore, we ask the question whether the chemical reactivity of the 20-atom gold cluster can be enhanced or not keeping the tetrahedral geometry intact. In the next chapter we will address this question.

Chapter 4

Structural and Chemical Properties of Pt Doped Gold Nano-Clusters

The results presented in the previous chapter indicate that the chemical reactivity of the 20-atom gold cluster can be enhanced by doping it with a single Li-atom. In contrast to this it has been reported in Refs. [124, 125] that the doping of coinage metals like Cu and Ag in gold clusters results in reduction of reactivity of these clusters toward CO adsorption. On the other hand, the studies on the interaction of CO molecule with Pt doped small gold clusters (Au_nPt) with maximum up to 13 atoms unanimously concluded that the presence of Pt atom always enhances the adsorption of CO molecule on the gold clusters [51, 52, 135–137]. Moreover, it has also been found that the Pt site is more favorable for CO adsorption when both Pt and Au sites are available for CO adsorption. For example, Morrow *et al.* reported that the CO adsorption energy on the Pt site is more than 1 eV higher than that of adsorption on Au site [136]. Furthermore, it is important to note that adsorption of CO molecule on Au atoms located in the neighborhood of a Pt atom also shows marked improvement as compared to the case when Au atoms are present in pure cluster. The explanation for the enhancement in CO adsorption on Pt doped gold clusters is given in terms of charge transfer from the cluster to the CO molecule and the shift in d-band center of the adsorbing atom [136]. From these results we infer that the doping of Pt atom in the gold clusters can provide more number of active adsorption sites in

the doped gold clusters as compared to those in the pure ones. Overall, it is very clear that the presence of Pt in the gold clusters of smaller sizes is very promising for enhancing the catalytic activities of these clusters towards CO oxidation reactions. In conformity with the theoretical predictions, in an experiment by Pedersen *et al.* it was observed that CO adsorption on Pt atom of Au-Pt mixed island on Au(111) is stronger as compared to that on clean Pt(111) surface [138]. This strong reactivity of the supported island was explained in terms of the shift of d-band centre of the adsorbate. The results of this experiment demonstrated that the presence of Au atoms can stimulate the reactivity of Pt atom. Moreover, the supported Au-Pt nano-particles of core size $\sim 2 - 4$ nm with different mixing proportion are also synthesized and their reactivity have been investigated using CO molecule as a probe [139, 140]. These authors observed a significant enhancement of CO adsorption on these bimetallic nano-particles. However, to the best of our knowledge no detail theoretical analysis to explain the reactivity of the Au-Pt nano-particles exists in the literature. We expect that the theoretical electronic structure investigations of Au-Pt clusters of larger size may help to understand the experimental observations for the Au-Pt nano-particles.

Note that in an earlier report by Leppert *et al.* [18] devoted to the study of the core-shell (Pt atoms occupy the core position surrounded by Au atoms) growth of 20 and 40-atoms Au-Pt bimetallic clusters only the tetrahedral structure of Au_{20} and one cage-like structures of Pt_{20} were explored for determination of ground state geometries of Au_{19}Pt cluster. These authors reported only the exohedral-Pt structures of Au_{19}Pt cluster and no endohedral-Pt structure was considered. Whereas, our study is more focused on the structural and chemical properties of Au_{19}Pt cluster. We have considered both exohedral and endohedral structures of Au_{19}Pt cluster which are based on the tetrahedral, cage-like and tube-like geometries of Au_{20} and Au_{19} clusters. Moreover, the higher reactivity of the bimetallic Au-Pt clusters was mentioned in the earlier reports by Leppert *et al.* [18, 141], but the detail study on the reactivity was missing. The present chapter provides a complete understanding of not only the structural aspects of the Au_{19}Pt clusters but also the chemical property of the Au_{19}Pt clusters using CO as a probe, which will be helpful to develop new catalyst in this size range and beyond. To this end, we study the

electronic properties of the Au₁₉Pt cluster by calculating various bond lengths, binding energy (BE) and HOMO-LUMO gap of the Au₁₉Pt cluster. To study the catalytic activity of bimetallic Au₁₉Pt cluster we investigate the adsorption characteristic of CO molecule on this cluster.

4.1 Structural and Electronic Properties of Bimetallic Au₁₉Pt Clusters

All calculations presented in this chapter have been carried out by employing the same theory as described in Chapter 2 with PBE XC functional. In order to check the accuracy of our choice of basis set and XC functional we first carry out calculations for BE, bond length and bond stretching frequency of Au₂ and AuPt dimers and CO molecule. The results of these calculations are compiled in Table 4.1 along with the previously reported experimental and theoretical data. From this table, we conclude that our choice of XC functional (PBE) and the

TABLE 4.1: Calculated and experimental values of the binding energy, bond length and bond stretching frequency of Au₂, AuPt dimers and CO molecule.

System	Binding energy (eV)		Bond length (Å)		Frequency (cm ⁻¹)	
	Present work	Reported	Present work	Reported	Present work	Reported
Au ₂	2.30	2.36 ^a [2.29 (±0.02) ^b]	2.527	2.52 ^a [2.472 ^b]	175	[191] ^b
AuPt	2.62	2.55 ^a	2.479	2.47 ^a [2.60 ^c]	183	170 ^d
CO	12.13	[11.24 ^e]	1.136	1.13 ^f [1.13 ^g]	2122	2212 ^f [2143 ^g]

^{a,b,c,d,e,f,g}The values are taken from Refs. [102, 136, 142–146]. The numbers within the square brackets indicate the experimental values.

basis set (TZ2P) can provide satisfactory results for gold and gold-platinum bimetallic systems. Therefore, we make use of above mentioned XC functional and the basis sets for all calculations discussed in this chapter.

4.1.1 Properties of Tetrahedral Isomers of Au₁₉Pt Cluster

In order to get the ground state geometry we consider several structures of Au₂₀ and Au₁₉ clusters (tetrahedral, tube- and cage-like), and generate from them starting geometries of Au₁₉Pt cluster either by replacing an Au atom with a Pt atom in Au₂₀ cluster or by adding a Pt atom in Au₁₉ cluster. The details of this generation of the initial structures of the single atom doped clusters are described in Chapter 2. All these initial structures of Au₁₉Pt cluster are then optimized at GGA level (PBE XC functional) for two different values of spin multiplicity namely 2 (doublet) and 4 (quartet) to obtain the spin multiplicity of the ground state. After geometry optimization we also calculate the vibrational frequencies to check the stability of these structures. The optimized structures of tetrahedral Au₁₉Pt cluster which are obtained for doublet spin state are shown in Figure 4.1. Following the same notational convention as discussed in Chapter 2 we denote the exohedrally doped tetrahedral Au₁₉Pt clusters by Td-X, where Td stands for tetrahedral geometry and X (X = S, E, and V) refers to the location of the dopant atom Pt and X=0 represents a pure Au₂₀ cluster. The structures in Figure 4.1 are arranged in the descending

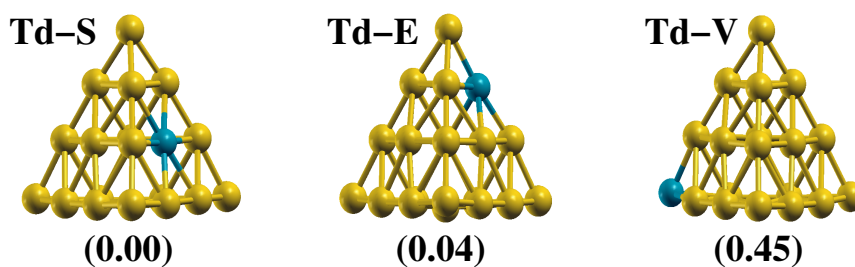


FIGURE 4.1: Optimized geometries of pyramidal bimetallic Au₁₉Pt clusters in decreasing order of BE. The values within the parentheses indicate the relative energy (in eV) of the corresponding structures. Here, the relative energy (in eV) is calculated with respect to the most stable Td-S structure.

order of their BE. It has been observed that the parent structure of Au₂₀ does not undergo any significant distortion when an Au atom is replaced by a Pt atom. This observation implies that the size of Pt (1.39 Å) atom, which is comparable to that of Au (1.44 Å) atom is geometrically suitable for doping in the tetrahedral Au₂₀ cluster. As mentioned in Chapter 2, the doping with Li (1.52 Å) atom also does not lead to any distortion in the tetrahedral structure of Au₂₀. To further study the structures of the bimetallic tetrahedral Au₁₉Pt cluster we analyze the bond

TABLE 4.2: Bond length between Pt atom and its nearest neighbor Au atom.^a

Pairs	Bond length (Å)	
	Au-Au	Au-Pt
Pt(E)-Au[edge1]	2.936	2.824
Pt(E)-Au[edge2]	2.682	2.664
Pt(E)-Au[surface]	2.815	2.697
Pt(S)-Au[vertex]	4.682	4.676
Pt(S)-Au[edge]	2.815	2.772
Pt(V)-Au[edge]	2.713	2.607

^aAu[edge1] and Au[edge2] denote Au atom in the same and different planes, respectively, with respect to the dopant Pt atom.

distances between the dopant Pt atom and its neighboring Au atoms. These bond distances are listed in Table 4.2. In the first column of this table the entry in the square bracket denotes the nearest Au atoms with which the bond distances are calculated. For the sake of comparison the corresponding Au-Au bond distances are also given in the second column of the Table 4.2. From this table we find that all the Au-Pt bond distances (2.607 - 2.824 Å) are shorter as compared to the corresponding Au-Au bond distances (2.682 - 2.936 Å) in pure Au₂₀ cluster. In particular, the Au-Pt bond distance for the case where the Pt atom makes bond with the surface Au atom reduces by 0.117 Å as compared to the corresponding Au-Au bond distance in pure Au₂₀ cluster. The reduction in bond distances is attributed to the strong interaction between Au and Pt atoms, which will be discussed further later in this chapter.

Next, we present the results for BE, HOMO-LUMO gap and magnetic moment of the optimized isomers of the bimetallic tetrahedral Au₁₉Pt cluster. First, we focus our attention on the BE of these clusters which characterises the thermodynamic stability of the clusters and it is calculated by employing the equation given below,

$$BE = -\{E(\text{Au}_{19}\text{Pt}) - 19E(\text{Au}) - E(\text{Pt})\} \quad (4.1)$$

where $E(\text{Au}_{19}\text{Pt})$, $E(\text{Au})$ and, $E(\text{Pt})$ are the energies of Au₁₉Pt cluster, Au and, Pt atoms respectively. The calculated binding energies of Au₁₉Pt clusters have been tabulated in the second

TABLE 4.3: Binding energy, HOMO-LUMO gap, and magnetic moment of the pure (Td-0) and bimetallic tetrahedral Au₁₉Pt cluster.

System	Binding energy (eV)	HOMO-LUMO gap (eV)		Magnetic moment(μ_B)
		Spin up	Spin down	
Td-0	46.81	1.771	-	-
Td-S	48.10	1.430	0.128	1
Td-E	48.06	1.546	0.037	1
Td-V	47.65	1.782	0.089	1

column of the Table 4.3. From this table we find that binding energies of all bimetallic Au₁₉Pt clusters (47.65 - 48.10 eV) are greater than that of pure Au₂₀ cluster (46.81 eV). We thus infer that the doped Au₁₉Pt clusters are energetically more favorable as compared to the pure Au₂₀ cluster. In particular, the BE of Td-S structure is the highest among all the isomers of Au₁₉Pt clusters which are considered in this present study and it is 1.29 eV higher than that of pure Au₂₀ cluster. The second most stable isomer of Au₁₉Pt cluster is Td-E and its BE is just 0.04 eV lower than the most stable Td-S isomer. Note that the relative stabilities observed here are in good agreement with the previous study by Leppert *et al.* [18], where the authors have investigated the core-shell growth pattern of 20 and 40-atoms Au-Pt bimetallic clusters. Thus we conclude that the dopant Pt atom favors almost equally both the surface and edge positions of the tetrahedral Au₂₀ cluster. We wish to point out here that the enhancement in the BE due to Pt doping is more than twice that of due to Li doping (0.58 eV) with respect to pure 20-atom gold cluster [19]. This drastic difference in the BE of Au₁₉Pt in comparison to the Au₁₉Li may be attributed to the fact that interaction of Au atom with Pt is more of a covalent nature whereas with Li atom it is more ionic in character [19, 20].

Having discussed the thermodynamic stability of the isomers of the bimetallic Au₁₉Pt clusters, we now focus our attention to the chemical stability of these isomers, which is quantified in terms of HOMO-LUMO gap. For the open shell cluster we can define HOMO-LUMO gap separately for spin-up ($E_{gap}^{spin-up}$) and spin-down ($E_{gap}^{spin-down}$) electrons as,

$$E_{gap}^{spin-up} = -\{HOMO^{spin-up} - LUMO^{spin-up}\} \quad (4.2)$$

$$E_{gap}^{spin-down} = -\{HOMO^{spin-down} - LUMO^{spin-down}\} \quad (4.3)$$

where $HOMO^{spin-up}$ ($HOMO^{spin-down}$), and $LUMO^{spin-up}$ ($LUMO^{spin-down}$) are Kohn-Sham eigenvalues for HOMO and LUMO, respectively, for the spin-up (spin-down) electrons. The HOMO-LUMO gaps for the spin-up and spin-down electrons corresponding to the tetrahedral $Au_{19}Pt$ cluster are listed in the third and fourth columns of Table 4.3 respectively. From this table it is observed that $E_{gap}^{spin-up}$ is always much higher than that of $E_{gap}^{spin-down}$. This indicates that the transfer of electron through the spin-down channel is much easier than the spin-up channel. In Figure 4.2 we display the molecular orbital corresponding to HOMO of spin down electrons of the bimetallic tetrahedral $Au_{19}Pt$ cluster. From this figure clearly we see that the HOMO of

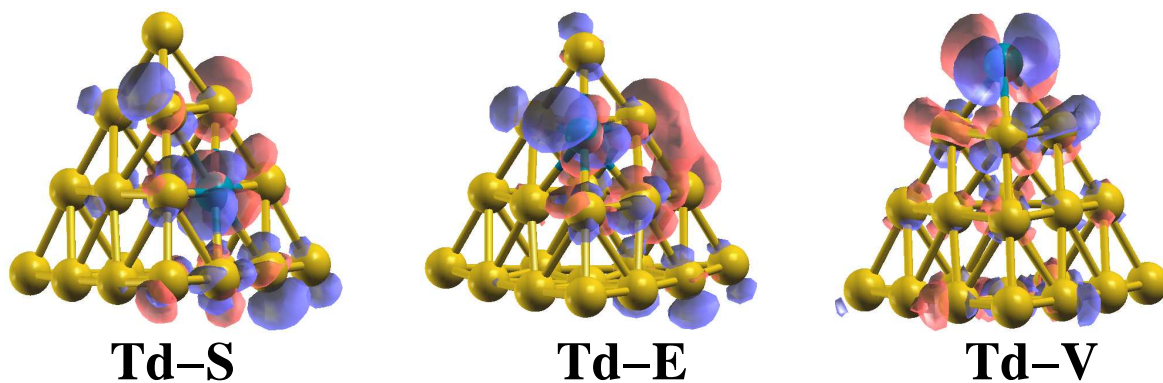


FIGURE 4.2: Representation of HOMO of spin down electrons corresponding to the tetrahedral $Au_{19}Pt$ clusters.

the bimetallic $Au_{19}Pt$ clusters are localized around the dopant Pt atom. The gold atoms in the surroundings of the dopant Pt atom also contribute to the HOMO of the clusters. This indicates that there is a strong possibility of electron exchange from the Pt sites as well as Au sites which are neighborhood of Pt, during the chemical reaction. To explore this possibility of modulation of reactivity of the Pt doped clusters we study adsorption of CO on all the isomers of the bimetallic tetrahedral $Au_{19}Pt$ cluster and results are presented in Section 4.2.

Due to unfilled d-orbital in Pt atom it is expected that the Pt doped gold cluster to have finite magnetic moment. In order to check this we calculate the magnetic moments of these clusters,

which are listed in fifth column of the Table 4.3. From this table it is clear that the substitution of Pt atom in Au_{20} cluster gives rise to the magnetic moment of $1 \mu_B$ in the doped clusters. For more insight into the origin of this magnetic moment we plot the magnetization density of the doped clusters, which is shown in Figure 4.3. This figure shows that the magnetic moments

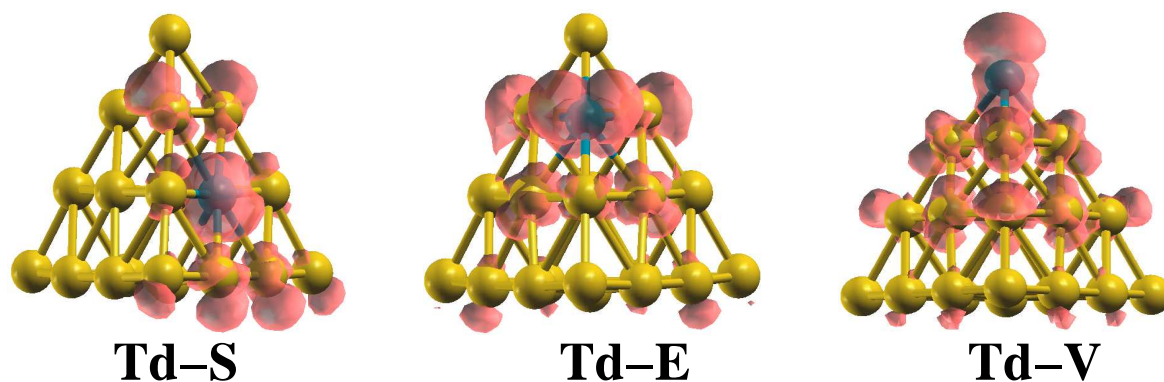


FIGURE 4.3: Magnetization density (spin-up charge density - spin-down charge density) plot of Td-S, Td-E and Td-V clusters.

of all the isomers of Pt doped gold cluster are localized around dopant Pt atom. The value of magnetic moments for Pt atom in Td-S, Td-E and Td-V clusters are found to be 0.46, 0.51, and $0.36\mu_B$ respectively, while for bare a Pt atom it is $2.0 \mu_B$. Thus we infer that the magnetic moment of Pt atom is quenched when it is doped in the gold cluster. Moreover, the total magnetic moments of the bimetallic Au_{19}Pt clusters are not solely due to the dopant Pt atom rather, it is a collective effect which comes from the different Au atoms and Pt atom.

In order to rationalize the existence of strong interaction between Au and Pt atoms in Au_{19}Pt clusters we plot partial density of states (PDOS) of the s- and d-orbitals of Pt and Au atoms of Au_{19}Pt cluster. The PDOSs are displayed in Figure 4.4 (a), (b) and (c) corresponding to Td-S, Td-E and Td-V clusters respectively. This plot clearly shows the presence of hybridization between the s- and d-orbitals of Au and Pt atoms in the energy range 0 to -5 eV. It is this hybridization which leads to a strong bonding between the dopant Pt atom and the host Au atoms. For the surface- and edge-doped Au_{19}Pt clusters the hybridization occurs in a wider range as compared to that observed in vertex-doped Au_{19}Pt cluster. As a result Td-S and Td-E clusters are energetically more stable than Td-V cluster. Moreover, for the case where the Pt atom is doped at the vertex position of the tetrahedral Au_{20} cluster the unfilled d-orbital

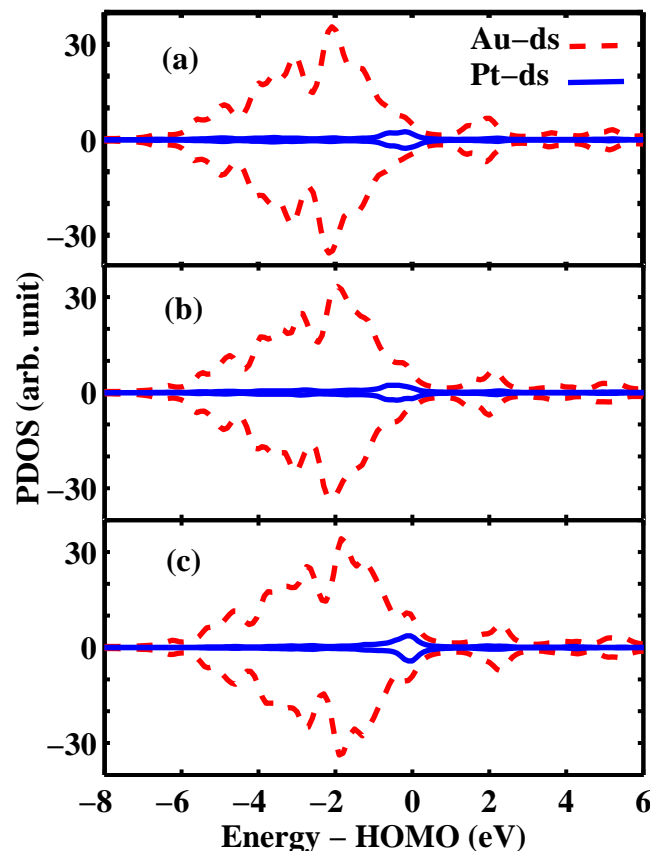


FIGURE 4.4: PDOS for s- and d-orbitals of Au (dashed lines) and Pt (solid lines) atoms in Td-S (a), Td-E (b) and Td-V (c) clusters.

of Pt atom is almost localized at the HOMO of the cluster. Whereas for surface- and edge-doped Au_{19}Pt clusters the unfilled d-orbital of Pt atom is distributed around the HOMO. This indicates that the vertex site occupied by Pt atom in the isomers of Au_{19}Pt cluster may show maximum chemical reactivity which is investigated in the next section (Section 4.2) by studying the adsorption of CO molecule on these clusters.

4.1.2 Properties of Cage-like Isomers of Au_{19}Pt Cluster

In order to make our search for the minimum energy structure of Au_{19}Pt cluster we now focus our attention on the non-tetrahedral isomers of this cluster. To this end, like Li case here also

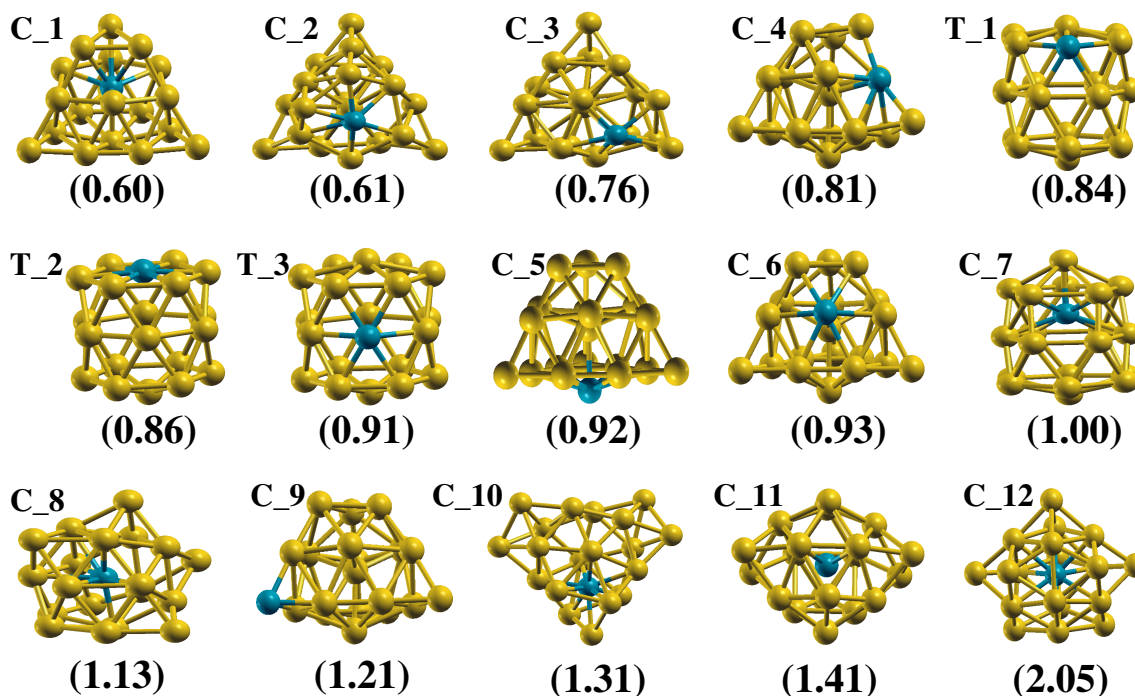


FIGURE 4.5: Optimized geometries of cage and tube like Au_{19}Pt clusters in the decreasing order of BE. The values within the parentheses indicate the relative energy (in eV) of the corresponding structures. Here, the relative energy (in eV) is calculated with respect to the most stable Td-S structure.

we consider seven cage-like isomers of Au_{19}Pt cluster where the dopant Pt atom is placed at the endohedral as well as exohedral positions of the cage. Along with these cage-like isomers of Au_{19}Pt we also consider a tube-like isomer of Au_{20} and replace an Au atom with a Pt atom from the three non-equivalent positions of the tube to generate three tube-like isomers of Au_{19}Pt cluster. The cage-like isomers are denoted by C_i , where $i = 1 - 12$ and the tube-like isomers are represented by T_i , where $i = 1 - 3$. All these isomers of Au_{19}Pt cluster are the optimized at the similar level of theory as employed for obtaining optimized tetrahedral isomers. Selected optimized geometries of the cage-like and tube-like isomers of Au_{19}Pt cluster are shown in Figure 4.5. In this figure the values within the parentheses below each structure indicate the relative energies of the cage- and tube-like isomers of Au_{19}Pt cluster with respect to the most stable Td-S cluster. In order to make our search more extensive for the most stable isomer of Au_{19}Pt cluster, we carry out a calculation of relative energies and binding energies of all the isomers with different XC functional (PBE, PW91 and BP86) as well as for two different spin states (doublet and quartet). These results are compiled in Table 4.4. From this table we observe

TABLE 4.4: Binding energies of the bimetallic Au₁₉Pt clusters with different XC functionals and spin states.

System	Binding energy (in eV) with different spin states			Relative energy (in eV) with different XC functionals ^a		
	Doublet	Quartet ^b	E_{d-q}^{\dagger}	PBE	PW91	BP86
Td-S	48.10	46.70(46.79)	1.41	0.00	0.00	0.00
Td-E	48.06	46.60(46.73)	1.47	0.04	0.02	0.01
Td-V	47.65	45.87(46.01)	1.78	0.45	0.43	0.41
C_1	47.50	46.23(46.65)	1.27	0.60	0.60	0.65
C_2	47.49	46.22(46.44)	1.28	0.61	0.61	0.66
C_3	47.34	45.997(46.190)	1.34	0.76	0.75	0.80
C_4	47.30	46.05(46.22)	1.24	0.81	0.80	0.85
T_1	47.27	46.37 ^c	0.90	0.84	0.78	0.72
T_2	47.24	46.27 ^c	0.98	0.86	0.80	0.76
T_3	47.20	46.13 ^c	1.06	0.91	0.85	0.79
C_5	47.19	45.97(46.09)	1.22	0.92	0.91	0.96
C_6	47.18	45.97(46.12)	1.21	0.93	0.92	0.97
C_7	47.11	46.11(46.48)	1.00	1.00	0.98	1.03
C_8	46.97	46.04(46.34)	0.94	1.13	1.12	1.19
C_9	46.90	45.44(45.71)	1.46	1.21	1.20	1.24
C_10	46.79	46.05(46.36)	0.74	1.31	1.30	1.30
C_11	46.68	46.37(46.51)	0.31	1.42	1.41	1.51
C_12	46.05	45.65(46.22)	0.41	2.05	2.04	2.10

^aThe relative energy (in eV) is calculated with respect to the most stable Td-S structure.

^bThe values indicates the binding energies calculated at the doublet spin state geometries and values within the parentheses indicate the binding energies calculated from optimized geometries with quartet spin state.

[†]The energy difference between doublet and quartet spin states.

^cThese geometries do not converge with quartet spin state.

that binding energies of all the doped Au₁₉Pt clusters with doublet spin state are around 1 eV higher as compared to those with the quartet spin state. This indicates that for Au₁₉Pt clusters the higher spin multiplicity other than doublet is not favorable. Furthermore, from the last three columns of Table 4.4 we observe that for all the three XC functional Td-S is the most stable isomer of Au₁₉Pt cluster. It is also very clear that the relative stabilities of all the isomers of Au₁₉Pt cluster are almost same for different XC functionals. Moreover, from this table we can see that all the tetrahedral isomers of Au₁₉Pt cluster are more stable than any other non-tetrahedral isomers of Au₁₉Pt cluster. For example, the BE of tetrahedral isomer Td-S is 0.6

eV higher than the most stable endohedrally doped cage-like isomer C_1. From these results we infer that the cage-like core-shell segregated structure, which is often observed for Au-Pt bimetallic clusters [18, 135, 141, 147], is not observed for the single Pt doped 20-atoms Au-Pt bimetallic cluster. Due to very high symmetry (T_d) of Au_{20} cluster and the comparable sizes of Au and Pt atoms this cluster can be doped with Pt atom without causing appreciable distortion of the pyramidal structure. Note that earlier Leppert *et al.* [18] studied the core-shell growth pattern for 20 and 40-atoms Au-Pt clusters. Similar to our result these authors also found that a tetrahedral structure of a single Pt atom doped at surface location as the most stable structures among all the structures of $Au_{19}Pt$ cluster considered in their paper. Moreover, these authors also noted the absence of definite signature of formation of core-shell system in case of singly doped $Au_{19}Pt$ cluster. Nevertheless, they have considered only one cage like structure for the $Au_{19}Pt$ cluster. On the other hand, in the present work we consider 12 cage-like and 3 tube-like structures, in addition to all the tetrahedral structures. Due to the large energy difference between tetrahedral and other isomers of $Au_{19}Pt$ cluster we consider only the former one to investigate the interaction of CO molecule with this cluster.

4.2 Chemical Properties of Bimetallic $Au_{19}Pt$ Clusters

To study the chemical reactivity of $Au_{19}Pt$ cluster we systematically investigate the adsorption of CO molecule on various isomers of this cluster. As mentioned before for this purpose we consider only the tetrahedral isomers of $Au_{19}Pt$ cluster. To get the initial geometries for the cluster-CO complex we place a single CO molecule on various non-equivalent positions of the three bimetallic tetrahedral isomers namely Td-S, Td-E and Td-V. Note here that a CO molecule can interact with Au/Pt atom in the cluster either via C atom (CO mode) or via O atom (OC mode). Like the case of Li doping as described in the previous chapter here also we find that CO molecule prefers to interact with Pt/Au atom in CO mode. So we consider this mode of interaction and find that there are 27 different possible configurations for CO to interact with the isomers of $Au_{19}Pt$ cluster. The optimized geometries of tetrahedral $Au_{19}Pt$ -CO complexes are

shown in Figure 4.6. Following the notations adopted for the case of Li doping, we denote the various tetrahedral isomers of cluster-CO complex by the symbol Td-X-Y_j, where Y refers to the site of CO adsorption like S, E and V and the index j, which takes integral values indicates different Y sites in the tetrahedral geometry. In the following we focus our attention on the three most stable cluster-CO complexes namely Td-S-S1, Td-E-E1 and Td-V-V1 where CO molecule is adsorbed on the surface-, edge-, and vertex-Pt atoms respectively. It is observed that the binding energies of these cluster-CO complexes change drastically after the adsorption of a CO molecule. We find that the most stable Td-S cluster becomes the least stable among these three structures after adsorbing a CO molecule on the surface Pt atom. On the other hand, Td-V-V1 is 0.15 eV more stable as compared to Td-S-S1 configuration, while, parent Td-V cluster is 0.45 eV less stable than Td-S cluster. The configuration Td-E-E1 turns out to be the most stable one with a energy difference of 0.34 eV as compared to the least stable Td-S-S1 complex. This change in the energy ordering of the cluster-CO complexes occurs due to the strong interaction of CO molecule with the vertex and edge Pt atoms as compared to that with surface Pt atom. The results pertaining to the interaction of CO with the isomers of Au₁₉Pt cluster is discussed below in this section. From Figure 4.6 we can see that the adsorption of CO molecule results in minimal changes to the geometries of the parent structures of the doped clusters. However, we observe that due to the adsorption of CO molecule the surface Pt/Au atom is slightly pulled out from the cluster. Interestingly, we observe that Pt-C-O angle in all the three cases (see Figure 4.6) lies in the range 177.1 - 179.9°. This indicates that the cluster repels O atom of CO molecule and try to keep it away from cluster which may lead to the weakening of C-O bond and implication of this result is discussed below.

To further analyze the structure of cluster-CO complex we examine various bond lengths which are compiled in Table 4.5. From this table we observe that the Au-C distance ranges from 1.986Å - 2.020Å for the cases where the CO molecule is adsorbed on the Au atom of a pure Au₂₀ cluster. Whereas, for CO adsorption on Au₁₉Pt cluster the Pt-C distance reduces to the range 1.841Å- 1.852Å. This result clearly indicates that the interaction between CO molecule and the Pt atom in the doped cluster is significantly stronger as compared to that between CO

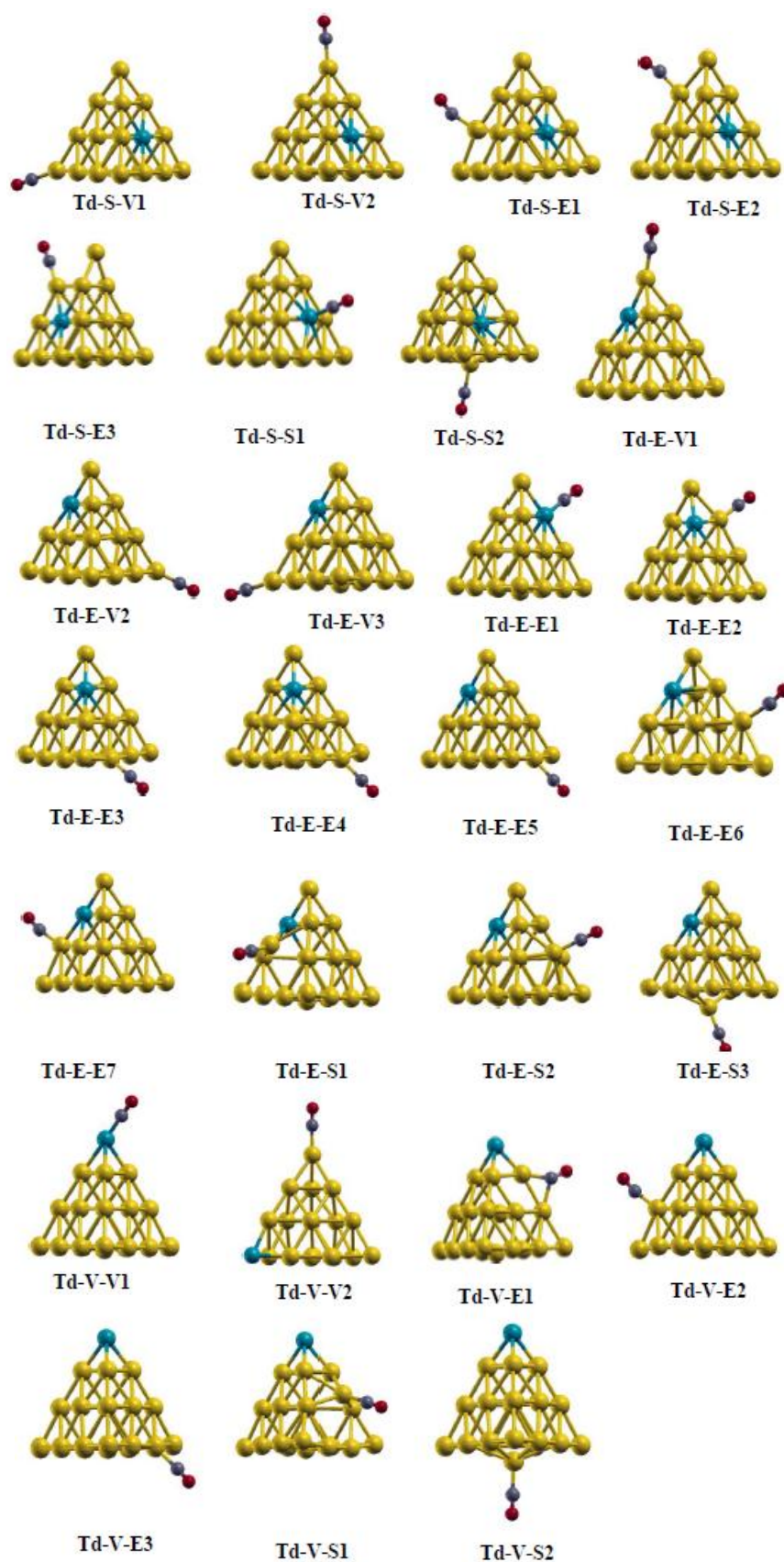
FIGURE 4.6: Optimized geometries of pyramidal $\text{Au}_{19}\text{Pt-CO}$ complex.

TABLE 4.5: Bond length and bond stretching frequency of the cluster-CO complexes.

System	Bond length (Å)		Frequency (cm ⁻¹)	
	metal-C ^a (Å)	C-O (Å)	$\nu_{metal-C}$	ν_{C-O}
Td-0-S	1.986	1.144	335	2056
Td-0-E	2.020	1.147	319	2027
Td-0-V	1.977	1.144	355	2063
Td-S-S1	1.841	1.156	507	2018
Td-E-E1	1.852	1.158	501	2001
Td-V-V1	1.850	1.157	504	2016

^ametal-C indicates either Au-C or Pt-C distances.

molecule and Au atom in pure cluster. Moreover, we note that the decrease in Pt-C bond length is also accompanied with an increase (~ 0.02 Å) in C-O bond length as compared to that of the free CO molecule (1.136 Å) when a CO molecule is adsorbed on the Pt atom. A maximum increase by 0.022 Å in C-O bond length is observed for the case where CO molecule gets adsorbed on Pt atom of Td-E cluster. On the other hand, in the previous chapter we have shown that a small increase (~ 0.01 Å) in C-O bond length occurs when CO molecule is allowed to get absorbed on bimetallic Au₁₉Li and on pure Au₂₀ clusters. Thus, from these C-O bond length data it is very clear that the activation of C-O bond is much higher in the present case of CO adsorption on bimetallic Au₁₉Pt cluster in comparison to our previous work [22]. This indicates that the bimetallic Au₁₉Pt cluster has higher potential to be a good catalytic agent in CO oxidation reaction. To get more insight into the effect of cluster-CO interaction on the metal-C and C-O bond lengths we also calculate their stretching frequencies which are listed in fourth and fifth columns of Table 4.5 respectively. These results show that the C-O stretching frequency suffers a red-shift when CO molecule is adsorbed on both pure (Au₂₀-CO) and Pt doped (Au₁₉Pt-CO) cluster. However, the magnitude of the red-shift is significantly more when the CO molecule is adsorbed on the Pt sites in the Au₁₉Pt clusters. For this case the red-shift in the C-O stretching frequency lies in the range 104 - 121 cm⁻¹. These results indicate that the adsorption of CO on Pt atom significantly changes the electronic structure of CO molecule. This change in electronic structure of CO molecule is further elucidated by the Mulliken charge analysis and the results of this analysis are discussed below. First, we evaluate the charge on

Pt atom on which the CO molecule has been adsorbed and also on the adsorbed CO molecule and these results are compiled in Table 4.6. From this table it can be clearly seen that the

TABLE 4.6: Mulliken Charge on Pt Site and the Total Charge on the Adsorbed CO Molecule.

System	Mulliken charge analysis			
	Charge on adsorption sites		Charge transfer	Total charge on CO
	Before CO adsorption	After CO adsorption		
Td-S-S1	-0.0306	0.0937	0.1243	-0.0252
Td-E-E1	-0.1429	-0.0091	0.1338	-0.0757
Td-V-V1	-0.1893	-0.0513	0.1380	-0.0695

Pt atom loses a fraction of its charge and this is transferred partly to the neighboring Au atoms and partly (~50%) to the adsorbed CO molecule. We observe that the amount of charge received by CO molecule depends on the location (S, E, and V) where it gets adsorbed. For example, the highest charge (-0.0757) transfer takes place when CO molecule gets adsorbed on Pt atom located at the edge site of Td-E cluster. This excess charge is transferred to empty $2\pi^*$ anti-bonding orbital of CO molecule, which in turn leads to the weakening of the C-O bond. Consequently, we observe an increase in C-O bond length as well as a red-shift in the C-O stretching frequency which are discussed earlier. Moreover, we find that the maximum increase in C-O bond length is observed in the case where CO molecule is adsorbed on Pt atom located at edge site, which is consistent with the highest charge transfer corresponding to this adsorption. Furthermore, in our earlier study [22] on adsorption of CO on Au_{19}Li cluster we observed that the maximum charge transfer from the cluster to CO is -0.0305 which is almost half of that which is observed in our present study (-0.0757). As a result, we find that the increase in C-O bond length is almost double for Au_{19}Pt cluster (0.022 Å) as compared to that of Au_{19}Li cluster [22] (0.011 Å). This also clearly indicates that the charge transfer from the cluster to the adsorbed CO has an important role in the increase of C-O bond length and which in turn leads to the activation of C-O bond.

To quantify the strength of adsorption of CO molecule on Au₁₉Pt cluster we calculate the adsorption energy (E_{ad}) using the following expression,

$$E_{ad} = -\{E(\text{cluster} - \text{CO}) - E(\text{cluster}) - E(\text{CO})\} \quad (4.4)$$

where $E(\text{cluster} - \text{CO})$, $E(\text{cluster})$, $E(\text{CO})$ are the energies of the cluster-CO complex, pure/-doped gold cluster on which CO is adsorbed and a bare CO molecule respectively. The higher value of E_{ad} indicates the stronger adsorption of CO molecule on the cluster. We observe that the adsorption energy of a CO molecule at the Pt site, irrespective of the position in the cluster, is much higher as compared to that on the Au sites in the pure as well as doped clusters. This is in contrast to our earlier report [22] where we observed that the Li sites in Au₁₉Li clusters show least propensity towards CO adsorption. The values of E_{ad} for adsorption of CO molecule at various locations of the tetrahedral Au₁₉Pt cluster are reported in Table 4.7. From this table we

TABLE 4.7: CO Adsorption energy (in eV) for the pure and the bimetallic Au₁₉Pt clusters.

Adsorption site	Pure cluster	Bimetallic cluster	
	Adsorption on Au atom	Adsorption on Pt atom	Adsorption on Au atom ^a
Surface	0.37	1.68	0.39 - 0.56
Edge	0.46	2.06	0.44 - 0.89
Vertex	0.82	2.28	0.81 - 1.03

^aThe adsorption energy is given in a range for Au atom which possesses similar position in different tetrahedral Au₁₉Pt clusters.

observe that the CO adsorption energy increases by more than 1.3 eV when the CO molecule gets adsorbed on Pt site in Au₁₉Pt cluster as compared to the adsorption on corresponding Au atoms in pure Au₂₀ cluster. Furthermore, we find that among all the three locations (E, S, and V) of Pt atom in Au₁₉Pt cluster the vertex site is the most favorable site for the adsorption of a CO molecule with $E_{ad} = 2.28$ eV which is 1.46 eV greater than the adsorption energy of CO molecule on vertex Au atom of pure Au₂₀ cluster. Thus it is very clear that a CO molecule

exhibits higher propensity to get adsorbed on vertex sites which has minimum number of nearest neighbors (lowest co-ordination site) [132]. Moreover, we note here that HOMO of Td-V is highly localised near the Pt atom (see Figure 4.2) and hence it can interact strongly with CO molecule yielding very high adsorption energy. Thus we conclude from the above results that combined effect of low coordinated site for Pt atom and localization of HOMO at Pt atom results in significant enhancement of the adsorption energy. On the other hand, the adsorption of CO on the surface- and edge-Pt atoms is also significantly strong (>1.3 eV) as compared to that on the corresponding sites in the pure Au_{20} cluster. But, the adsorption energy for these two cases is slightly smaller (~ 0.6 eV) as compared to that of Td-V-V1 complex where CO is adsorbed on vertex-Pt atom. This lowering in adsorption energy may be attributed to the higher (more than 6) coordination number of the surface- and edge-sites. In Table 4.7 (column 4) we also present the results for the adsorption energy when CO molecule is adsorbed on various Au sites in Au_{19}Pt cluster. These results clearly indicate that the presence of Pt atom generally enhances the adsorption energy in comparison to the cases of corresponding adsorption of CO on pure Au_{20} cluster. The maximum enhancement in the CO adsorption energy on Au sites in the bimetallic Au_{19}Pt cluster is observed for Au atoms which are located nearest to the dopant Pt atom. This increase in adsorption energy can be attributed to the effect of localization of HOMO at Pt and the adjoining Au atoms (see Figure 4.2). Thus our study clearly demonstrates that not only Pt site but also adjoining Au sites in Au_{19}Pt cluster favor adsorption of CO molecule thereby providing a more number of active sites as compared to the pure Au_{20} cluster. We note here that the bimetallic cluster Td-V is slightly less stable (see Figure 4.1) as compared to the most stable Td-S structure but it is more stable than pure Au_{20} cluster. Hence, the production of Td-V cluster along with other isomers of Au_{19}Pt cluster may be possible in the experiments. We note here that the less favorable isomers can be stabilized by depositing on a suitable solid surface [17]. It is then quite clear that the energy ordering of the CO adsorbed cluster complexes will be different as compared to that of the free clusters, and it might be possible to observe Td-V experimentally.

To get further insight into the interaction of CO and the cluster we analyze PDOS (Figure 4.7)

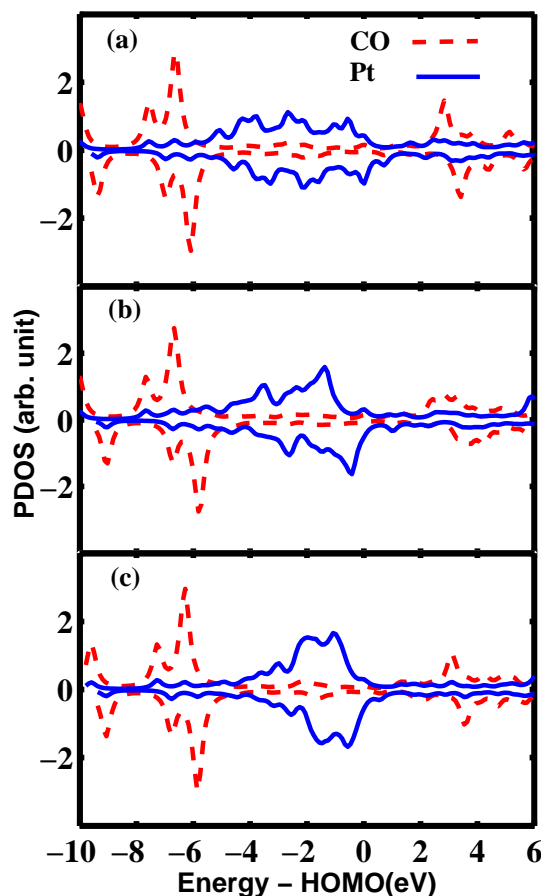


FIGURE 4.7: PDOS of s- and p-orbitals of CO (dashed line) and s- and d-orbitals of Pt atom (solid line) in (a) Td-S-S1, (b) Td-E-E1 and (c) Td-V-V1 complexes.

corresponding to s- and p-orbitals of CO and s- and d-orbitals of Pt atom in Td-S-S1, TD-E-E1 and Td-V-V1 isomers of cluster-CO complexes. From Figure 4.7 we can see that the interaction between CO and Pt atom in all these cluster-CO complexes occurs in a wide range below the HOMO. In particular, the interaction between sp orbitals of CO and sd orbitals of Pt is very strong near -2 and -6 eV. This leads to the strong adsorption of CO on the bimetallic Au₁₉Pt clusters and hence these clusters may exhibit better catalytic activity. Here, we wish to mention that the catalytic activity of Au-Pt bimetallic cluster may change towards betterment with the increasing content of Pt [18, 141]. This is because of the increase in DOS at the HOMO due to the increasing content of Pt. Similarly, in the present study we also observe that the population of d-orbital of Pt atom near the HOMO (see Figure 4.4 where the solid curve is dominated by the d-orbital of Pt) leads to the enhancement of CO adsorption energy which is generally

considered as an indicator for a better catalytic activity. Note that for Au_{19}Pt cluster the Pt site is directly exposed to the external molecules whereas for cage-like core-shell segregated $\text{Au}_{\text{shell}}\text{-Pt}_{\text{core}}$ clusters the Pt atoms is not directly available to react with the external molecules.

4.3 Conclusions

In summary, we study the structural and chemical properties of bimetallic Au_{19}Pt cluster. We find that Au_{19}Pt cluster also prefers the tetrahedral geometry as observed for the pure Au_{20} cluster as well as for Li doped Au_{19}Li cluster. The binding energies of all the three possible tetrahedral isomers (Td-S, Td-E, and Td-V) of Au_{19}Pt cluster are found to be higher than that of pure tetrahedral Au_{20} and Li doped Au_{19}Li clusters. In particular, BE of the isomers with Pt atom doped at one of the four surfaces or one of the twelve edges of the tetrahedron are significantly higher (around 1.3 eV) as compared to that of the pure Au_{20} cluster. The high stability of the bimetallic Au_{19}Pt cluster can be attributed to the strong interaction between Au and Pt atoms, which is caused by the hybridization of s- and d-orbitals of dopant Pt and the host Au atoms lying in the energy range 0 to -5 eV. Moreover, PDOS analysis shows that the unfilled d-orbitals of the doped clusters are localized near the HOMO level making them good electron donors, which results in higher chemical activities of these doped clusters. We verify this by investigating the chemical reactivity of the doped clusters using CO adsorption as a probe. We find that the Pt sites in Au_{19}Pt clusters are much more reactive than Au sites. In particular, the low coordinated vertex-Pt atom shows maximum reactivity ($E_{ad} = 2.28$ eV) towards CO adsorption. This happens due to the fact that for the case of Pt atom located at the vertex site its unfilled d-orbital is more localized at the HOMO in comparison to the cases where Pt atoms occupy the surface or edge sites of Au_{20} cluster. Moreover, we observe that due to the charge transfer from the cluster to the CO molecule C-O bond length increases around 0.02 Å which causes a substantial amount of red shift (104-121 cm^{-1}) in C-O stretching frequency. In particular, the increase in the C-O bond length and its stretching frequency are found to be maximum (0.022 Å and 121 cm^{-1}) for CO molecule adsorbed on edge-Pt atom. Moreover,

the adsorption energy of this edge-doped Au_{19}Pt -CO complex (Td-E-E1) is also significantly higher than the corresponding Au_{20} -CO complex. Hence, we expect that the edge-doped Au_{19}Pt cluster (Td-E) will be a good catalytic agent in the CO oxidation reaction. Moreover, we conclude that all the Pt doped tetrahedral Au_{19}Pt clusters are more suitable for catalysts in the CO oxidation reaction as compared to that of pure Au_{20} cluster. Overall, the comparison between chemical properties of the Au_{19}Pt and Au_{19}Li indicates that the former has higher catalytic activity than that of the later one. Hence, to check the catalytic activity of the Au_{19}Pt cluster in the next chapter we carry out a systematic investigation on the catalytic activity of Au_{19}Pt cluster for the oxidation reaction of the CO molecule.

Chapter 5

Catalytic Activity of Pt Doped Gold Nano-Clusters

This chapter is devoted to the study of the oxidation reaction of CO molecule on Au₁₉Pt cluster. In the previous chapter we have discussed the adsorption behavior of CO on Au₁₉Pt cluster which is a part of the above mentioned oxidation reaction. It was shown that the adsorption energy of CO on this cluster is more than 1 eV higher than that on pure Au₂₀ cluster and the C-O bond is activated by around 0.02 Å. In accordance with the general belief that both CO and O₂ activations are important factors in the process of oxidation of CO, we expect that Au₁₉Pt cluster may serve as good catalytic agent for this process [49, 136, 148–152]. In the present chapter, we explore this possibility by carrying out a systematic study on the catalytic activity of Au₁₉Pt cluster for the CO oxidation reaction. To this end, in addition to CO adsorption we further investigate adsorption characteristics of both O₂ and CO+O₂ on this bimetallic cluster and calculate the corresponding reaction barriers. Moreover, we also study the relationship between the extent of O₂ activation and the CO oxidation process to search for the optimal activity as expected on the basis of the Sabatier principle [153]. For this purpose, we choose two structurally similar and energetically almost degenerate isomers of the Au₁₉Pt cluster and investigate their catalytic activities for the oxidation of CO.

5.1 Computational Details

All the results presented in this chapter are calculated at the same level of theory as used in previous chapter (Chapters 4). The transition states for the oxidation reaction of CO are obtained using ‘climbing image nudged elastic band’ (CI-NEB) [100] method as implemented in ADF package. For completeness we also carry out geometry optimization of the states obtained through CI-NEB method by employing the transition state optimization procedure available in ADF package. The transition state is identified as the structure having a vibrational mode with highly negative frequency.

5.2 Isomers of Au₁₉Pt Cluster

In the previous chapter, we found that the Td-S and Td-E isomers are energetically very close and more stable than the pure Au₂₀ cluster, while Td-V is less stable by around 0.4 eV as compared to both Td-S and Td-E. Therefore, we choose to study the catalytic activity of Td-S and Td-E isomers of Au₁₉Pt cluster in the oxidation reaction of CO. Since the adsorption of O₂ and its bond activation [49, 148, 149, 151] is considered to be a key step for the oxidation reaction of CO, we start our investigation with the adsorption of O₂ on Td-E and Td-S isomers of Au₁₉Pt cluster. For the sake of completeness and comparison we also consider Td-V isomer and investigate the adsorption of O₂ on it.

5.3 Adsorption of O₂ on Au₁₉Pt Clusters

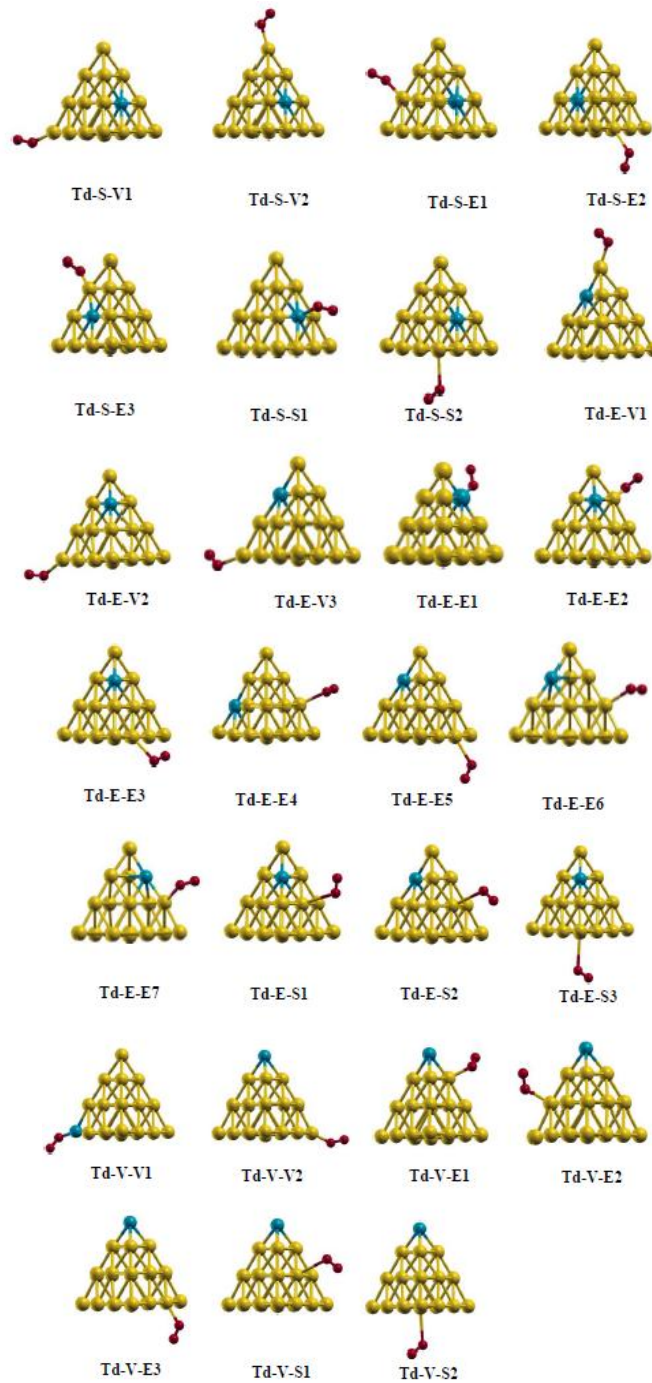
In order to investigate the O₂ adsorption behavior of Au₁₉Pt cluster first we allow one O₂ molecule to get adsorbed at different non-equivalent positions within this cluster which results in 27 different possible initial geometries of Au₁₉Pt-O₂ complexes. All these geometries are then locally optimized at GGA level with PBE XC functional. Note that, here all the geometries are optimized considering two possible spin states namely doublet and quartet. We

find that the ground state spin configuration is doublet and all the results presented here have been obtained with the doublet spin state of the $\text{Au}_{19}\text{Pt-O}_2$ complexes. Following the notation employed in Chapter 4 we denote the cluster- O_2 complexes by the symbol Td-X-Y_j, where Td denotes tetrahedral geometry, X and Y indicate the positions (edge (E), surface (S) and vertex (V)) of Pt and O_2 respectively, and j is an integer which denotes the different Y site in the tetrahedral geometry. All the optimized geometries of the $\text{Au}_{19}\text{Pt-O}_2$ complexes with doublet spin state are shown in Figure 5.1. From this figure we observe that like CO as discussed in Chapter 4, the adsorption of O_2 also does not lead to any significant distortion of the parent structure of the Au_{19}Pt cluster. It implies that the bimetallic Au_{19}Pt cluster can accommodate both CO and O_2 without much deformation in its structural property, which is a positive feature as far as prediction of catalytic activity is concerned. Furthermore, looking at the geometries of the $\text{Au}_{19}\text{Pt-O}_2$ complexes (Figure 5.1) we observe that the Pt-O-O angle is close to 116° , whereas in the case of CO adsorption the corresponding angle is close to 180° . It indicates that adsorption of CO and O_2 on Au_{19}Pt cluster exhibits distinctly different characteristics. For further analysis of the adsorbed O_2 molecule we calculate the O-O bond length, corresponding stretching frequency, and the Mulliken charges on it. These results are compiled in Table 5.1. From this table we find that the O-O bond length of the adsorbed O_2 molecule increases by

TABLE 5.1: O-O bond lengths ($R_{\text{O-O}}$), corresponding stretching frequencies ($\nu_{\text{O-O}}$) and the atomic charges (Q_{O_2}) on the adsorbed O_2 for the selected tetrahedral $\text{Au}_{19}\text{Pt-O}_2$ complexes along with the corresponding values for a free O_2 molecule

System	$R_{\text{O-O}}$ (Å)	$\nu_{\text{O-O}}$ (cm^{-1})	Q_{O_2}
Free O_2	1.222	1538	0.0000
Td-V-V1	1.280	1204	0.2889
Td-E-E1	1.281	1188	0.2821
Td-S-S1	1.267	1234	0.2123
Td-E-V1	1.263	1272	0.2002
Td-S-E3	1.259	1286	0.1782
Td-V-E1	1.256	1286	0.1684

more than 0.04 Å as compared to that of a free O_2 molecule. The increase in O-O bond length is also observed when the O_2 is adsorbed on the Au sites in the neighborhood of the Pt atom. This increase in O-O bond length is attributed to the charge transfer from the cluster to the

FIGURE 5.1: Optimized geometries of the $\text{Au}_{19}\text{Pt-O}_2$ complexes

$2\pi^*$ anti-bonding state of O_2 . Here, we find that maximum charge transfer occurs when the O_2 molecule is adsorbed on the vertex-Pt atom. However, for CO adsorption the maximum charge transfer was observed for the case where CO is adsorbed on the edge-Pt atom. Overall, our studies indicate that the charge transfer to the adsorbed species is responsible for the increase

in their bond lengths. Such lengthening of the O-O and C-O bond lengths indicates the activation of the corresponding bond. To further quantify the activation of the O-O bond we calculate the corresponding bond stretching frequencies which are listed in the third column of Table 5.1. These results show significant amount of red shift (250-350 cm^{-1}) in the O-O stretching frequency, which is also a signature of the activation of the O-O bond. From the bond length and the stretching frequency data we can conclude that the maximum activation in O-O bond occurs when O_2 is adsorbed on the edge-Pt atom. Moreover, we observe from Table 5.1 that the activation of O-O bond occurs not only for O_2 adsorbed on the Pt site but also for the cases where the O_2 is adsorbed on the Au sites in the neighborhood of the Pt atom. Such bond activation is important for facilitating the oxidation reaction of CO, which is discussed later in this chapter. In addition to the bond activation, O_2 adsorption energy is also an important parameter for oxidation reaction of CO and in the following we discuss the results for this parameter.

In order to understand the interaction between an O_2 molecule and the bimetallic Au_{19}Pt cluster we calculate the adsorption energy by using the following equation,

$$E_{ad} = -\{E(\text{cluster} - \text{O}_2) - E(\text{cluster}) - E(\text{O}_2)\} \quad (5.1)$$

where $E(\text{cluster}-\text{O}_2)$, $E(\text{cluster})$, and $E(\text{O}_2)$ are the energies of the cluster- O_2 complex, the parent Au_{20} or bimetallic Au_{19}Pt on which O_2 molecule has been adsorbed, and a bare O_2 molecule, respectively. The higher value of E_{ad} indicates a stronger interaction between O_2 and Au_{19}Pt cluster. The adsorption energies of O_2 on the bimetallic Au_{19}Pt cluster are compiled in Table 5.2. For the sake of comparison we also list E_{ad} for adsorption of CO on $\text{Au}_{19}\text{Pt}/\text{Au}_{20}$ clusters [14, 22]. From Table 5.2 we infer that all the Pt sites are more active as compared to the Au sites in the bimetallic Au_{19}Pt clusters. In particular, the vertex-Pt atom is the most active site for both O_2 and CO adsorption. Moreover, we find that the adsorption of O_2 and CO on the bimetallic Au_{19}Pt cluster is much stronger as compared to that on a pure Au_{20} cluster [14]. To get more insight into the adsorption behavior of the doped clusters we plot in Figure 5.2 the variation of O_2 and CO adsorption energies with the d-band centre of the atoms (Pt/Au) on which the respectively molecules are placed for adsorption. From this figure it can be clearly

TABLE 5.2: Adsorption energy (E_{ad}) of O_2 and CO on the various isomers of $Au_{19}Pt$ cluster

System (Td-X-Y _j) ^a	E_{ad} (eV)	
	O_2 adsorption	CO adsorption ^c
Td-0-V	0.21 [0.15] ^b	0.82
Td-0-E	0.07	0.46
Td-0-S	0.06	0.37
Td-S-V1	0.21	0.83
Td-S-V2	0.31	0.89
Td-S-E1	0.07	0.44
Td-S-E2	0.08	0.54
Td-S-E3	0.23	0.77
Td-S-S1	0.62	1.68
Td-S-S2	0.07	0.44
Td-E-V1	0.34	1.03
Td-E-V2	0.24	0.87
Td-E-V3	0.20	0.81
Td-E-E1	1.02	2.06
Td-E-E2	0.30	0.81
Td-E-E3	0.07	0.49
Td-E-E4	0.09	0.56
Td-E-E5	0.07	0.51
Td-E-E6	0.10	0.60
Td-E-E7	0.07	0.56
Td-E-S1	0.06	0.58
Td-E-S2	0.06	0.47
Td-E-S3	0.06	0.39
Td-V-V1	1.32	2.28
Td-V-V2	0.24	0.88
Td-V-E1	0.19	0.89
Td-V-E2	0.17	0.74
Td-V-E3	0.12	0.64
Td-V-S1	0.06	0.46
Td-V-S2	0.07	0.45

^aX = 0 indicates the pure Au_{20} cluster and Y site can be either for O_2 or CO.

^bValue is taken from Ref. [14].

^cValues are taken from Ref. [22].

seen that atoms with d-band centres lying close to the HOMO exhibit higher reactivity in accordance with the well known relationship between the adsorption energy and d-band centre [154]. Furthermore, from Table 5.2 it is observed that the adsorption energies of CO on different sites of the bimetallic $Au_{19}Pt$ cluster are higher (0.3 – 1.0 eV) as compared to the corresponding

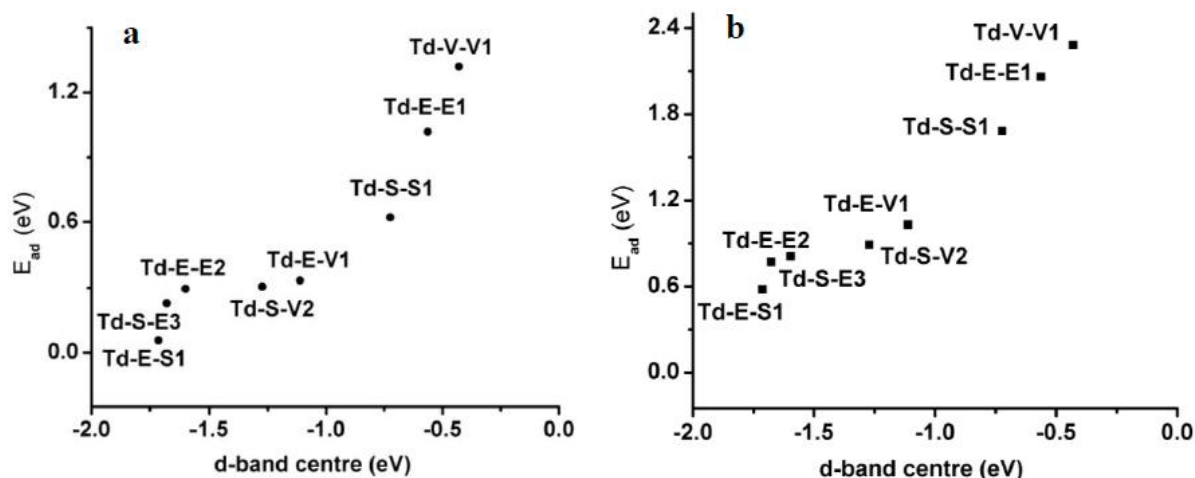


FIGURE 5.2: Adsorption energy vs d-band centre plot for some selected (a) cluster- O_2 and (b) cluster-CO complexes. Here d-band centre is calculated with respect to the HOMO.

O_2 adsorption. This clearly indicates that when O_2 and CO molecules are allowed to get adsorbed together (coadsorption) on the bimetallic $Au_{19}Pt$ cluster, it is CO molecule which will preferably occupy the Pt site and then O_2 will sit on the unoccupied Au sites. To explore the simultaneous adsorption of CO and O_2 next we investigate the coadsorption behavior of these two molecules on the bimetallic $Au_{19}Pt$ cluster and discuss the results in the following.

5.4 Coadsorption of CO and O_2 on Td-E Isomer of $Au_{19}Pt$ Cluster

Having discussed the adsorption properties of CO and O_2 molecules individually, we now discuss the coadsorption of CO and O_2 on the bimetallic $Au_{19}Pt$ cluster. Here, we wish to mention that in Chapter 4 we showed that the bimetallic $Au_{19}Pt$ cluster with Pt atom occupying one of the twelve edges (Td-E) of tetrahedral Au_{20} cluster is the most stable after adsorbing a CO molecule at the Pt site. Similarly, in the present study we find that among all the cluster- O_2 complexes, $Au_{19}Pt-O_2$ (Td-E-E1) configuration with O_2 molecule adsorbed on the edge-Pt atom is the most stable one. Keeping in mind the above results we choose Td-E-E1 configuration where CO is pre-adsorbed (2.06 eV) at the edge-Pt site and O_2 is allowed to get adsorbed on the neighboring

Au sites to obtain the optimized structure of $\text{Au}_{19}\text{Pt-CO(E)-O}_2\text{(V)}$ complex. We observe that O_2 is preferably adsorbed (0.34 eV) at the vertex site which is nearest to the edge-Pt atom. The $\text{CO}+\text{O}_2$ coadsorption energy is found to be 2.48 eV, which is slightly higher than the sum of individual adsorption energies of CO and O_2 (Table 5.2) molecules adsorbed on the corresponding sites. This result indicates that the coadsorption of CO and O_2 is more preferable than their individual adsorptions. In order to understand the effect of pre-adsorbed CO on the activation of O-O bond we calculate the O-O bond length and its stretching frequency, Mulliken charge on O_2 in the $\text{CO}+\text{O}_2$ coadsorbed structure and compare them with the corresponding results for the case where only O_2 is adsorbed on the Au_{19}Pt cluster. The results of these calculations are listed in Table 5.3. From this table we find that the O-O bond length of O_2 (2.282 Å) in

TABLE 5.3: O-O bond length ($R_{\text{O-O}}$), its stretching frequency ($\nu_{\text{O-O}}$) and atomic charge on O_2 (Q_{O_2}) in the $\text{CO}+\text{O}_2$ coadsorbed and only O_2 adsorbed structures.

Catalyst	Species adsorbed	$R_{\text{O-O}}$ (Å)	$\nu_{\text{O-O}}$ (cm^{-1})	Q_{O_2}
Td-E	O_2	1.263	1272	0.2002
	$\text{CO}+\text{O}_2$	1.282	1209	0.2825
Td-S	O_2	1.259	1285	0.1782
	$\text{CO}+\text{O}_2$	1.235	1418	0.0533
Pure Au_{20}	O_2	1.231	1454	0.0317
	$\text{CO}+\text{O}_2$	1.253	1325	0.1561

the complex with coadsorbed $\text{CO}+\text{O}_2$ is higher than the corresponding bond length (2.263 Å) in the complex without CO. This bond length enhancement is also accompanied with a higher value of red shift in the O-O stretching frequency and a higher value of Mulliken charge on O_2 (Table 5.3) for the case of coadsorbed $\text{CO}+\text{O}_2$ complex. Therefore, we conclude from these results that the pre-adsorption of a CO molecule not only promotes the adsorption of O_2 on the Au_{19}Pt cluster but also enhances the activation of the adsorbed O_2 molecule, which may lead to a better oxidation of CO molecule. For the sake of completeness we also calculate the energetic of the $\text{Au}_{19}\text{Pt-CO(V)-O}_2\text{(E)}$ configuration in which the positions of CO and O_2 have been interchanged with respect to the $\text{Au}_{19}\text{Pt-CO(E)-O}_2\text{(V)}$ configuration. We find that the switching of the positions of CO and O_2 increases the energy of $\text{Au}_{19}\text{Pt-CO(V)-O}_2\text{(E)}$ complex by 0.48 eV and hence we concentrate only on the $\text{Au}_{19}\text{Pt-CO(E)-O}_2\text{(V)}$ configuration for studying the

oxidation reaction. Furthermore, we also explore the possibility of adsorption of more than one CO and O₂ molecules onto the doped gold cluster. To this end we consider three cases corresponding to the coadsorption of the three molecules, namely (i) adsorption of two CO and one O₂ molecules, (ii) adsorption of three CO molecules, and (iii) adsorption of one CO and two O₂ molecules. We find that the Pt site can accommodate a maximum of two CO molecules without significantly distorting the parent structure of the Au₁₉Pt cluster. On the other hand, we find that the co-adsorption of CO and O₂ molecules on the Pt site is not energetically favorable. However, coadsorption of CO and O₂ is possible when they are adsorbed at different sites in Au₁₉Pt cluster. Therefore, it is natural to expect that Au₁₉Pt cluster will retain its structure even after multiple (as mentioned above) adsorptions of CO and O₂ molecules.

5.5 Oxidation Reaction of CO on Td-E Isomer of Au₁₉Pt Cluster

Our results presented above clearly demonstrate that the adsorption of CO on the Au₁₉Pt cluster is much stronger as compared to the O₂ adsorption. On the basis of the results on coadsorption discussed above along with the already published data [155, 156] we adopt the Langmuir-Hinshelwood (L-H) mechanism to find the reaction path for the oxidation of CO molecule. In Figure 5.3 we show the reaction path for the oxidation reaction of CO consisting of two intermediate states (Str_A2 and Str_A3) and three transition states (TS_A1 to TS_A3). After the coadsorption of CO and O₂ on Au₁₉Pt cluster (Td-E) we find that the intermediate state (Str_A2) corresponds to the formation of Au₁₉Pt-OOCO complex via the transition state (TS_A1) with a barrier of 0.70 eV (free energy barrier is 0.72 eV in Figure 5.3b). Note that we also explore the possibility of dissociation of the adsorbed O₂ instead of forming OOCO complex. It is observed that the barrier corresponding to this dissociation is very high (2.22 eV) as compared to the barrier for the formation of OOCO complex, hence we do not consider the reaction involving the dissociation of the O₂ molecule. However, we find that the Au₁₉Pt-OOCO complex

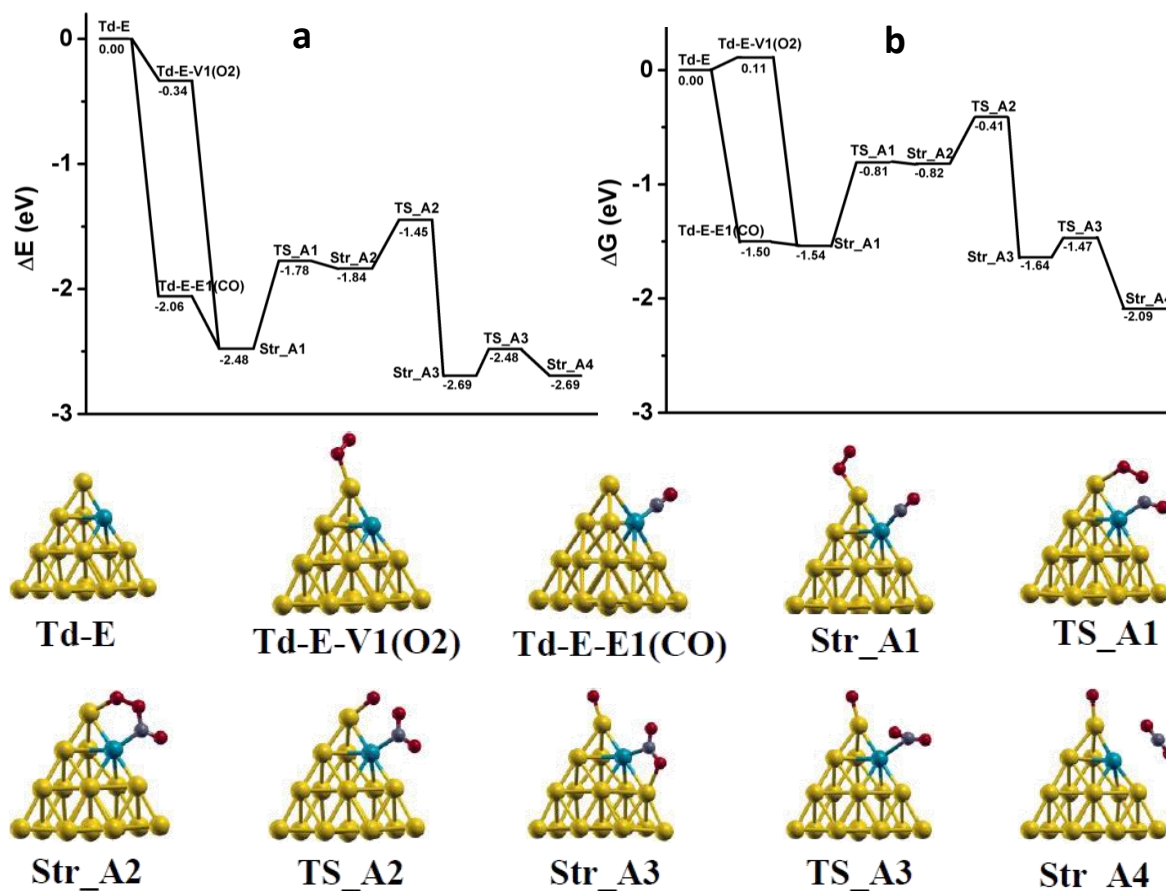


FIGURE 5.3: Partial reaction path for oxidation of CO on Td-E isomer of Au₁₉Pt cluster. ΔE and ΔG (in eV) indicate respectively, the reaction energy and Gibbs free energy calculated between the partial reactants and products.

is 0.64 eV higher in energy as compared to the CO+O₂ adsorbed structure (Str_A1 in Figure 5.3). It indicates that oxidation reaction of CO on Td-E isomer of Au₁₉Pt cluster needs to be thermally excited to initiate the reaction process. For the sake of comparison we also carry out calculations on the CO oxidation on pure Au₂₀ cluster (Figure 5.4). We find that the formation of OOCO complex on pure Au₂₀ requires a lower barrier of 0.30 eV (free energy barrier is 0.31 eV in Figure 5.3b). Here, we wish to mention that our calculated barrier for the formation of OOCO complex on pure Au₂₀ matches well with the result (0.36 eV) reported by Molina et al. [14]. The next step in the CO oxidation process involves the dissociation of the OOCO complex via the transition state TS_A2 (Figure 5.3) with CO₂ and O still attached to the cluster. This dissociation process is thermodynamically favorable as it lowers the energy by 0.21 eV as compared to Str_A1. The barrier corresponding to this dissociation is 0.39 eV (free energy

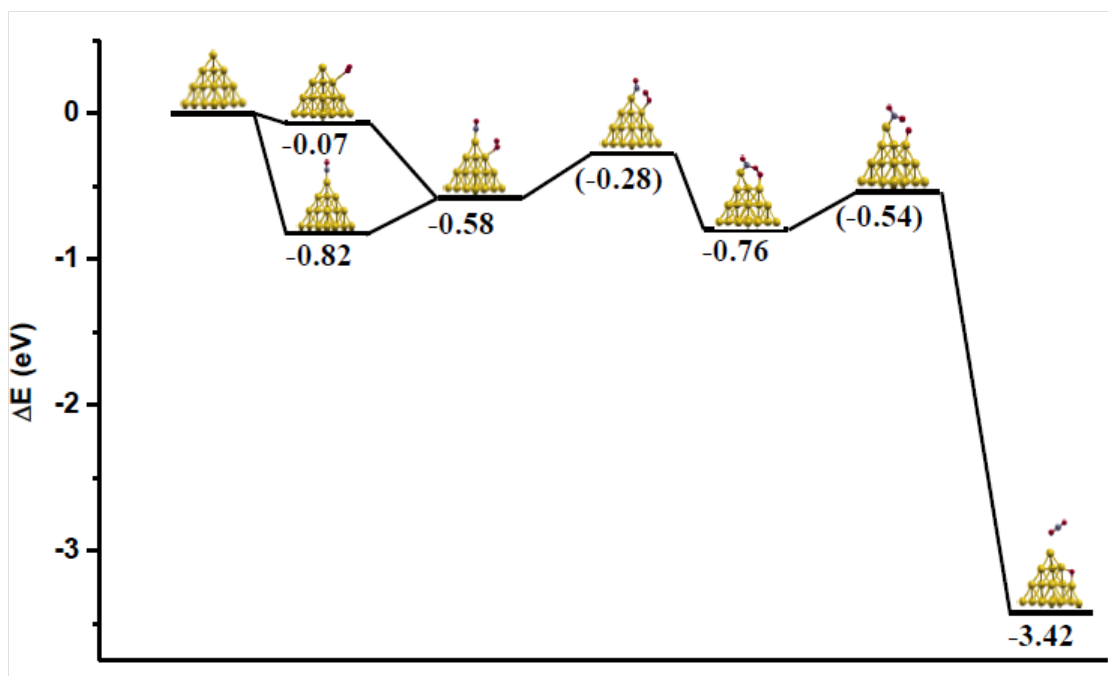


FIGURE 5.4: Partial reaction path for oxidation of CO on pure Au_{20} cluster. ΔE (in eV) indicate the reaction energy calculated between the partial reactants and products.

barrier is 0.42 eV as shown in Figure 5.3b) which is lower as compared to the barrier for the formation of $\text{Au}_{19}\text{Pt-OOCO}$ complex (0.70 eV). We also observe that the elimination of the CO_2 attached to the Au_{19}Pt cluster requires a supply of energy corresponding to a barrier of 0.21 eV (free energy barrier is 0.17 eV in Figure 5.3b). After liberation of the CO_2 molecule the O atom still remains attached to the vertex-Au atom of Au_{19}Pt cluster. At this stage a question arises whether this O atom can diffuse to some other energetically more favorable locations on the cluster. To answer this question we study the adsorption behavior of the O atom at several nearby locations which it can occupy after undergoing diffusion. We observe that this O atom occupying the Au-Pt (edge-edge) bridge site in the cluster is energetically more stable by 1.65 eV than the structure with O occupying the vertex-Au site. The barrier corresponding to this diffusion process is found to be 0.49 eV (free energy barrier is 0.48 eV in Figure 5.3b), which is lower than the barrier for the formation of OOCO complex (0.70 eV). Hence, we infer that at the reaction temperature the diffusion of the O from vertex-Au to the farthest Au-Pt bridge site is possible. As a result, after the liberation of the first CO_2 molecule the remaining O atom diffuses to the Au-Pt bridge site. This O atom can be further used for oxidizing the subsequent CO molecule getting adsorbed on the Au_{19}Pt cluster. To explore this possibility we carry out

more calculations by allowing another CO molecule to get adsorbed on the vertex-Au atom of Au₁₉Pt-O complex. When these two adsorbed species (CO and O) are brought closer, they react to form CO₂ molecule. We find that the barrier corresponding to this reaction is 1.00 eV (free energy barrier is 1.01 eV) which is higher than the barrier corresponding to the formation of OOCO complex. In order to explore the relationship between the adsorption energy and the reaction barrier we consider the case where the diffusion of the O atom is not allowed and the second CO gets adsorbed at the edge-Pt site of Au₁₉Pt cluster. For this case we find that the reaction barrier corresponding to the oxidation of the adsorbed CO is 0.59 eV which is much lower than the case where the diffusion of O atom is allowed. The adsorption energies of the CO+O for the above mentioned two cases (with and without O atom diffusion) are 5.62 and 5.04 eV, respectively. This clearly indicates that the higher value of the adsorption of CO+O is responsible for increase in barrier of the subsequent oxidation reaction of CO as already observed by Nørskov et al. [153]

Having discussed the oxidation reaction of single CO molecule we now focus our attention on the simultaneous oxidation of multiple CO molecules adsorbed on Au₁₉Pt cluster. To this end we calculate the reaction path and the corresponding reaction barriers when there are two CO molecules which are adsorbed on the Pt site whereas a single O₂ molecule is adsorbed on the nearest vertex-Au site. In this case we find that the formation of OOCO complex and its dissociation require crossing the barriers of 0.91 and 0.57 eV respectively. These values are 0.21 and 0.18 eV higher than the corresponding barriers in the case of single CO oxidation. These results clearly indicate that the higher CO coverage does not favor the oxidation reaction of CO molecules. From the above discussion it is very clear that for Au₁₉Pt cluster (Td-E) the adsorption energy and bond activation of CO and O₂ are very high as compared to the corresponding numbers for pure Au₂₀ cluster (Table 5.2 and 5.3). In particular, the increases in the O-O bond length (relative to free O₂ molecule) for CO+O₂ coadsorption on Au₁₉Pt and Au₂₀ clusters are found to be 0.06 Å and 0.031 Å (Table 5.3), respectively. However, as discussed in the above the maximum reaction barrier for the oxidation of CO on Td-E isomer of Au₁₉Pt is also very high (0.70 eV) as compared to the corresponding reaction on a pure Au₂₀ cluster

(0.30 eV). This high reaction barrier for oxidation of CO on the Au₁₉Pt (Td-E) cluster may be attributed to the strong interaction between CO and Au₁₉Pt (Td-E) cluster.

5.6 Coadsorption of CO and O₂ on Td-S Isomer of Au₁₉Pt Cluster

In order to understand the role of CO adsorption energy and the activation of O-O bond on the reaction barrier we further investigate the oxidation of CO molecule on another isomer of Au₁₉Pt cluster, namely Td-S (Figure 4.1), having CO adsorption energy (1.68 eV), which is 0.38 eV lower as compared to that of Td-E isomer, although the bare Td-E and Td-S clusters are very close in energy. For Td-S isomer the CO molecule is adsorbed on surface-Pt atom and the O₂ molecule is adsorbed on the edge site closest to the surface-Pt atom. Similar to the earlier case of CO oxidation on Td-E isomer in Figure 5.5 we show the reaction path for the oxidation of CO on Td-S isomer of Au₁₉Pt cluster. From this figure it is very clear that the energy of the complex Au₁₉Pt-CO-O₂ (Str_B1 in Figure 5.5) is lowered by 1.77 eV due to the coadsorption of CO and O₂ molecules on Td-S isomer of Au₁₉Pt cluster. From Figure 5.5 we note that the adsorption energy of O₂ on Td-S-S1(CO) complex is 0.09 eV. Here, we wish to mention that in the absence of CO the adsorption of O₂ on the Au₁₉Pt (Td-S) cluster (Td-S-E3 complex in Table 5.2) is 0.23 eV, which indicates that the adsorption of O₂ is opposed by the pre-adsorbed CO in the CO+O₂ coadsorbed complex (Str_B1 in Figure 5.5). This trend is in contrast to our earlier case where the pre-adsorbed CO in Td-E-E1(CO) complex facilitates O₂ adsorption considerably. In order to investigate the effect of pre-adsorbed CO on the geometric and electronic structures of the adsorbed O₂ molecule we calculate the O-O bond lengths and corresponding stretching frequencies and Mulliken charges accumulated on the adsorbed O₂ in the complexes with and without CO molecule. These results are presented in Table 5.3. From this table we find that the O-O bond length of O₂ (1.235 Å) in the complex with coadsorbed CO and O₂ is lower than the corresponding bond length (1.259 Å) in the complex without CO. This

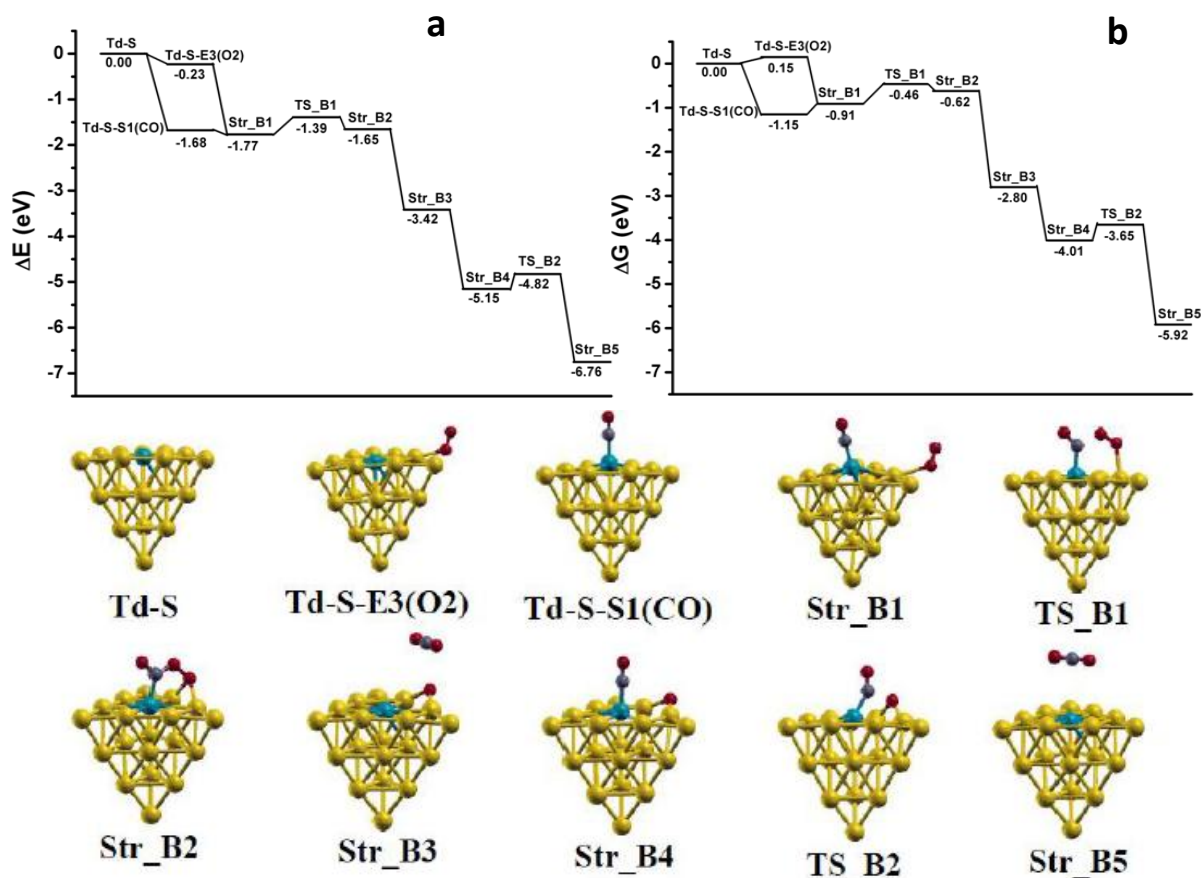


FIGURE 5.5: Complete reaction path for oxidation of CO on Td-S isomer of Au₁₉Pt cluster. ΔE and ΔG (in eV) indicate respectively, the reaction energy and Gibbs free energy calculated between the partial reactants and products

indicates that the pre-adsorbed CO deactivates the O₂ in CO+O₂ coadsorbed structure (Str_B1 in Figure 5.5). This deactivation of O₂ can be attributed to the lower value of Mulliken charge on it in the CO+O₂ coadsorbed complex (Table 5.3). On the other hand, for the case of Td-E, the activation of O-O bond occurs due to the higher value Mulliken charge on O₂. In order to have a better understanding of the connection between the presence of charge on O₂ and its activation we plot in Figure 5.6 partial density of states (PDOS) corresponding to the p-orbital of the adsorbed O₂ (black and blue curves for Td-E and Td-S respectively) along with that of free O₂ (red curve) in Figure 5.6. Note that here the PDOS represents the weightage of a basis function in the molecular orbitals determined by means of Mulliken population analysis. From Figure 5.6 it can be seen that the unoccupied 2 π^* anti-bonding state of free O₂ molecule is partially shifted below the HOMO for Td-E, while for Td-S this anti-bonding level is shifted towards the HOMO and it still remains above the HOMO. In the case of Td-E we observe

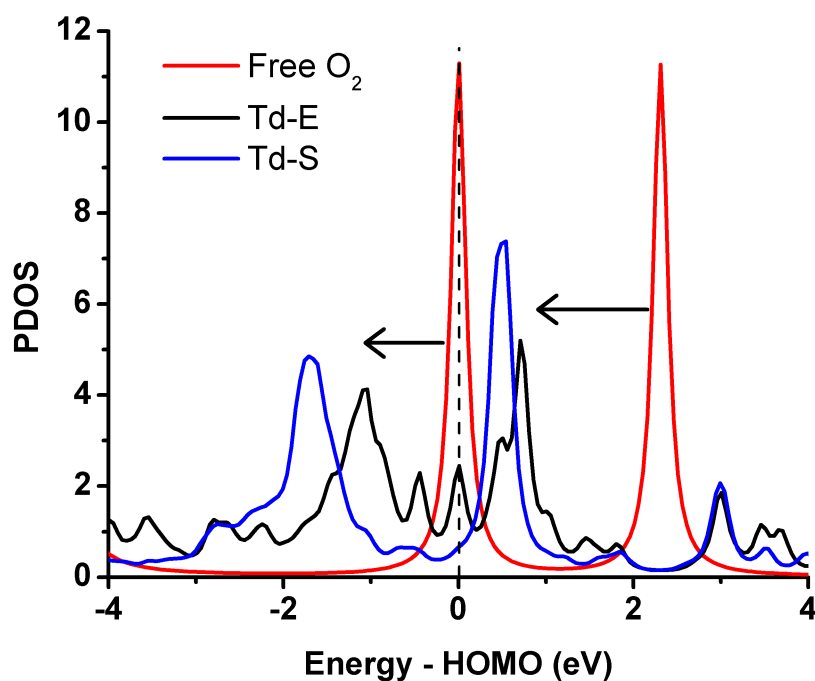


FIGURE 5.6: Partial density of state (PDOS) corresponding to the p-orbital of the O_2 molecule. Black and blue curves indicate the p-orbital of the adsorbed O_2 for the CO+ O_2 coadsorption on Td-E and Td-S respectively. Red curve corresponds to the p-orbital of the free O_2 molecule. The horizontal arrows indicate the shifting direction of the anti-bonding orbitals of the free O_2 molecule. The vertical dotted line denotes the HOMO

higher O-O bond activation as O_2 receives more charges from the cluster whereas, for Td-S the unoccupied anti-bonding state of O_2 remains almost unoccupied. As a result, hardly any activation is observed for the adsorbed O_2 on Td-S.

5.7 Oxidation Reaction of CO on Td-S Isomer of $Au_{19}Pt$ Cluster

Having discussed the activation characteristics of O_2 on Td-S isomer, we now proceed with the discussion on the results for the oxidation of CO molecule. To this end we calculate the energetics of the intermediate (Str_B2) and transition states (TS_B1) falling on the considered

reaction path (Figure 5.5). From Figure 5.5 we find that the formation of $\text{Au}_{19}\text{Pt-OOCO}$ complex (Str_B2) from $\text{CO}+\text{O}_2$ coadsorbed structure (Str_B1) requires crossing a barrier (TS_B1) of 0.38 eV (free energy barrier is 0.45 eV in Figure 5.5b). We wish to note here that the difference in energy between $\text{CO}+\text{O}_2$ coadsorbed and the OOCO complexes for Td-S isomer of Au_{19}Pt is 0.52 eV lower than the corresponding number for the Td-E isomer of Au_{19}Pt cluster. Furthermore, in the case of Td-S isomer the activation barrier for the formation of $\text{Au}_{19}\text{Pt-OOCO}$ complex from the corresponding $\text{CO}+\text{O}_2$ coadsorbed complex is found to be 0.32 eV lower than that in the case of Td-E isomer. As mentioned earlier, the next step in the oxidation of CO requires dissociation of this OOCO complex into CO_2 and O. Interestingly, we find that the dissociation of OOCO complex adsorbed on Td-S isomer of Au_{19}Pt is barrier less and the CO_2 molecule formed after dissociation does not remain attached to the cluster. It is in sharp contrast to the dissociation of OOCO complex adsorbed on Td-E isomer of Au_{19}Pt cluster, which is associated with a finite energy barrier of 0.39 eV, as discussed above. Similar to the Td-E case, after the liberation of one CO_2 molecule second O atom still remains attached to the two Au atoms located at the edge of Au_{19}Pt cluster. Furthermore, similar to the previous case we once again explore the possibility of this O atom undergoing diffusion to the surface-Pt atom. We find that for the O atom to get adsorbed at the Pt site is slightly less (0.05 eV) favorable as compared to its original position. Moreover, the O atom has to cross a diffusion barrier of 0.32 eV to reach the Pt atom. In accordance with these results, unlike Td-E case here we neglect the diffusion of the O atom from the edge-Au to the surface-Pt site. Therefore, the O atom adsorbed at the edge-Au site is subsequently available to oxidize the adsorbed CO molecule. We find that the reaction between these two adsorbed species (CO and O) occurs via the transition state TS_B2 with a barrier of 0.33 eV (free energy barrier is 0.36 eV in Figure 5.5b). This reaction generates another CO_2 and finally Td-S cluster is retrieved without any permanent structural change to the Td-S isomer of Au_{19}Pt cluster.

At this point we wish to remark that in all the cases studied here the adsorption of CO is much higher than that of O_2 , which may lead to the significant covering of the Au_{19}Pt clusters by CO molecules, [157, 158] thereby causing hindrance for O_2 molecules to get adsorbed on various

sites of the clusters. It then becomes necessary to estimate the energy that will be required to replace a CO molecule already adsorbed on cluster surface by an O₂ molecule. To this end we carry out energy calculations for both pure Au₂₀ and doped Au₁₉Pt clusters with a CO molecule adsorbed at the most favorable Au/Pt site and the O₂ molecule replacing the second CO molecule located at nearby gold site. We find that this replacement energy is the maximum (0.75 eV) for pure Au₂₀ and the minimum (0.50 eV) for Td-S cluster. For Td-E cluster this replacement energy decreases from 0.62 eV to 0.52 eV as we go from single CO to double CO adsorption. These replacement energies can be added to the rate limiting reaction barriers to understand the effective reaction barriers for the oxidation of CO on the pure as well as Au₁₉Pt clusters. Accordingly, we find that the effective reaction barrier for Td-S cluster is the lowest among all the clusters studied in the present paper. Overall, from the above discussion we find that the Td-S isomer of Au₁₉Pt cluster is a much better catalyst as compared to the Td-E isomer, although the O₂ activation (in terms of O₂ adsorption energy and O-O bond length) on Td-E isomer is much higher than that on Td-S isomer. Hence, it is very clear that O₂ activation solely does not determine the efficiency of a catalyst. In addition, we find that much stronger adsorption of CO on the Td-E isomer prevents it from performing as a good catalyst for oxidation of CO molecule. Therefore, the value of CO adsorption energy is also an important factor and it plays a crucial role in determining the catalytic activity of a cluster. Moreover, in the overall CO oxidation reaction ($2\text{CO} + \text{O}_2 \rightarrow 2\text{CO}_2$) Td-E isomer is associated with four transition states, on the other hand, Td-S isomer involves only two transition states with much lower energy barrier for the same reaction.

5.8 Conclusions

In summary, our density functional investigation on the O₂ adsorption on the Au₁₉Pt cluster shows that the extent of O-O bond activation may differ widely depending upon the choice of adsorption site within the various isomers of the Au₁₉Pt cluster. We report that the O₂ adsorption on the Td-E isomer of Au₁₉Pt cluster is much stronger as compared to that on a pure Au₂₀

cluster as well as on the Td-S isomer of Au₁₉Pt cluster. Additionally, we find that the presence of pre-adsorbed CO favors the O₂ adsorption in the Td-E structure. Moreover, the O-O bond activation is very high in the case of Td-E (0.06 Å) as compared that in the pure Au₂₀ (0.031 Å) cluster. In spite of this high O-O bond activation on Td-E we find that the reaction barrier for CO oxidation is also very high (0.70 eV) as compared to the case of oxidation reaction of CO occurring on a pure Au₂₀ cluster (0.30 eV). We also investigate the oxidation reaction of CO on another isomer of the Au₁₉Pt cluster (Td-S) possessing an energy very close to that of Td-E. The adsorption energy of CO on Td-S isomer is lower by around 0.38 eV as compared to that on Td-E. We find that the O-O bond activation in CO+O₂ coadsorbed complex on Td-S isomer is 0.013 Å, which is much smaller than the bond activation on Td-E isomer (0.06 Å). However, we observe that the reaction barrier for the oxidation of CO on Td-S (0.38 eV) is much smaller than that on the Td-E cluster (0.70 eV). Comparing the O₂ bond activations on Pt doped Td-E, Td-S and pure Au₂₀ clusters and the corresponding reaction barriers, we conclude that the larger O₂ activation does not necessarily lead to a better oxidation of CO molecule. This behavior may be attributed to a very strong interaction between the CO molecule and the cluster used for catalysis. The reported results in this chapter clearly suggest that over-binding of O₂ may not qualify a cluster as a good catalyst for oxidation of CO, rather CO and O₂ molecules should get adsorbed in an optimal way to make a cluster catalytically more efficient for the same reaction in agreement with the Sabatier principle of catalysis and the expectation of a volcano curve [153, 159]. From the results presented in this chapter it is evident that the optimum values of CO and O₂ adsorption energy may lead to a very good catalytic activity of a cluster, and it is possible to tune this optimum adsorption behavior through doping the cluster with a suitable metal atom for increasing the catalytic efficiency as suggested for other alloy systems [160].

Chapter 6

Gold Clusters on Silicene: Morphology Transformation

In the previous chapters we have discussed the effect of doping on the structural and chemical properties of the gold clusters. We have observed that the incorporation of metal atoms having sizes comparable to that of Au atom does not change the structure of the 20-atom gold cluster. Moreover, such incorporation of metal atoms in the gold cluster leads to a bimetallic cluster having higher chemical reactivity than the pure gold cluster. It is well known that these properties of the gold clusters can also be modified when they are deposited on a suitable solid support [17]. For example, it is reported that the catalytic activity of the Au_8 cluster gets enhanced when it is deposited on a defect rich MgO surface [62]. However, it is observed that pure MgO surface has a very weak effect on the catalytic activity of the gold clusters. This indicates that the nature of the surface plays an important role in modifying the chemical properties of the gold clusters. Moreover, it is important to note here that the morphology of the gold clusters also plays a crucial role in the chemical reactivity of the clusters. It is found that the 2D planer isomer ($\text{Au}_{20}\text{-P}$) of Au_{20} cluster is catalytically more active than its most stable 3D isomer ($\text{Au}_{20}\text{-T}$) [61, 63, 161]. However, in gas phase $\text{Au}_{20}\text{-T}$ is found to be energetically more stable (1.5 – 2.0 eV) [46, 47, 55, 65] than $\text{Au}_{20}\text{-P}$ and hence few studies explored the possibility of tuning or modifying the 3D geometry of Au_{20} cluster by anchoring it to different kind of

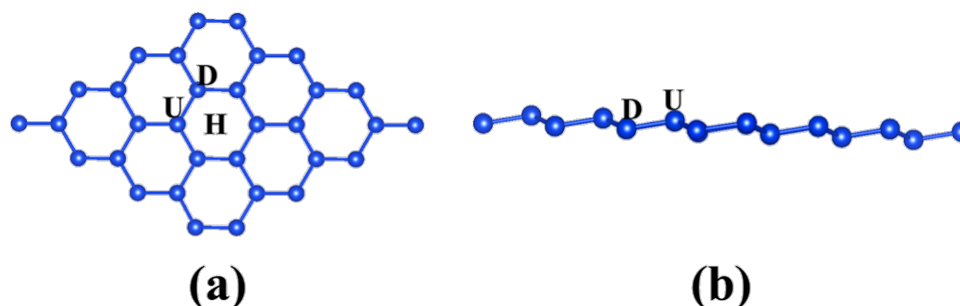


FIGURE 6.1: (a) top view, (b) side view of the free-standing hexagonal buckled 4×4 unit cell of silicene surface.

surfaces [60–63, 65, 68]. It has been shown that the stabilization of Au_{20} -P can be achieved mainly in three possible ways: (i) by using ultrathin layer of MgO on underlying metal surface (Mo(100)) as a support [60, 61, 63], (ii) by using aluminum and nitrogen atom doped MgO and graphene surfaces, respectively, as supports [65, 68], and (iii) by growing the system of cluster and MgO/Ag(100) support in presence of an electric field of strength 1 V/nm [62]. The morphological transformation from 3D to 2D isomer of Au_{20} on these modified surfaces is attributed to the charge transfer from the substrate to the cluster. Moreover, it has been shown that the excess charge on the supported 2D isomer of Au_{20} cluster (Au_{20} -P) makes it better catalytic agent for carrying out the environmentally important CO oxidation reaction. However, it is experimentally observed that the growth of continuous ultrathin film (1-3 layers) of MgO is not possible [61]. Moreover, doping has its own intrinsic complexity and the use of external electric field to stabilize planar form of Au_{20} gold cluster (Au_{20} -P) is also not practicable for actual applications. It is then natural to search for a defect-free undoped surface, which can stabilize the Au_{20} -P cluster even in the absence of any external field. Here, we wish to point out that although graphene doped with nitrogen is capable of transforming the morphology of Au_{20} cluster but its pure form fails to transform the morphology [68]. Recently, silicon based 2D structure analogous to graphene has attracted many researchers due to their novel properties [70, 162–166]. Unlike graphene this 2D structure of silicon, which is termed as silicene has buckled honeycomb arrangement of Si atoms (as shown in Figure 6.1). This buckled silicene has also been grown on various kind of surfaces like Ag(111), $\text{ZrB}_2(0001)$, Ir(111), and

Au(110) [71–74]. The buckling in silicene arises due to the mixing of sp^2 and sp^3 hybridizations rather than purely sp^2 hybridization present in graphene. Moreover, the strength of π bonds between two $3p_z$ orbitals in silicene is weaker than the corresponding bond in graphene formed between two $2p_z$ orbitals. Therefore, it is expected that any adsorbate on silicene surface can easily break the π bonds and can form covalent-like bond with silicon atom. In this context, recently, it has been shown that when a single Au atom is placed on a silicene surface, it binds very strongly to the surface [77]. Subsequently, it has been revealed that the silicene supported single Au atom is also catalytically very active for the CO oxidation reaction [78]. In the light of the above discussion it is quite natural to explore whether a pure silicene surface can be employed for the stabilization of catalytically active planar structures of gold clusters. Moreover, it remains to be investigated whether the buckling present in silicene has any role in stabilizing the 2D isomer of gold clusters. Therefore, in the present chapter our objective is to investigate the morphology and energetic of small (Au_n , $n = 1 - 3$) as well as large (Au_{20}) gold clusters adsorbed on silicene surface by using density functional theory based calculations. We consider silicene surface supported on Ag(111) for all of our calculations in accordance with the recent experimental report [71].

6.1 Computational Details

We employ DFT in combination with PAW method as implemented in MedeA-VASP for our calculations [167–170]. The XC functional is approximated within the GGA as proposed by Perdew, Burke and Ernzerhof (PBE) [92]. Energy cutoff of 500 eV is used to get the converged results in case of all the free gold clusters. To construct the silicene/Ag(111) surface we consider a 3×3 unit cell of silicene deposited on five layers of 4×4 unit cell of Ag (111) [77]. For optimization of this structure we allow all the atoms (Si and Ag) to relax except for the Ag atoms which reside within the bottom three layers of Ag(111). We find that the geometry of the silicene on Ag(111) does not change significantly when we freeze either one or two or three bottom layers of Ag(111). The smaller gold clusters (Au_n , $n = 1 - 3$) are placed on the

optimized silicene/Ag(111) surface. These calculations have been carried out using 250 eV of energy cutoff for plane waves and k-mesh of $3 \times 3 \times 1$ [71]. To study the adsorption of Au₂₀ cluster we consider a 2×2 super cell of the previously constructed silicene/Ag(111) surface so that the interaction between the two neighboring images of the Au₂₀ cluster is negligible. Due to the large size of this system, calculations corresponding to Au₂₀/silicene/Ag(111) systems have been carried out using a single k-point. The size of the unit cells for Au₂₀-P and Au₂₀-T adsorbed on silicene/Ag(111) are taken to be $23.35 \times 23.35 \times 30 \text{ \AA}^3$ and $23.35 \times 23.35 \times 37 \text{ \AA}^3$, respectively. For all the calculations we apply dipole corrections as implemented in MedeA-VASP and the tolerances for energy and force are chosen to be 10^{-5} eV and 0.02 eV/\AA , respectively.

As the dispersion forces are likely to play an important role in determining the properties of the cluster-cluster and cluster/surface systems [171–177], we use Grimme’s dispersion correction [178] along with DFT (PBE + D2 method as implemented in VASP 5.3.5) [167, 179] to take into account the effect of van der Waals (vdW) interaction between the cluster and the surface. Note that for gold the values of C_6 coefficient and R_0 (vdW radius) of Au atom are not included in the program suit. For the present calculations we use the values of C_6 and R_0 for Au as $40.62 \text{ J nm}^6 \text{ mol}^{-1}$ and 1.772 \AA , respectively [177].

6.2 Validation of Theoretical Methodology

To check the reliability of our theoretical approach we first calculate the adsorption energy of a single Au atom adsorbed on a free-standing silicene. To this end we compare our results with the theoretical data already available in the literature [77, 78]. The optimized geometry of a 4×4 unit cell of silicene, which is employed for studying adsorption of a single Au atom is shown in Figure 6.1. In this figure D and U represent the two different Si atoms lying on two planes in silicene and H indicates the centre of the hexagon. To study the adsorption of a single Au atom we place it on either of these three above mentioned locations. The optimization of Au adsorbed on the 4×4 unit cell of silicene has been carried out with energy cutoff of 400 eV and k-mesh

of $7 \times 7 \times 1$. In Table 6.1 we present the results of our calculations along with the reported data [77]. We observe that our results for the adsorption of a single Au atom on free-standing

TABLE 6.1: Calculated Results for the Adsorption of a Single Au Atom on the Free-standing Silicene along with the Corresponding Reported Values

Adsorption sites	Adsorption energy (E_{ad}) ^b (eV)	
	Present results (eV)	Reported (eV) ^a
H	2.39	2.316
U	1.99	1.977
D	2.21	2.159

^aValues are taken from Ref. [77].

^b $E_{ad} = - (E(\text{Au/surface}) - E(\text{surface}) - E(\text{Au}))$, where $E(\text{Au/surface})$, $E(\text{surface})$ and $E(\text{Au})$ are the energies of the Au atom deposited on surface (silicene), the bare surface and the free single Au atom, respectively.

silicene match well with the previously reported data [77]. Furthermore, in accordance with our aim to consider experimentally grown silicene/Ag(111) surface for studying the adsorption of gold clusters we optimize the structure of silicene/Ag(111) surface. We find that the silicene surface is buckled by 0.77 Å which agrees well with both experimental (0.75 Å) [71] and theoretical (0.77 Å) [71, 77] results reported in the literature.

6.3 Adsorption of Smaller Gold Clusters on Silicene

We now proceed with the discussion of our results for the adsorption of various isomers of Au_n ($n = 1 - 3$, and 20) clusters on silicene/Ag(111) surface. To quantify the strength of interaction between the cluster and the surface (silicene/Ag(111)) we calculate the interaction energy given by,

$$E_i = -E(\text{cluster/surface}) - E(\text{cluster}) - E(\text{surface}) \quad (6.1)$$

where $E(\text{cluster/surface})$, $E(\text{cluster})$ and $E(\text{surface})$ are the energies of the gold cluster adsorbed on silicene/Ag(111), bare gold cluster and bare surface (silicene/Ag(111)), respectively,

with the geometries same as those in the composite system. To study the adsorption of the gold clusters we consider different possible adsorption sites on the silicene/Ag(111) surface. For a single Au atom we find that the centre of the hexagon of the silicene surface is the most favorable adsorption site. The interaction energy of a single Au atom on silicene/Ag(111) is found to be 3.13 eV. To explain this strong bonding between silicene and Au we calculate the difference charge density (ρ_{diff}) by using the following expression,

$$\rho_{diff} = \rho_{Au/cluster+surface} - \rho_{surface} - \rho_{Au/cluster} \quad (6.2)$$

where $\rho_{Au/cluster+surface}$, $\rho_{surface}$ and $\rho_{Au/cluster}$, are the charge densities of the gold cluster/Au-atom adsorbed on silicene/Ag(111), bare surface (silicene/Ag(111)) and the bare gold cluster/Au-atom with the geometries same as those in the composite system, respectively. We display the ρ_{diff} for single Au atom adsorbed on silicene/Ag(111) in Figure 6.2. From this figure we ob-

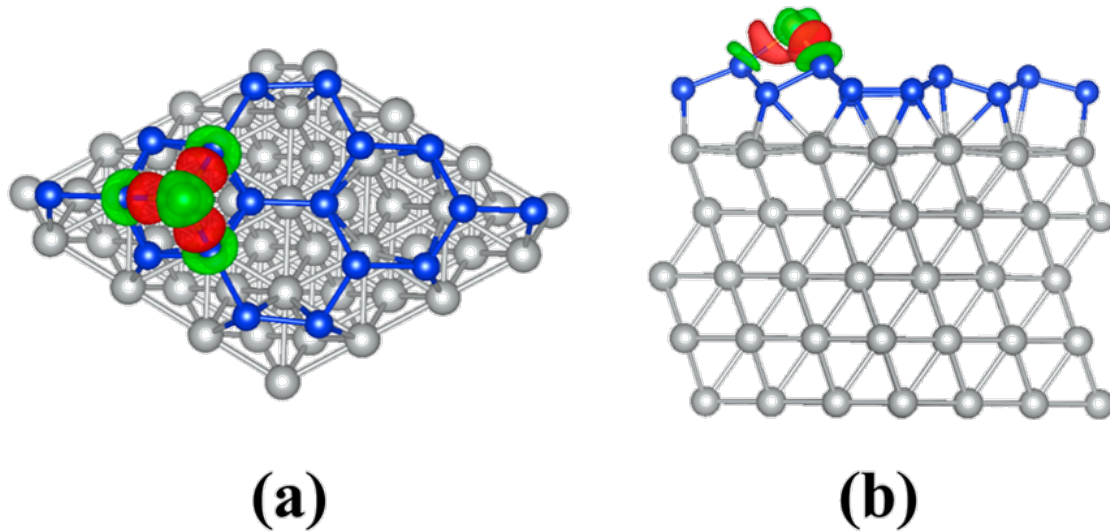


FIGURE 6.2: Difference charge density (ρ_{diff}) with isosurface value of $0.003 \text{ e}/\text{\AA}^3$: (a) top view, (b) side view for Au/silicene/Ag(111) system. Red and green indicate respectively the accumulation and depletion of charge. Gray, blue and yellow balls represent Ag, Si and Au atoms, respectively.

serve that the accumulation of the excess charge occurs at the interface between Au and the silicene surface, but closer to the Au atom. This indicates that there is a strong covalent-like bonding between Au and Si atoms on the silicene/Ag(111) surface.

Having discussed the adsorption of a single gold atom on silicene/Ag(111) surface we now focus our attention on the adsorption of Au_2 and Au_3 clusters. For this purpose we choose two initial configurations of the clusters, namely, horizontal (plane of the cluster is parallel to the surface) and vertical (plane of cluster is perpendicular to the surface) to study their adsorptions. We find that various horizontal and vertical configurations are possible for both Au_2 and Au_3 clusters. Two most stable horizontal and vertical configurations for both Au_2 and Au_3 clusters are shown in Figure 6.3. It is observed that for both Au_2 and Au_3 their horizontal configura-

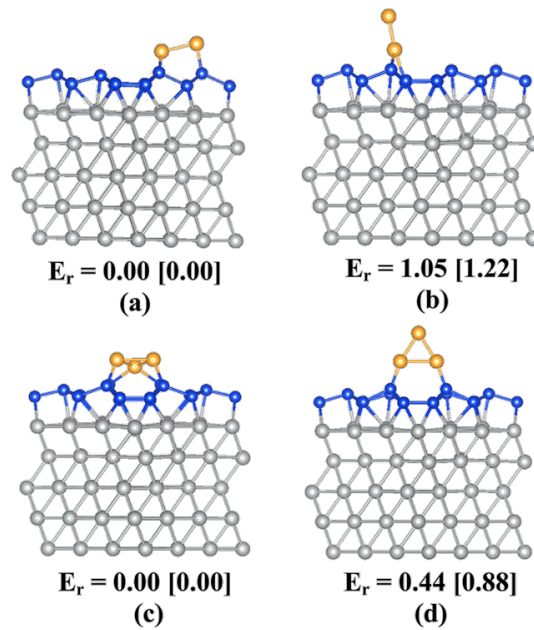


FIGURE 6.3: (a) horizontal, (b) vertical configurations for Au_2 and (c) horizontal, (d) vertical configurations for Au_3 , all are placed on silicene/Ag(111) surface. The values at the bottom indicate the relative energies of the respective configurations. The relative energy (E_r , in eV) values are calculated with respect to the horizontal configuration of the respective cluster. The values outside the square bracket are obtained with PBE XC-functional and the numbers within the square bracket are calculated using PBE + D2 method. Gray, blue and yellow balls represent Ag, Si and Au atoms, respectively.

tions adsorbed on silicene/Ag(111) are the most stable ones. Energetically these configurations are 1.05 and 0.44 eV lower for Au_2 and Au_3 respectively, as compared to their corresponding vertical counterparts. To take into account the effect of van der Waals interaction between the cluster and the surface we use PBE + D2 method and calculate the energies of the Au_n ($n = 2, 3$) clusters deposited on silicene/Ag(111) surface. We find that the horizontal configurations of the Au_n clusters become more stable due to the incorporation of the van der Waals interaction, than for its vertical counterpart (see Figure 6.3). This may be attributed to the fact that more

TABLE 6.2: Interaction energies with and without Grimme's dispersion correction, and average Au-Au and Au-Si bond distances (d_{Au-Au} and d_{Au-Si} , respectively) for the deposited Au_n ($n = 2, 3$) clusters for two different adsorption configurations (horizontal and vertical) along with the average Au-Au bond distances (d_{Au-Au}^g) and binding energies (E_b) of the gas phase Au_n ($n = 2, 3$) clusters

Deposited cluster	Horizontal ^a				Vertical ^a				d_{Au-Au}^g (Å)	E_b (eV) ^b
	d_{Au-Au} (Å)	d_{Au-Si} (Å)	E_i^{PBE} (eV)	E_i^{PBE-D2} (eV)	d_{Au-Au} (Å)	d_{Au-Si} (Å)	E_i^{PBE} (eV)	E_i^{PBE-D2} (eV)		
Au ₂	2.776	2.419	3.39	4.45	2.564	2.462	2.39	2.94	2.517	2.26
Au ₃	2.852	2.436	5.46	6.59	2.666, 2.876	2.312	4.6	5.32	2.673	3.53

^a E_i^{PBE+D2} and E_i^{PBE} indicate the interaction energies obtained using PBE XC-functional with and without Grimme's dispersion correction, respectively.

^b $E_b = - (E(\text{cluster}) - nE(\text{Au}))$, where $E(\text{cluster})$, and $E(\text{Au})$ are the energies of the free cluster, and the Au atom, respectively. n represents total number of Au atoms in the cluster.

number of Au atoms are attached to the silicene/Ag(111) surface for horizontal configuration than for its vertical counterpart. To get more insight into the effect of silicene/Ag(111) on the stability and geometry of the adsorbed Au₂ and Au₃ clusters we calculate the interaction energies with and without Grimme's dispersion correction, various bond lengths (Au-Au and Au-Si) and compare them with the binding energies and bond lengths of the free Au₂ and Au₃ clusters. The results of these calculations are compiled in Table 6.2. From this table we observe that the bond lengths of both Au₂ and Au₃ cluster increase as compared to their gas phase values, when they are placed on the silicene/Ag(111) surface. For Au₂ the increments in bond lengths for horizontal and vertical configurations are 0.259 and 0.047 Å, respectively. Interestingly, the equilateral geometry (gas phase) of Au₃ transforms into isosceles when it is adsorbed on silicene/Ag(111) surface in the vertical configuration. This is because the increase in all the three Au-Au bonds in Au₃ cluster is not isometric. The Au-Au bond parallel to the surface increases by 0.203 Å, while, other two Au-Au bonds remain almost unchanged for Au₃ adsorbed on silicene/Ag(111). On the other hand, in case of horizontal configuration of the adsorption of Au₃ on silicene/Ag(111) the equilateral triangular nature of Au₃ remains intact. Here, the increase in Au-Au bond is 0.179 Å. Furthermore, to investigate the effect of van der Waals forces on the geometries of the adsorbed Au_n clusters we carry out geometry optimization calculations using PBE + D2 method. We find that the geometries of deposited clusters obtained using PBE

+ D2 method are very close to the respective structures obtained with only PBE functional. However, we note that the Au-Au bond length with PBE + D2 increases by around 0.01 Å over its PBE value whereas, the corresponding Au-Si bond length decreases by around 0.02 Å. Having discussed the structures of the adsorbed clusters on silicene/Ag(111) surface we now focus our attention on the interaction energy between the Au_n clusters and silicene/Ag(111) surface. For this purpose we employ expression given by Eq. 6.1 to calculate the interaction energies. The results for interaction energies obtained using PBE XC-functional both with and without Grimme's dispersion correction are compiled in Table 6.2. From this table it is very clear that the incorporation of dispersion correction increases the interaction energy by around 1 eV (0.6 eV) for horizontal (vertical) configurations of Au_2 and Au_3 clusters. This result indicates that the van der Waals interaction is important for gold/silicene/Ag(111) systems and it leads to the higher stability of the horizontal configurations as compared to the vertical configuration of gold/silicene/Ag(111) systems. Moreover, we find that the interaction energies of the Au_2 and Au_3 clusters are higher as compared to their binding energies (gas phase). This indicates that the Au_n ($n = 2, 3$) clusters are more stable when they are placed on silicene/Ag(111) surface. Furthermore, it is observed that for both Au_2 and Au_3 the interaction energy for horizontal configuration is around 1 eV higher as compared to their vertical counterparts. Higher stability of the horizontal configurations may be attributed to the strong covalent-like bonding between the Au and Si atoms [180, 181]. Here, it is important to note that the binding energy of AuSi dimer is 3.34 eV (experimental value is 3.26 eV) [182], which is significantly higher as compared to that of the Au_2 dimer (2.26 eV). This larger binding energy of AuSi dimer favors all the Au atoms in a cluster to lie on the silicene surface to form covalent-like bonds with the Si atoms resulting in highly stable horizontal configurations.

6.4 Adsorption of Larger Gold Clusters on Silicene

From the above discussion we expect that the planar isomer of the gold clusters may be stabilized over their three-dimensional counterparts by depositing them on the silicene/Ag(111)

surface. To explore this possibility for larger clusters, we consider two isomers of Au_{20} cluster ($\text{Au}_{20}\text{-P}$ and $\text{Au}_{20}\text{-T}$) with different dimensionalities (2D and 3D) and study their adsorptions on the silicene/ $\text{Ag}(111)$ surface. The optimized geometries of the $\text{Au}_{20}\text{-P}$ and $\text{Au}_{20}\text{-T}$ clusters adsorbed on silicene/ $\text{Ag}(111)$ surface are given in Figure 6.4. We wish to mention here that

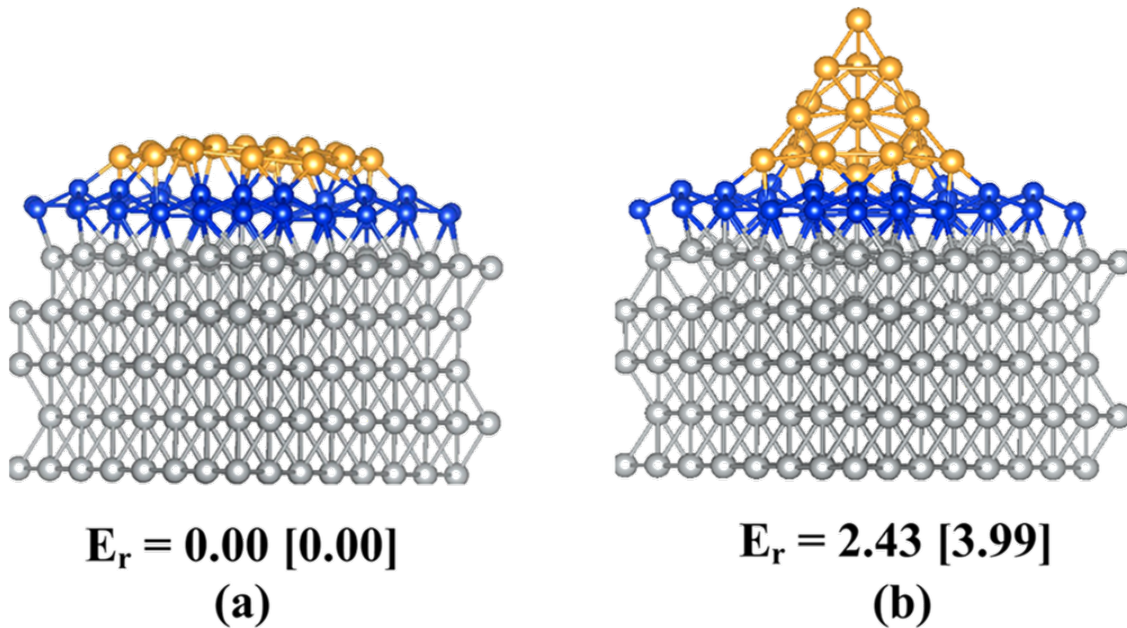


FIGURE 6.4: Optimized geometries: (a) $\text{Au}_{20}\text{-P}$ and (b) $\text{Au}_{20}\text{-T}$, both are placed on silicene/ $\text{Ag}(111)$ surface. The values at the bottom indicate the relative energies of the respective configurations. The relative energy (E_r , in eV) values are calculated with respect to $\text{Au}_{20}\text{-P}$. The values outside the square bracket are obtained with PBE XC-functional and the numbers within the square bracket are calculated using PBE + D2 method. Gray, blue and yellow balls represent Ag, Si and Au atoms, respectively.

the free $\text{Au}_{20}\text{-T}$ cluster is more stable by 1.61 eV as compared to the $\text{Au}_{20}\text{-P}$ isomer (note that the reported values in the literature are in the range of 1.5 – 2.0 eV) [46, 47, 55, 65]. Interestingly, when these isomers of Au_{20} cluster are adsorbed on the silicene/ $\text{Ag}(111)$ surface, the above mentioned energy ordering gets reversed. We observe that $\text{Au}_{20}\text{-P}$ becomes more stable by 2.43 eV than $\text{Au}_{20}\text{-T}$ when they are adsorbed on the silicene/ $\text{Ag}(111)$ surface. Note that in PBE + D2 method the relative stability of $\text{Au}_{20}\text{-P}$ with respect to $\text{Au}_{20}\text{-T}$ increases to 3.99 eV. This indicates that the van der Waals interaction provides additional stability to the planar isomer of Au_{20} compared to its tetrahedral counterpart. To quantify the interaction between the cluster and surface, we calculate the interaction energy as defined in Eq. 6.1.

The interaction energy between Au₂₀-P and silicene/Ag(111) is found to be 18.73 eV, which is around 4 eV higher than that between Au₂₀-T and the same surface (14.64 eV). Note that in PBE + D2 method the interaction energies between the two isomers of Au₂₀ cluster and silicene/Ag(111) surface are found to be 26.22 and 19.57 eV respectively, for Au₂₀-P and Au₂₀-T. The high stability of the Au₂₀-P cluster on silicene/Ag(111) can be attributed to the fact that all the 20 Au atoms make bonds with the surface, whereas for Au₂₀-T, due to tetrahedral geometry only 50 percent of the 20 Au atoms which lie on the base of the tetrahedron can form Au-Si bonds with Si atoms on silicene surface. Thus we find that a pristine silicene surface deposited on Ag(111) can be used to stabilize the 2D isomer of Au₂₀ cluster over its 3D counterpart. Moreover, we wish to point out that the strong Au-Si bond may lead to wetting of the silicene surface by the gold atoms.

We emphasize here that unlike silicene, the stabilization of 2D gold clusters over the 3D counterparts on pristine graphene surface is found to be energetically not favorable [68]. The origin of this distinct difference between the nature of interaction of gold clusters with graphene and silicene can be attributed to the weak π bonds in buckled silicene surface [70, 166], which can easily be broken to form strong Au-Si covalent-like bonds. Consequently, buckled silicene surface leads to the stabilization of the catalytically active 2D planar Au₂₀ cluster over its highly symmetric tetrahedral 3D counterpart when adsorbed on silicene/Ag(111) surface. On the other hand, pristine graphene surface is unable to stabilize the 2D isomer as compared to the corresponding 3D structure due to the presence of strong C-C π bonds and absence of any buckling in it. Further, to gain more insight into the nature of bonding between the surface and the Au₂₀ cluster we calculate the difference charge density (ρ_{diff}) for each isomers adsorbed on the silicene/Ag(111) surface by using the expression given in Eq. 6.2. The results of these calculations are displayed in Figure 6.5. From this figure we observe that the accumulation of the charge takes place at the interface region between cluster and the surface, but closer to the Au atoms. This clearly indicates the presence of strong covalent-like bonding between Au and Si atoms as also observed for the smaller gold cluster. Moreover, we observe from Figure 6.5 that the accumulation of charges occurs around all the 20 atoms in Au₂₀-P whereas only 10

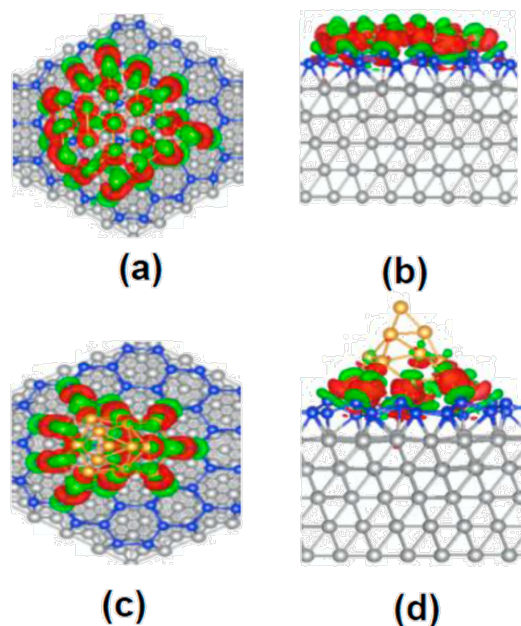


FIGURE 6.5: Difference charge density (ρ_{diff}) with isosurface value of $0.002 \text{ e}/\text{\AA}^3$: (a) top view and (b) side view for $\text{Au}_{20}\text{-P}$, and (c) top view and (d) side view for $\text{Au}_{20}\text{-T}$, both adsorbed on silicene/Ag(111) surface. Red and green indicate, respectively, the accumulation and depletion of charges. Gray, blue and yellow balls represent Ag, Si and Au atoms, respectively.

atoms of $\text{Au}_{20}\text{-T}$ located nearest to the surface acquire the excess charges.

In order to quantify the excess amount of charge acquired by the gold atoms we carry out Bader charge analysis. From this analysis we find that the amount of charge transferred from the surface to the $\text{Au}_{20}\text{-P}$ and $\text{Au}_{20}\text{-T}$ clusters are $0.26e$ and $0.18e$, respectively, per Au atom. It is reported in the literature that the Au atoms with excess charge can serve as active sites for the adsorption of CO and O_2 molecules [14, 17, 183]. As $\text{Au}_{20}\text{-P}$ provides more number of active sites associated with higher amount of negative charge than $\text{Au}_{20}\text{-T}$, it is then expected that the 2D planar isomer will exhibit higher catalytic activity for oxidation reactions as compared to the 3D counterpart. Here, we wish to mention that the amount of charge accumulation observed in the present study is much higher as compared to the earlier values reported in the literature [60–63, 65, 68]. Hence, we expect that $\text{Au}_{20}\text{-P}$ supported on silicene/Ag(111) will act as more efficient catalysts than on already reported supports [60–63, 65, 68].

6.5 Conclusions

In summary, our density functional investigation demonstrates that the strong covalent-like bonding between the Au and Si atoms tend to keep all the Au atoms of the clusters directly attached to the pure silicene/Ag(111) surface. This leads to the stabilization of the catalytically active planar Au₂₀ cluster over its highly symmetric tetrahedral counterpart when adsorbed on silicene/Ag(111) surface. Note that this stabilization of planar structure over the tetrahedral counterpart is further enhanced when van der Waals interaction between the cluster and the surface is taken into account. In contrast to the pure graphene surface, the buckling nature of the pristine silicene surface associated with weak π bonds is largely responsible for the lowering of the energy of Au₂₀-P isomer as compared to the Au₂₀-T structure. It would indeed be interesting to investigate various chemical reactions on silicene supported nano-clusters of gold. The results reported in this thesis clearly indicate that the recently discovered silicene surface has the potential to change the present scenario of gold based catalysts.

Chapter 7

Summary

The catalyst assisted oxidation reaction of carbon monoxide (CO) is very important as this gas is poisonous and generated during the burning of most of the fuels. The gold clusters have been proven to be very effective for the catalytic conversion of CO molecule to less poisonous CO₂. Low temperature catalytic conversion of CO to CO₂ is also possible using gold clusters. Moreover, it is observed that the catalytic activity of the gold cluster can be enhanced by doping them with suitable alkali and transition metal atoms. The catalytic activity of the gold clusters also gets enhanced when these clusters are deposited on suitable surfaces. Motivated by these results, in this thesis we have investigated the effect of dopants and surface support on the structural and chemical properties of the gold clusters with a special emphasis on the Au₂₀ cluster, which has unique electronic and chemical properties. The work presented in this thesis can be divided into two broad categories: (i) the effect of doping on the physicochemical properties of gold clusters, particularly, on the oxidation reaction of CO and (ii) the stabilization of energetically less stable but catalytically more important gold clusters on new solid support. We have considered Li and Pt from alkali and transition metal groups, respectively, to dope the Au₂₀ cluster and silicene surface as a support on which the gold clusters are deposited.

To investigate the effect of doping of Li and Pt atoms on the properties of Au₂₀ cluster we have considered several tetrahedral, cage-like and tube-like geometries of the 20-atom gold cluster.

These clusters are then doped with Li or Pt atoms by replacing the Au atoms from different exohedral and endohedral locations within the pure gold clusters. We find that these dopant elements always favor to occupy the surface positions of the tetrahedron of Au_{20} cluster. For $\text{Au}_{20-n}\text{Li}_n$ ($n = 1 - 4$) clusters we observe that the binding energies of these doped clusters are greater than the binding energy of the pure Au_{20} cluster and it increases almost linearly with the increase in the number of dopant Li atoms. The HOMO-LUMO gaps of these doped clusters follow an interesting trend. For $n = 1$ the HOMO-LUMO gap of the doped cluster decreases as compared to that of pure Au_{20} cluster, while for $n > 2$ HOMO-LUMO gap increases beyond its value for pure Au_{20} cluster. For $n = 4$, all the four surfaces of the tetrahedron of Au_{20} cluster are occupied by the four Li atoms. This doped $\text{Au}_{16}\text{Li}_4$ cluster is energetically more stable by 1.76 eV as compared to that of pure Au_{20} cluster and the HOMO-LUMO gap of $\text{Au}_{16}\text{Li}_4$ cluster is 0.33 eV higher than that of the pure Au_{20} cluster. All the calculated results indicate that the doped $\text{Au}_{16}\text{Li}_4$ cluster may be used as super-atom to construct a cluster assembled material. Moreover, due to the lower value of HOMO-LUMO gap, the Au_{19}Li cluster may exhibit higher reactivity as compared to the pure Au_{20} cluster. To explore this possibility we have investigated the reactivity of the Au_{19}Li cluster using the adsorption of CO molecule as a probe. It is observed that Li doping can enhance the adsorption energy of CO on Au_{19}Li cluster over that of pure Au_{20} cluster. Furthermore, elongation of C-O bond length and the red-shift in C-O stretching frequency have been observed for some of the isomers with high value of adsorption energy including the one with highest value of adsorption energy. Our results indicate that the endohedrally doped cage-like Au_{19}Li clusters may be better catalytic agent than pure Au_{20} cluster for CO oxidation.

Furthermore, continuing our studies on bimetallic clusters, we have investigated the geometries and chemical reactivity of the Au_{19}Pt clusters. It is observed that all the isomers of the tetrahedral Au_{19}Pt cluster are energetically more stable as compared to the pure Au_{20} cluster as well as the cage-like isomers of Au_{19}Pt cluster. The high stability of the bimetallic Au_{19}Pt cluster can be attributed to the strong interaction of Au and Pt atoms, which is caused by the hybridization of s- and d-orbitals of the guest Pt and the host Au atoms in the energy span

of around 5 eV below the HOMO level. To explore the chemical reactivity of the isomers of bimetallic Au_{19}Pt cluster, we have investigated the adsorption behavior of a CO molecule on various non-equivalent sites of these isomers. We have calculated CO adsorption energy, C-O bond length and bond stretching frequency for various possible cluster-CO complexes. We have found that a CO molecule is preferably adsorbed on Pt sites when both Au and Pt sites are exposed for adsorption. Interestingly, we observe that the CO adsorption energy increases by more than 1.3 eV when a CO molecule gets adsorbed on Pt site in tetrahedral Au_{19}Pt cluster as compared to the adsorption on corresponding Au atoms in a pure Au_{20} cluster. Moreover, we have shown that due to the charge transfer from the cluster to the CO molecule its bond length increases by around 0.02 Å, which causes a substantial amount of red shift (104 - 121 cm^{-1}) in C-O stretching frequency. These results indicate that the electronic structure of CO molecule is highly disturbed when it gets adsorbed on the bimetallic clusters, which in turn suggests that the oxidation of adsorbed CO molecule may become easy. This has been explored by calculating the reaction paths and the corresponding barriers and thermodynamic parameters for the oxidation of CO in the presence of Au_{19}Pt clusters. We find that the adsorption of CO is much stronger as compared to that of O_2 . This may lead to the poisoning of Au_{19}Pt clusters by the CO molecules. We find that the possibility of CO poisoning of the pure Au_{20} cluster is higher as compared to that of doped Au_{19}Pt cluster. Moreover, we observe that the higher activation of O_2 and CO molecules does not lead to any lowering the reaction barrier for the oxidation of CO, while stronger CO adsorption certainly increases the reaction barrier. Although, all the results discussed above are not positive with respect to performance of Au_{19}Pt cluster as a catalyst for CO oxidation but our study do show that a particular isomer of Au_{19}Pt cluster in which Pt atom is located at one of the surfaces of tetrahedral structure exhibits better catalytic activity than the pure Au_{20} cluster.

Moreover, we find that for oxidation of CO on Au_{19}Pt cluster the over-binding of O_2 may not qualify a cluster as a good catalyst for CO oxidation, rather CO and O_2 molecules should get adsorbed in an optimal way to make a cluster catalytically more efficient. From the present work it is evident that the optimum values of CO and O_2 adsorption energy may lead to a very

good catalytic activity of a cluster, and it is possible to tune this optimum adsorption behavior through doping the cluster with a suitable metal atom for increasing the catalytic efficiency as suggested for other alloy systems [160]. In order to estimate the optimal values of CO and O₂ adsorption energies it would be necessary to carry out a systematic series of investigations of CO oxidation on Au-Pt bimetallic cluster of different sizes with varying adsorption energies.

With an objective to investigate the effect of support on the geometric and electronic structures of the gold clusters we use recently grown silicene surface and place the Au_n (n = 1 - 3, 20) clusters on it. In contrast to the previous schemes which have been suggested for the stabilization of planar structures of gold clusters by appropriate surfaces, the present proposal does not require any external influence such as doping or application of external electric field. In fact, we have exploited the special characteristics of the silicene surface, namely, buckled nature and weak Si-Si π bonding, which enabled this surface to make strong Si-Au covalent bonds resulting into the two-dimensional planar Au₂₀ isomer as more stable over its three-dimensional tetrahedral structure. In contrast to this, as already reported in the literature, the planar isomer of Au₂₀ cluster is not energetically favored when it is adsorbed on a pure graphene surface. Moreover, Bader charge density analysis indicates that the amount of charge transfer from silicene surface to the planar Au₂₀ cluster is considerably high, thereby increasing the catalytic activity of this composite system. In future we plan to explore the catalytic activity of this composite system by explicitly computing the reaction barriers and the corresponding thermodynamic parameters for oxidation reaction of a CO molecule on this composite system. Furthermore, we wish to note here that it has been experimentally demonstrated that the planar form of platinum clusters can be stabilized on the silicon surface [184] which requires less efforts to grow in laboratory as compared to the silicene surface. In view of this it would be interesting to explore the possibility of stabilizing two dimensional gold structures on silicon surface.

Bibliography

- [1] Alonso, J. A. *Structural and Properties of Atomic Nanoclusters*; Imperial College Press, 2005.
- [2] Johnston, R. L. *Atomic and molecular clusters*; Taylor & Francis, 2002.
- [3] Kreibig, U.; Vollmer, M. *Optical properties of metal clusters*; Springer-Verlag Berlin, 1995.
- [4] Brack, M. *Rev. Mod. Phys.* **1993**, 65, 677.
- [5] de Heer, W. A. *Rev. Mod. Phys.* **1993**, 65, 611.
- [6] Arenz, M.; Landman, U.; Heiz, U. *Chem. Phys. Chem.* **2006**, 7, 1871.
- [7] Qi, C.; Akita, T.; Okumura, M.; Haruta, M. *Appl. Catal. A Gen.* **2001**, 218, 81.
- [8] Ding, X.; Li, Z.; Yang, J.; Hou, J. G.; Zhu, Q. *J. Chem. Phys.* **2004**, 121, 2558.
- [9] Andreeva, D.; Idakiev, V.; Tabakova, T.; Ilieva, L. *Catal. Today* **2002**, 72, 51.
- [10] Pyykkö, P.; Runeberg, N. *Angew. Chem. Int. Ed.* **2002**, 41, 2174.
- [11] Shaw, C. F. *Chem. Rev.* **1999**, 99, 2589.
- [12] Wu, D.; Zhang, Z. D.; Liu, P. X.; Zhang, L. A.; Fan, F. Y. *Curr. Nanosci.* **2011**, 7, 110.
- [13] Huang, X.; El-Sayed, H. I.; Quian, W.; Ei-Sayed, M. A. *J. Am. Chem. Soc.* **2005**, 128, 2115.

- [14] Molina, L. M.; Hammer, B. *J. Catal.* **2005**, *233*, 399.
- [15] Beletskaya, A. V.; Pichugina, D. A.; Shestakov, A. F.; Kuźmenko, N. E. *J. Phys. Chem. A* **2013**, *117*, 6817.
- [16] Jena, N. K.; Chandrakumar, K. R. S.; Ghosh, S. K. *J. Phys. Chem. Lett.* **2011**, *2*, 1476.
- [17] Yoon, B.; Häkkinen, H.; Landman, U.; Wörz, A. S.; Antonietti, J. M.; Abbet, S.; Judai, K.; Heiz, U. *Science* **2005**, *307*, 403.
- [18] Leppert, L.; Kümmel, S. *J. Phys. Chem. C* **2011**, *115*, 6694.
- [19] Ghanty, T. K.; Banerjee, A.; Chakrabarti, A. *J. Phys. Chem. C* **2010**, *114*, 20.
- [20] Mondal, K.; Ghanty, T. K.; Banerjee, A.; Chakrabarti, A.; Kamal, C. *Mol. Phys.* **2013**, *111*, 725.
- [21] Mondal, K.; Manna, D.; Ghanty, T. K.; Banerjee, A. *Chem. Phys.* **2014**, *428*, 75.
- [22] Mondal, K.; Banerjee, A.; Ghanty, T. K. *J. Phys. Chem. C* **2014**, *118*, 11935.
- [23] Mondal, K.; Banerjee, A.; Fortunelli, A.; Ghanty, T. K. *J. Comput. Chem.* **2015**, *36*, 2177.
- [24] Mondal, K.; Kamal, C.; Banerjee, A.; Chakrabarti, A.; Ghanty, T. K. *J. Phys. Chem. C* **2015**, *119*, 3192.
- [25] Habashi, F. *De Re Metallica* **2014**, *23*, 85.
- [26] Humpston, G.; Jacobson, D. M. *Gold Bulletin* **1992**, *25*, 132.
- [27] Yanson, A. I.; Bollinger, G. R.; van den Brom, H. E.; Agrait, N.; van Ruitenbeek, J. M. *Nature* **1998**, *395*, 783.
- [28] Giljohann, D.; Seferos, D.; Daniel, W.; Massich, M.; Patel, P.; Mirkin, C. *Angewandte Chemie International Edition* **2010**, *49*, 3280.
- [29] Pyykkö, P. *Chem. Rev.* **1988**, *88*, 563.

- [30] Pyykkö, P.; Desclaux, J. P. *Acc. Chem. Res.* **1979**, *12*, 276.
- [31] Huang, W.; Bulusu, S.; Pal, R.; Zeng, X. C.; Wang, L. S. *J. Chem. Phys.* **2009**, *131*, 234305.
- [32] Wallace, W. T.; Whetten, R. L. *J. Am. Chem. Soc.* **2002**, *124*, 7499.
- [33] Pabisiak, T.; Kiejna, A. *Phys. Rev. B* **2009**, *79*, 085411.
- [34] Valden, M.; Lai, X.; Goodman, D. W. *Science* **1998**, *281*, 1647.
- [35] Chen, M. S.; Goodman, D. W. *Science* **2004**, *306*, 252.
- [36] Jadzinsky, P. D.; Calero, G.; Ackerson, C. J.; Bushnell, D. A.; Kornberg, R. D. *Science* **2007**, *318*, 430.
- [37] Akola, J.; Walter, M.; Whetten, R. L.; Häkkinen, H.; Grönbeck, H. *J. Am. Chem. Soc.* **2008**, *130*, 3756.
- [38] Lopez-Acevedo, O.; Akola, J.; Whetten, R. L.; Grönbeck, H.; Häkkinen, H. *J. Phys. Chem. C* **2009**, *113*, 5035.
- [39] Xing, X.; Yoon, B.; Landman, U.; Parks, J. H. *Phys. Rev. B: Condens. Matter Mater. Phys.* **2006**, *74*, 165423.
- [40] Bonačić-Koutecký, V.; Burda, J.; Mitrić, R.; Ge, M.; Zampella, P., G. Fantucci *J. Chem. Phys.* **2002**, *117*, 3120.
- [41] Hutchings, G. *J. Catal.* **1985**, *96*, 292.
- [42] Haruta, M.; Kobayashi, T.; Sano, H.; Yamada, N. *Chem. Lett.* **1987**, *16*, 405.
- [43] Pyykkö, P. *Angew. Chem., Int. Ed.* **2004**, *43*, 4412.
- [44] Aikens, C. M.; Schartz, G. C. *J. Phys. Chem. A* **2006**, *110*, 13317.
- [45] Heiz, U.; Schneider, W. D. *J. Phys. D* **2000**, *33*, R85.

- [46] Gruene, P.; Rayner, D. M.; van der Meer, A. F. G.; Lyon, J. T.; Meijer, G.; Fielicke, A. *Science* **2008**, *321*, 674.
- [47] Li, J.; Li, X.; Zhai, H.; Wang, L. S. *Science* **2003**, *299*, 864.
- [48] Peplow, M. *Science* **2013**, *495*, S10.
- [49] Lopez-Acevedo, O.; Kacprzak, K. A.; Akola, J.; Häkkinen, H. *Nat. Chem.* **2010**, *2*, 329.
- [50] Deka, A.; Deka, R. C. *Appl. Nanosci.* **2012**, *2*, 359.
- [51] Sadek, M. M.; Wang, L. *J. Phys. Chem. A* **2006**, *110*, 14036.
- [52] Song, C.; Ge, Q. *J. Phys. Chem. B* **2005**, *109*, 22341.
- [53] Nhat, P. V.; Tai, T. B.; Nguyen, M. T. *J. Chem. Phys.* **2012**, *137*, 164312.
- [54] Heiz, U.; Landman, U. *Nanocatalysis*; Springer-Verlag, Berlin, 2007.
- [55] Kryachko, E. S.; Remacle, F. *Int. J. Quantum Chem.* **2007**, *107*, 2922.
- [56] Wu, K.; Li, J.; Lin, C. *Chem. Phys. Lett.* **2004**, *388*, 353.
- [57] Tlahuice-Flores, A. *J. Mol. Model.* **2013**, *19*, 1937.
- [58] Gao, Y.; Shao, N.; Pei, Y.; Chen, Z.; Zeng, X. C. *ACS Nano* **2011**, *5*, 7818.
- [59] Wang, X. B.; ; Ding, C. F.; Wang, L. S. *J. Chem. Phys.* **1999**, *110*, 8217.
- [60] Ricci, D.; Bongiorno, A.; Pacchioni, G.; Landman, U. *Phys. Rev. Lett.* **2006**, *97*, 036106.
- [61] Harding, C.; Habibpour, V.; Kunz, S.; Farnbacher, A. N. S.; Heiz, U.; Yoon, B.; Landman, U. *J. Am. Chem. Soc.* **2009**, *131*, 538.
- [62] Yoon, B.; Landman, U. *Phys. Rev. Lett.* **2008**, *100*, 056102.
- [63] Zhang, C.; Yoon, B.; Landman, U. *J. Am. Chem. Soc.* **2007**, *129*, 2228.
- [64] Amft, M.; Skorodumova, N. V. *Phys. Rev. B* **2010**, *81*, 195443.

- [65] Mammen, N.; Narasimhan, S.; Gironcoli, S. d. *J. Am. Chem. Soc.* **133**.
- [66] Walter, M.; Frondelius, P.; Honkala, K.; Häkkinen, H. *Phys. Rev. Lett.* **2007**, *99*, 096102.
- [67] Amft, M.; Sanyal, B.; Eriksson, O.; Skorodumova, N. V. *J. Phys.: Condens Matter* **2011**, *23*, 205301.
- [68] Yamijala, S. S.; Bandyopadhyay, A.; Pati, S. K. *J. Phys. Chem. C* **2014**, *118*, 17890.
- [69] Balendhran, S.; Walia, S.; Nili, H.; Sriram, S.; Bhaskaran, M. *Small* **2015**, *11*, 640.
- [70] Jose, D.; Datta, A. *Acc. Chem. Res.* **2014**, *47*, 593.
- [71] Vogt, P.; Padova, P. D.; Quaresima, C.; Avila, J.; Frantzeskakis, E.; Asensio, M. C.; Resta, A.; Ealet, B.; Lay, G. L. *Phys. Rev. Lett.* **2012**, *108*, 155501.
- [72] Fleurence, A.; Friedlein, R.; Ozaki, T.; Kawai, H.; Y., W. *Phys. Rev. Lett.* **2012**, *108*, 245501.
- [73] Enriquez, H.; Mayne, A.; Kara, A.; Vizzini, S.; Roth, S.; Lalmi, B.; Seitsonen, A. P.; Aufray, B.; Greber, T.; Belkhou, R.; Dujardin, G.; Oughaddou, H. *Appl. Phys. Lett.* **2012**, *101*, 021605.
- [74] Meng, L.; Wang, Y.; Zhang, L.; Du, S.; Wu, R.; Li, L.; Zhang, Y.; Li, G.; Zhou, H.; Hofer, W. A.; Gao, H. *J. Nano Lett.* **2013**, *13*, 685.
- [75] Takeda, K.; Shiraishi, K. *Phys. Rev. B* **1994**, *50*, 14916.
- [76] Tao, L.; Cinquanta, E.; Chiappe, D.; Grazianetti, C.; Fanciulli, M.; Dubey, M.; Molle, A.; Akinwande, D. *Nat. Nano.* **2015**, *10*, 227.
- [77] Lin, X.; Ni, J. *Phys. Rev. B: Condens. Matter Mater. Phys.* **2012**, *86*, 075440.
- [78] Li, L.; Gao, Y.; Li, H.; Zhao, Y.; Pei, Y.; Chen, Z.; Zeng, X. C. *J. Am. Chem. Soc.* **2013**, *135*, 19336.
- [79] Martini, A. *The Renaissance of Science: The Story of the Atom and Chemistry*; 2014.

- [80] Chorkendorff, I.; Niemantsverdriet, J. *Concepts of Modern Catalysis and Kinetics*; WILEY-VCH Verlag GmbH & Co. KGaA, Weinheim, 2003.
- [81] Born, M.; Oppenheimer, R. *Ann. Phys. (Leipzig)* **1927**, *84*, 457.
- [82] Fock, V. *Z. Phys.* **1930**, *61*, 126.
- [83] Sousa, S. F.; Fernandes, P.; Ramos, M. J. *J. Phys. Chem. A* **2007**, *111*, 10439.
- [84] Kohn, W.; Sham, L. J. *Phys. Rev.* **1965**, *140*, A1133.
- [85] Hohenberg, P.; Kohn, W. *Phys. Rev.* **1964**, *136*, B864.
- [86] Vosko, S. H.; Wilk, L.; Nusair, M. *Can. J. Phys.* **980**, *58*, 1200.
- [87] Perdew, J. P.; Wang, Y. *Phys. Rev. B* **1992**, *46*, 12947.
- [88] Becke, A. D. *Phys. Rev. A* **1988**, *38*, 3098.
- [89] Perdew, J. P. *Phys. Rev. B* **1986**, *33*, 8822.
- [90] Becke, A. D. *J. Chem. Phys.* **1993**, *98*, 5648.
- [91] Lee, C.; Yang, W.; Parr, R. G. *Phys. Rev. B* **1988**, *37*, 785.
- [92] Perdew, J. P.; Burke, K.; Ernzerhof, M. *Phys. Rev. Lett.* **1996**, *77*, 3865.
- [93] Engel, E.; Dreizler, R. M. *Density Functional Theory*; Springer, 2011.
- [94] Dirac, P. A. M. *Proc. R. Soc. London* **1926**, *A112*, 661.
- [95] Kurth, S.; Perdew, J. P.; Blaha, P. *Int. J. Quantum Chem.* **1999**, *75*, 889.
- [96] Koch, W.; Holthausen, M. C. *A Chemists's guide to Density Functional Theory.*; Wiley-VCH, Weinheim, 2001.
- [97] Becke, A. D. *J. Chem. Phys.* **2014**, *140*, 18A301.
- [98] Perdew, J.; Wang, Y. *Phys. Rev. B* **1992**, *45*, 13244.

- [99] Jónsson, H.; Mills, G.; Jacobsen, K. W. In *Classical and Quantum Dynamics in Condensed Phase Simulations*; Berne, B. J., Ciccotti, G., Coker, D. F., Eds.; World Scientific, Singapore, 1998; p 385.
- [100] Henkelman, G.; Uberuaga, B. P.; Jónsson, H. *J. Chem. Phys.* **2000**, *113*, 9901.
- [101] Zhang, M.; Zhang, H.; Zhao, L.; Li, Y.; Luo, Y. *J. Phys. Chem. A* **2012**, *116*, 1493.
- [102] Yuan, D. W.; Wang, Y.; Zeng, Z. *J. Chem. Phys.* **2005**, *122*, 114310.
- [103] Zhang, X. D.; Gao, M. L. *J. Nanosci. Nanotechnol.* **2010**, *10*, 7192.
- [104] Zhang, X. D.; Gao, M. L.; Wu, D.; Liu, P. X.; Sun, Y. M.; Zhang, L. A.; She, Y.; Liu, Q. F.; Fan, F. Y. *Int. J. Mol. Sci.* **2011**, *12*, 2972.
- [105] Cheng, L.; Xiao-Yu, K.; Zhi-Wen, L.; Ai-Jie, M.; Yan-Ming, M. *J. Phys. Chem. A* **2011**, *115*, 9273.
- [106] Banerjee, A.; Ghanty, T. K.; Chakrabarti, A.; Kamal, C. *J. Phys. Chem. C* **2012**, *116*, 193.
- [107] Gao, Y.; Bulusu, S.; Zeng, X. C. *J. Am. Chem. Soc.* **2005**, *127*, 15680.
- [108] Zhang, F.; Fa, W. *Phys. Lett. A* **2012**, *376*, 1612.
- [109] Baerends, E. J.; Autscbach, J.; Berces et al., A. *Amsterdam Density Functional; Theoretical Chemistry*, Virje Universiteit, Amsterdam, The Netherlands, URL: <http://www.scm.com>.
- [110] van Lenthe, E.; Baerends, E. J.; Snijders, J. G. *J. Chem. Phys.* **1993**, *99*, 4597.
- [111] van Lenthe, E.; Baerends, E. J.; Snijders, J. G. *J. Chem. Phys.* **1994**, *101*, 9783.
- [112] Broyden, C. G. *J. Inst. Math. Appl.* **1970**, *6*.
- [113] Fletcher, R. *Comput. J.* **1970**, *13*.
- [114] Golfrab, D. *Math. Comput.* **1970**, *24*, 23.

- [115] Shanno, D. F. *Math. Comput.* **1970**, *24*, 647.
- [116] Kokalj, A. *Comp. Mater. Sci.* **2003**, *28*, 155.
- [117] Person, W., Zerbi, G., Eds. *Vibrational Intensities in Infrared and Raman Spectroscopy*; Elsevier, Amsterdam,, 1982.
- [118] Overend, A. In *Infrared Spectroscopy and Molecular Structures*; Davis, M., Ed.; Elsevier, Amsterdam, 1963.
- [119] Herzberg, G. *Infrared and Raman Spectra of Polyatomic Molecules*; Van Nostrand, New York, 1986.
- [120] Fan, L.; Ziegler, T. *J. Chem. Phys.* **1992**, *96*, 9005.
- [121] Solovyov, I.; Solovyov, A.; Greiner, W. *Phys. Rev. A* **2002**, *65*, 053203.
- [122] *Jmol: The modes of vibrations of the cluster are visualized using Jmol which is an open-source Java viewer for chemical structures in 3D.*
- [123] Neumaier, M.; Weigend, F.; Hampe, O.; Kappes, M. M. *J. Chem. Phys.* **2005**, *122*.
- [124] De Haeck, J.; Veldeman, N.; Claes, P.; Janssens, E.; Andersson, M.; Lievens, P. *J. Phys. Chem. A* **2011**, *115*, 2103.
- [125] Zhao, Y.; Li, Z.; Yang, J. *Phys. Chem. Chem. Phys.* **2009**, *11*, 2329.
- [126] Jena, N. K.; Chandrakumar, K. R. S.; Ghosh, S. K. *J. Phys. Chem. C* **2009**, *113*, 17885.
- [127] Jiang, D.; Whetten, R. L. *Phys. Rev. B* **2009**, *80*, 115402.
- [128] Ma, W.; Chen, F. *Catal. Lett.* **2013**, *143*, 84.
- [129] Becke, A. D. *Phys. Rev. A* **1988**, *38*, 3098.
- [130] Perdew, J. P. *Phys. Rev. B* **1986**, *33*, 8822.
- [131] Tao, J.; Perdew, J.; Staroverov, V.; Scuseria, G. *Phys. Rev. Lett.* **2003**, *91*, 146401.

- [132] Lopez, N.; Janssens, T.; Clausen, B.; Xu, Y.; Mavrikakis, M.; Bligaard, T.; Nørskov, J. *J. Catal.* **2004**, *223*, 232.
- [133] Lin, L.; Lievens, P.; Nguyen, M. T. *Chem. Phys. Lett.* **2010**, *498*, 296.
- [134] Amft, M.; Johansson, B.; Skorodumova, N. V. *J. Chem. Phys.* **2012**, *136*, 024312.
- [135] Ge, Q.; Song, C.; Wang, L. *Comput. Mater. Sci.* **2006**, *35*, 247.
- [136] Morrow, B. H.; Resasco, D. E.; Striolo, A.; Nardelli, M. B. *J. Phys. Chem. C* **2011**, *115*, 5637.
- [137] Tian, W. Q.; Ge, M.; Gu, F.; Yamada, T.; Aoki, Y. *J. Phys. Chem. A* **2006**, *110*, 6285.
- [138] Pedersen, M. O.; Helveg, S.; Ruban, A.; Stensgaard, I.; Lægsgaard, E.; Nørskov, J. K.; Besenbacher, F. *Surf. Sci.* **1999**, *426*, 395.
- [139] Lang, H.; Maldonado, S.; Stevenson, K. J.; Chandler, B. D. *J. Am. Chem. Soc.* **2004**, *126*, 12949.
- [140] Mott, D.; Luo, J.; Njoki, P. N.; Lin, Y.; Wang, L.; Zhong, C. J. *Catal. Today* **2007**, *122*, 378.
- [141] Leppert, L.; Albuquerque, R. Q.; Foster, A. S.; Kümmel, S. *J. Phys. Chem. C* **2013**, *117*, 17268.
- [142] Morse, M. D. *Chem. Rev.* **1986**, *86*, 1049.
- [143] Dai, D.; Balasubramanian, K. *J. Chem. Phys.* **1994**, *100*, 4401.
- [144] Wang, S. J.; Kung, X. Y.; Lu, C.; Li, Y. F.; Zhao, Y. R. *Phys. Chem. Chem. Phys.* **2011**, *13*, 10119.
- [145] Chase, M. W.; Davies, C. A.; Downey, J. R.; Frurip, D. J.; McDonald, R. A.; Syverud, A. N. *J. Phys. Chem. Ref. Data* **1985**, *14*.

- [146] Lied, D. *CRC Handbook of Chemistry and Physics*, 81st ed.; CRC Press: Boca Raton, FL., 2000.
- [147] Tran, D. T.; Johnston, R. L. *Proc. R. Soc. A* **2011**, DOI: 10.1098/rspa.2010.0562.
- [148] Pal, R.; Wang, L. M.; Pei, Y.; Wang, L. S.; Zeng, X. C. *J. Am. Chem. Soc.* **2012**, *134*, 9438.
- [149] Lopez, N.; Norskov, J. K. *J. Am. Chem. Soc.* **2002**, *124*, 11262.
- [150] Widmann, .; Bhém, R. J. *Acc. Chem. Res.* **2014**, *47*, 740.
- [151] Eichler, A.; Hafner, J. *Phys. Rev. B* **1999**, *59*, 5960.
- [152] Weiher, N.; Beesley, A. M.; Tsapatsaris, N.; Delannoy, L.; Louis, C.; van Bokhoven, J. A.; Schroeder, S. L. M. *J. Am. Chem. Soc.* **2007**, *129*, 2240.
- [153] Falsig, H.; Hvolbæk, B.; Kristensen, I. S.; Jiang, T.; Bligaard, T.; Christensen, C. H.; Nørskov, J. K. *Angew. Chem. Int. Ed.* **2008**, *47*, 4835.
- [154] Nørskov, J. K.; Abild-Pedersen, F.; Studt, F.; Bligaard, T. *Proc. Natl. Acad. Sci.* **2011**, *108*, 937.
- [155] Liu, C.; Tan, Y.; Lin, S.; Li, H.; Wu, X.; Li, L.; Pei, Y.; Zeng, X. C. *J. Am. Chem. Soc.* **2013**, *113*, 2583.
- [156] Zhang, J.; Alexandrova, A. N. *J. Phys. Chem. Lett.* **2013**, *4*, 2250.
- [157] Negreiros, F. R.; Barcaro, G.; Sementa, L.; Fortunelli, A. *C. R. Chimie* **2014**, *17*, 625.
- [158] West, P. S.; Johnston, R. L.; Barcaro, G.; Fortunelli, A. *J. Phys. Chem. C* **2010**, *114*, 19678.
- [159] Vannice, M. A. *J. Catal.* **1977**, *50*, 228.
- [160] Liu, J. H.; Wang, A. Q.; Chi, Y. S.; Lin, H. P.; Mou, C. Y. *J. Phys. Chem. B* **2005**, *109*, 40.

- [161] Martínez, A. *J. Phys. Chem. C* **2010**, *114*, 21240.
- [162] Cahangirov, S.; Topsakal, M.; Akturk, E.; Sahin, H.; Ciraci, S. *Phys. Rev. Lett.* **2009**, *102*, 236804.
- [163] Sahin, H.; Cahangirov, S.; Topsakal, M.; Bekaroglu, E.; Akturk, E.; Senger, R. T.; Ciraci, S. *Phys. Rev. B: Condens. Matter Mater. Phys.* **2009**, *80*, 155453.
- [164] Ezawa, M. *Phys. Rev. Lett.* **2012**, *109*, 055502.
- [165] Houssa, M.; Pourtois, G.; Afanasev, V. V.; Stesmans, A. *Appl. Phys. Lett.* **2011**, *97*, 112106.
- [166] Kamal, C.; Chakrabarti, A.; Banerjee, A.; Deb, S. K. *J. Phys.: Condens. Matter* **2013**, *25*, 085508.
- [167] Kresse, G.; Furthmüller, J. *Phys. Rev. B: Condens. Matter Mater. Phys.* **1996**, *54*, 11169.
- [168] Kresse, G.; Joubert, D. *Phys. Rev. B: Condens. Matter Mater. Phys.* **1999**, *59*, 1758.
- [169] Blöchl, P. E. *Phys. Rev. B: Condens. Matter Mater. Phys.* **1994**, *50*, 17953.
- [170] *VASP 5.2 Programme Package Used Here is Fully Integrated in the MedeA Platform (Materials Design, Inc.) with a Graphical User Interface Enabling the Computation of the Properties.*
- [171] Banerjee, A.; Chakrabarti, A.; Ghanty, T. K. *J. Chem. Phys.* **2007**, *127*, 134103.
- [172] Banerjee, A.; Autschbach, J.; Chakrabarti, A. *Phys. Rev. A: At., Mol., Opt. Phys.* **2008**, *78*, 032704.
- [173] Kamal, C.; Ghanty, T. K.; Banerjee, A.; Chakrabarti, A. *J. Chem. Phys.* **2009**, *131*, 164708.
- [174] Tao, J.; Perdew, J. P. *J. Chem. Phys.* **2014**, *141*, 141101.
- [175] Hatz, R.; Hänninen, V.; Halonen, L. *J. Phys. Chem. A* **2014**, *118*, 5734.

- [176] Girifalco, L. A.; Hodak, M. *Phys. Rev. B: Condens. Matter Mater. Phys.* **2002**, *65*, 125404.
- [177] Amft, M.; Lebègue, S.; Eriksson, O.; Skorodumova, N. V. *J. Phys.: Condens. Matter* **2011**, *23*, 395001.
- [178] Grimme, S. *J. Comput. Chem.* **2006**, *27*, 1787.
- [179] Bučko, T.; Hafner, J.; Lebègue, S.; Ángyán, J. G. *J. Phys. Chem. A* **2010**, *114*, 11814.
- [180] Barysz, M.; Pyykkö, P. *Chem. Phys. Lett.* **1998**, *285*, 398.
- [181] Kiran, B.; Li, X.; Zhai, H. J.; Cui, L. F.; Wang, L. S. *Angew. Chem., Int. Ed.* **2004**, *43*, 2125.
- [182] Huber, K.; Herzberg, G. *Molecular Spectra and Molecular Structure. IV. Constants of Diatomic Molecules*; Van Nostrand, New York, 1974.
- [183] Sanchez, A.; Abbet, S.; Heiz, U.; Schneider, W. D.; Häkkinen, H.; Barnett, R. N.; Landman, U. *J. Phys. Chem. A* **1999**, *103*, 9573.
- [184] Yasumatsu, H.; Hayakawa, T.; Koizumi, S.; Kondow, T. *J. Chem. Phys.* **2005**, *123*, 124709.